UNIVERSITY OF TWENTE.

FACULTY OF ELECTRICAL ENGINEERING, MATHEMATICS &
COMPUTER SCIENCE

Dual-DC-port Inverter for a Fuel Cell Electric Aircraft

R. H. Kersjes
M.Sc. Thesis
September 1, 2023

Supervisors and Committee members:
Prof. dr. ir. T. Batista Soeiro
dr.ir. P. Venugopal
ir. A.I. de Boer

External Committee:
dr.ir. C. Salm

Power Electronics and EMC Group
Faculty of Electrical Engineering,
Mathematics & Computer Science
University of Twente
PO Box 217
7500 AE Enschede
The Netherlands

Summary

The development of a fuel cell electric range extender for the battery electric Pipistrel Velis Electro by NLR resulted in the question if it is possible to distribute the power of the fuel cell and battery energy storage systems and the electric motor of the aircraft with a single power electronic system in the form of a dual-DC-port inverter.

A conventional system architecture with one DC/DC converter and one DC/AC inverter was used as a benchmark to compare a number of promising dual-DC-port inverter architectures. The different architectures were converted into models in Simulink with the PLECS Blockset and adjusted to comply with a fixed set of requirements. These models were tested on the same dynamic load profiles based on the load profile of flight data from the Pipistrel. The resulting designs and simulations were used to compare the architectures on some significant characteristics. The multi-source inverter showed to be the most promising dual-DC-port inverter architecture for this application.

To operate the multi-source inverter in all available load configurations a multi-objective vector modulation algorithm was required. This algorithm was based on existing strategies in recent papers with a novel addition that allows the system to operate more efficiently when the motor is operated with a low power factor.

The multi-source inverter and multi-objective vector modulation algorithm were studied more in-depth with an experimental setup that emulates the energy storage systems with DC power supplies and the aircraft's engine with a variable AC load. These tests introduced some additional challenges that were not anticipated in the models. After these challenges were mitigated, the experimental data supported the results from the simulations.

In the end, the multi-source inverter was shown to be a viable alternative to the benchmark system architecture. As there are advantages and disadvantages to both designs, neither of the designs was a clear winner. The results do show the potential of the multi-source inverter and warrant a more in-depth investigation into the system.

Preface

This research was conducted in collaboration with the Netherlands Aerospace Centre (NLR) as an extension to their Pipistrel Range Extender project. This project gave rise to the main question that was explored in this project. Some data was provided regarding the use and capabilities of the Pipistrel as well as the desired system requirements. Special thanks goes to Ir. Alte de Boer who provided guidance during the project and enabled me to work on such an interesting and significant project.

I would also like to thank my UT supervisors Prof. Dr. Thiago Batista Soeiro and Dr. Ir. Prasanth Venugopal for their advice, feedback and expertise during the project. In addition, I want to thank Dr. Ir. Cora Salm for her time and expertise in acting as my external committee member.

Lastly, I want to thank the members of the power electronics and EMC group that assisted me during the project, especially during the experimental phase of the project.

Contents

1. Introduction

The aviation industry is an important part of today's society and economy, connecting people and businesses around the world. A downside is that the industry is also responsible for a significant share of the global carbon emissions and the sector is expected to grow rapidly in the coming decades. This has led to the desire to find more sustainable alternatives to existing technologies. The largest impact can be made by replacing fossil fuels with renewable sources of energy like bio- or synthetic fuels or electrical energy storage systems. The latter requires a more drastic overhaul of the power distribution system but also offers additional benefits like reduced noise and pollution.

Battery energy storage systems are one solution that is considered for fully electric aircraft and a number of prototypes have been produced in the recent years. In 2020 the Pipistrel Velis Electro became the first certified fully electric aircraft. This aircraft is able to transport up to two people with some cargo. The main limitation of the aircraft is the energy storage density of the battery packs which limits the distance it can travel. A different energy storage technology that promises a higher energy density are fuel cells that produce electricity with the electrochemical reaction of hydrogen and oxygen into water. These fuel cell electric systems introduce different limitations and fuel cell electric aircraft are still in development, with multiple prototypes seen in the past few years. A promising solution is to combine battery and fuel cell electric systems which can benefit of the advantages of both technologies.

1.1 Context

NLR is in possession of a Pipistrel Velis Electro and is attempting to improve the flight range of the aircraft with a fuel cell electric range extender. This project is used to gain insights into the challenges that arise when designing such a hybrid system and to look for solutions that may improve such a system. To use the energy supplied by the fuel cell system an interface is required that integrates the varying output voltage of the fuel cell into the rest of the system. Ideally, the fuel cell power is added to that of the battery to share the load and reduce the strain on the battery packs while making optimal use of the existing DC/AC motor inverter. It is possible to implement this with existing fuel cell DC/DC converters that control the output power of the fuel cell and convert the varying DC fuel cell voltage to that of the battery pack. Such a converter adds additional weight and volume to an aircraft that is already close to its weight limit.

1.2 Research objectives

The limited space and weight available for the addition of a fuel cell electric energy storage system and the associated power electronic system led to the following question:

- Can the power distribution system in a battery and fuel cell electric aircraft be improved by combining a number of power electronic systems?

To improve the process in finding an answer to this question, three sub-questions are listed. To better understand the requirements to properly operate the energy storage systems and what a power distribution system should be able to do, an analysis should be made following the first sub-question. The second question requires an exploration of so called dual-DC-port inverter technologies that combines the functionality of the DC/DC converter with that of the inverter and should decrease the total number of converters required for this application. The last sub-question is set to find out whether the system is actually improved by the use of these multi-port converters.

- What are the challenges with distributing electric power between the different energy storage systems?

- What dual-DC-port converters exist that are suitable for this application?

- How do these dual-DC-port converters compare to a more conventional solution?

1.3 Outline

Chapter 2 considers the different elements in a full electric aircraft from a number of perspectives. First a description is made on the existing and upcoming technologies in electric aircraft. This includes fully and partially electric aircraft as well as the available fuel cell, battery and power electronic systems. Next, the design of the existing battery electric Pipistrel Velis Electro is considered more in depth, to find out how this system is used, which loads are expected and how a fuel cell system can improve the flight range. Finally, a more in-depth description of proton exchange membrane fuel cell (PEMFC) and lithium ion battery systems is given. This analysis is used to describe how these systems should be used and how this influences the power and energy management strategy. In addition, the technologies are converted into equivalent circuit models which are later used to test how these systems perform under dynamic loading.

Chapter 3 considers a number of power distribution systems and how they could integrate the fuel cell range extender into the battery electric aircraft. The first design acts as a benchmark and is based on the original Pipistrel system with an additional DC/DC converter to converter the fuel cell output voltage to match with that of the battery. The other designs consider dual-DC-port inverters that integrate the DC/DC conversion into the motor inverter system. All designs are tested on the dynamic loading conditions and requirements of the energy storage systems described in chapter 2. Once the designs have been tested, a comparison is made on the performance of the different designs. The most promising solution is explored further in the following chapters.

Chapter 4 describes an multi-objective control algorithm that was developed to enable the multi-source inverter to distribute power between all three ports while maintaining the desired output voltage set by a standard field-oriented control motor controller. This algorithm attempts to maximize the available output voltage based on the available DC voltages and the output power factor. When the available output voltage is increased, the motor can output the same power with less current, making it more efficient.

Chapter 5 tests the multi-source inverter and multi-objective control algorithm created in chapter 4 in an experimental setup. A variable electronic load is used to simulate the motor in certain operating conditions found in the simulation in chapter 3. An existing T-type inverter is modified to operate as a multi-source inverter, this inverter is controlled using a real-time simulator running the control algorithm.

Chapter 6 reflects on the research objectives and the value of the different elements of the project. This includes the validity of the comparison and the results of the experiments on the prototype. Finally, some recommendations that could be used to further this research are considered.

2. Background

2.1 State of the art in electrification of aircraft

An overview of developments in the electrification of aircraft is created to show the potential, progress and challenges with electrification of aircraft. This includes developments in full electric aircraft as well as the energy storage systems that are required for the electrification of these aircraft.

2.1.1 Recent achievements in industry

In 2020 the Pipistrel Velis Electro became the first certified fully electric aircraft [1]. The range of this two seater aircraft is still somewhat limited with 50 minutes of flight in which it can travel up to 70 km [2]. This shows that for small ranges battery electric flight is possible. A larger 9 passenger Cessna 208 was retrofitted by MagniX with a battery electric propulsion system and flew for 30 minutes. For traveling longer distances the specific energy of batteries is insufficient and battery energy storage systems are unlikely to be a viable solution unless a significant breakthrough is made in the technology [3].

Fuel cell electric demonstrators

Fuel cell powered aircraft have also been tested in numerous demonstrators of different scales. In 2008 Boeing already flew a fuel cell and battery electric two seater aircraft [4]. Recently, ZeroAvia flew a 19 seater Dornier 228 for 10 minutes with one fuel cell electric powered engine and one conventional engine [5]. Before this, ZeroAvia performed a short hydrogen powered flight with a converted 6 seater Piper Malibu aircraft using a 100 kW fuel cell system [6]. Universal Hydrogen demonstrated a Dash 8-300 that was also partially powered by a hydrogen fuel cell. During take-off the aircraft was assisted by a conventional fuel engine but the fuel cell became the main power source during cruise [7]. These demonstrators show that progress on implementing fuel cell electric propulsion is being made but that some improvements are still required before a certified fuel cell electric aircraft can be produced.

2.1.2 Battery systems

Battery electric systems are the most common energy storage system in partial or fully electrified automotive vehicles. Larger battery electric systems are often based on lithium-ion technologies and the energy and power density of these batteries makes them worth considering for use in electric propulsion systems in aircraft as well. Although it appears that batteries will not be suited for long distance travel they are still an important subsystem in fuel cell electric aircraft.

Specific energy and power

The best reference on aircraft suited battery packs is the PB345V124E-L used in the Velis Electro, which includes all the systems required for safe operation of Lithium batteries in aircraft. An individual battery pack weighs 72 kg, has a rated power of 40 kW and energy capacity of 12 kWh [8]. This results in a specific energy of 0.17 $\frac{kWh}{kg}$ and a specific power of 0.6 $\frac{kW}{kg}$ for the full system. When the specific energy is compared with that of jet fuel at 12 $\frac{kWh}{kg}$ [9] it becomes clear that large improvements in battery technology are required to enable long distance battery electric flight.

2.1.3 Fuel cell systems

A small analysis of current state of the art fuel cell systems is also executed. For aviation the mass of hydrogen storage systems and fuel cell systems should be minimized as the take-off weight is expected to be one of the main challenges with electrification of aircraft. A number of fuel cell technologies are available with different electrolyte materials, charge carrier, fuels and operating temperature. Proton exchange membrane fuel cells

using pure hydrogen as fuel make most sense for the application in small electric aircraft due to the system simplicity, low temperature and high efficiency [10].

Specific energy

A promising property of hydrogen is that it has a large amount of energy stored per kg of fuel, however, because the density of hydrogen is very low at standard temperature and pressure it can be hard to store hydrogen in a small volume. Multiple technologies are available for improving the density of hydrogen like storing it at high pressures or liquefying it at cryogenic temperatures. The storage mediums that can withstand these abnormal conditions weigh much more than the hydrogen that is stored inside them. The effective energy density of the hydrogen storage system can be expressed as the energy stored in kWh vs the mass of the tank in kg or alternatively in a gravimetric index of the mass of hydrogen stored per kilogram of tank. A number of different hydrogen storage technologies are available, with a range of volumetric and gravimetric energy densities [11]. A target set by the US department of energy for hydrogen storage in light electric vehicles is a gravimetric index of 4.5% in 2020 and eventually aiming for 6.5%. A similar number is also given for the volumetric storage density, with a target of 0.03 $\frac{kg}{L}$ for 2020 [12]. A report from the Clean Sky 2 joint undertaking gives a gravimetric index of 15-20% for liquid hydrogen storage systems and aims for a gravimetric index of 35% in 2050 which would result in a specific energy of 12 $\frac{kWh}{kg}$, matching that of jet fuel. Some 700 bar gaseous hydrogen storage tanks like the H2-70-368X878 from Hexagon Purus are already available for automotive applications with a gravimetric index of 5.8%, storing 2.1 kg of hydrogen in a 85 L tank. Liquid hydrogen storage promises a larger gravimetric index but introduces the challenge of liquid boil-off which can limit the time that hydrogen is stored inside the tank. It is also possible to combine pressure and temperature with cryo-compressed hydrogen gas storage, which can further improve the gravimetric index. In exchange, the risks of both high pressure and cryogenic temperatures are present in this storage type. Other types of hydrogen storage are also in development, like storing it in a metal framework or in a chemical bond like Ammonia [13].

Specific power

The fuel cell system that is used to generate electrical power from hydrogen does not scale directly with the size of the hydrogen storage system and an additional mass is added to the total mass of the hydrogen energy storage system that scales with the required power of the load. The specific power of a fuel cell system is defined as the rated output power of a fuel cell system compared to the weight of the fuel cell stack in addition to the weight of secondary systems that are required to operate the fuel cells. These secondary systems can already include a DC/DC converter for some manufacturers. Table 2.1 shows a number of available fuel cell systems, their output power, mass and specific power given in their respective datasheets. A number of systems around 100 kW reach a specific power from 0.4 to 0.6 kW/kg and the same is found for systems around 2 kW with a specific power of 0.5 kW/kg. Systems in the range of 20-30 kW are less common and appear to have a worse specific power in general only 0.21 kW/kg at best. For reference, the fuel cell stack at the core of the PowerCell Power Generation System 30 is a 35.5 kW V-stack that weighs 35.9 kg. This means that only about 1/4th of the weight of the fuel cell system comes from the stack itself. For the Power Generation system 100 this is even more pronounced where only 1/5th of the weight of the system comes from the fuel cell stack [14]. The density of the fuel cell systems is 0.6 $\frac{kg}{L}$ on average. The Clean Sky 2 report [3] states that the specific power of current fuel cell systems can reach about 0.75 $\frac{kW}{kg}$ and that it needs to be improved to 1.7 $\frac{kW}{kg}$ for regional transportation.

Table 2.1: Table of power densities in fuel cell systems

Manufacturer	Product name	Power (kW)	Mass (kg)	Specific power ($\frac{kW}{kg}$)
H3Dynamics	AEROSTAK A-1500	1.5	3.0	0.50
Intelligent energy	IE-SOAR 2.4	2.4	4.8	0.50
Intelligent energy	IE-DRIVE P100	110	240	0.46
PowerCell	Power Generation System 30	30	145	0.21
PowerCell	Power Generation System 100	100	212	0.47
PowerCell	Heavy duty system 100	100	170	0.59
Ballard	FCmove-HD+	100	260	0.38
Plug Power	ProGen 30	30	257	0.12
Plug Power	ProGen 100	125	363	0.34
Loop Energy	S300-S	28	274	0.11
Loop Energy	S505-S	48	381	0.13

2.1.4   Power electronic converters in aircraft

To design a power electronic system that can be used in aircraft, a number of challenges need to be considered. The converter needs to be resistant to rough conditions, like strong vibrations and low pressure environments. At 3660 m, the service ceiling of the Velis Electro, pressures drop to around 64 kPa. At these pressures the insulation of air is decreased following Paschen's law, making it easier for arcs to form. Like with the energy storage systems, the mass and volume of a converter system should also be reduced as much as possible. High safety requirements may also place additional requirements on reliability and redundancy. Once more the Velis Electro can be used as a reference on state of the art power electronic systems. In the aircraft the permanent magnet machine is controlled by a H300c inverter with a mass of 8 kg, volume of 7.1 L and rated output power of 90 kW. This results in a specific power of 11.3 $\frac{kW}{kg}$ [15] while also meeting aviation specific requirements.

2.2   System overview

A hybrid fuel cell battery electric aircraft can take many shapes, ranging from seating just a pilot for short distances to large passenger aircraft for further distances. To narrow down on the many options in different components and size some general requirements on the functionality and architecture of the system are set.

2.2.1   Pipistrel Velis Electro

As mentioned, the Pipistrel Velis Electro is a type-certified battery electric aircraft. The aircraft uses energy stored in 2 parallel connected Lithium-ion battery packs and has enough energy for a flight duration of up to 50 minutes [2]. At this point in time it is the only type certified battery electric aircraft. This means that it can be used to get a sense of the sizing and requirements of different components in a battery electric aircraft.

Existing propulsion system

A summary is made on the subsystems of the aircraft that are of interest for power and energy distribution in the aircraft. This includes the battery packs, 400 to 12 V DC/DC converter, 13.2 V battery, motor and motor controller.

The two main battery packs can store around 30 Ah each at a voltage between 260 and 394 V. The maximum discharge current is 120 A, resulting in a peak power of about 47 kW [8]. Many other systems, like the avionics and battery management systems take power from a 12 V bus. This bus is primarily powered by a DC/DC buck-converter that is connected to the high voltage system. An auxiliary battery is present to buffer this voltage and to maintain the voltage when the connection to the high voltage system is interrupted.

Finally, the electric engine is packaged as the E-811 by Pipistrel, consisting of the 268 MV LC VHML electric motor and the H300C motor controller. The electric motor is an axial flux permanent magnet synchronous machine with 57.6 kW as a maximum power for up to 90 seconds and 49.2 kW continuously.

The H300C three phase inverter used to drive the machine should be operated between 250 and 400 V and is able to supply a current of up to 311 A for a short time and 226 A in continuous operation [15]. The battery voltage can go as low as 260 V, resulting in a converter power of 58.8 kW for continuous operation and 80.9 kW in peak loads. This means that the inverter does not put additional constraints on the operating conditions of the engine. The existing battery electric system is summarized in the diagram shown in Figure 2.1.
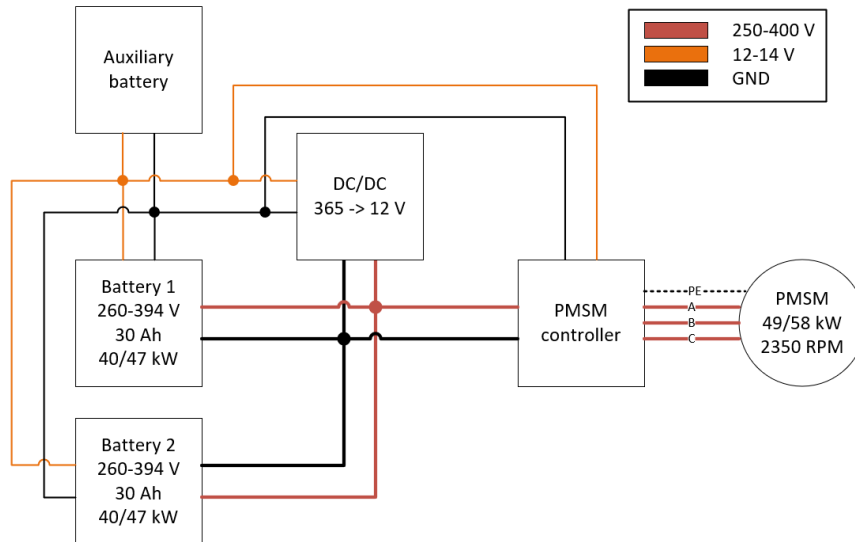
Figure 2.1: Diagram of the Velis Electro propulsion system

Load profile

The motor power and RPM of the Velis Electro can be characterised for different periods during a flight. A normal flight from location A to B is shown schematically in Figure 2.2. The flight starts with a pulse of around 3 kW at 700 RPM used for taxiing, where the aircraft moves to the start of the runway. After a small wait there is a sharp peak in the power to 60 kW at 2450 RPM, here the velocity of the aircraft is increased until takeoff, this period lasts about 15 seconds. Once the aircraft has left the ground, the power is reduced to 40 kW at 2250 RPM, enough to keep the aircraft in the air and to climb to higher altitudes. Once the desired altitude is reached after about 1.5 minutes, the power is reduced even further to cruising power at about 20 kW and 1900 RPM, exactly enough to maintain the velocity and altitude. Once the destination is reached the power is reduced to 0 kW which allows the aircraft to descent until touchdown, in this period the propeller retains about 1200 RPM. Back on the ground a final peak of 3 kW at 700 RPM is used to taxi away from the runway. The output power for a certain RPM depends on the current airspeed of the aircraft and is non-linear.
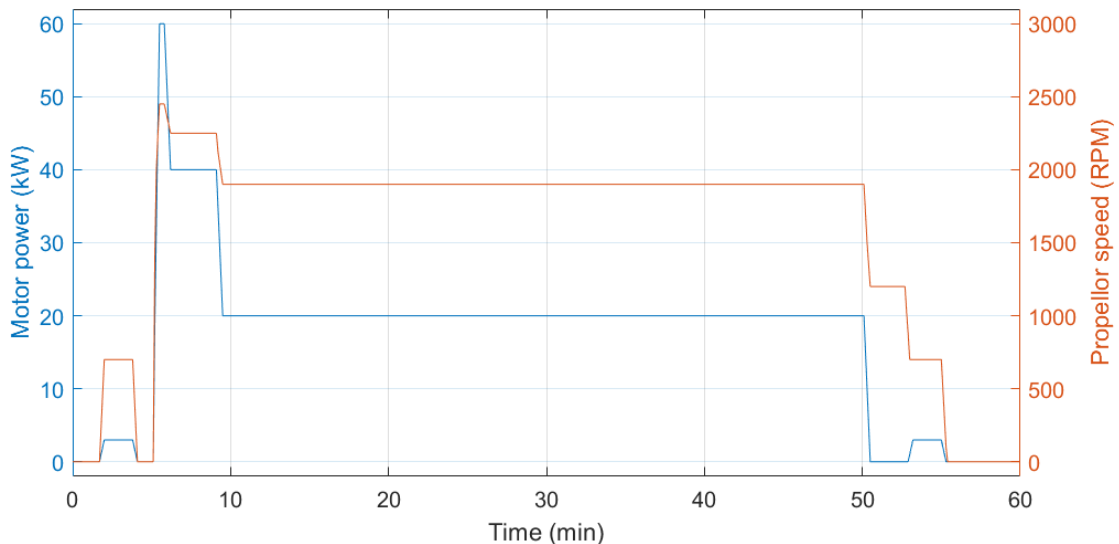
Figure 2.2: Simplified loading curve of a flight from A to B

In an actual flight the profile can get more complicated, the climb power changes depending on the desired climb rate, the cruise power can fluctuate depending on changes in wind speed and the altitude may be changed somewhere during the flight introducing multiple climb and descend phases.

A second flight profile is introduced in Figure 2.3 which is based on data from test flights where the aircraft goes through repeated touch-and-go landings at the same airport. Such a flight can be used to test certain systems or in the training of pilots which is the main intended purpose of the Velis Electro [2].

Figure 2.3: Simplified loading curve of a repeating touch-and-go flight

2.2.2 Fuel cell system requirements

A hydrogen fuel cell system is considered to be a viable solution for extending the range of the Pipistrel aircraft. The main task of this system will be to add power to the system during a flight, sharing the load with the battery packs. To significantly increase the flight time, the fuel cells should be capable of taking the bulk of the load during the cruise period of the flight. In the given load curves that amounts to about 20 kW. At this load, a voltage of about 200 V at a current of 10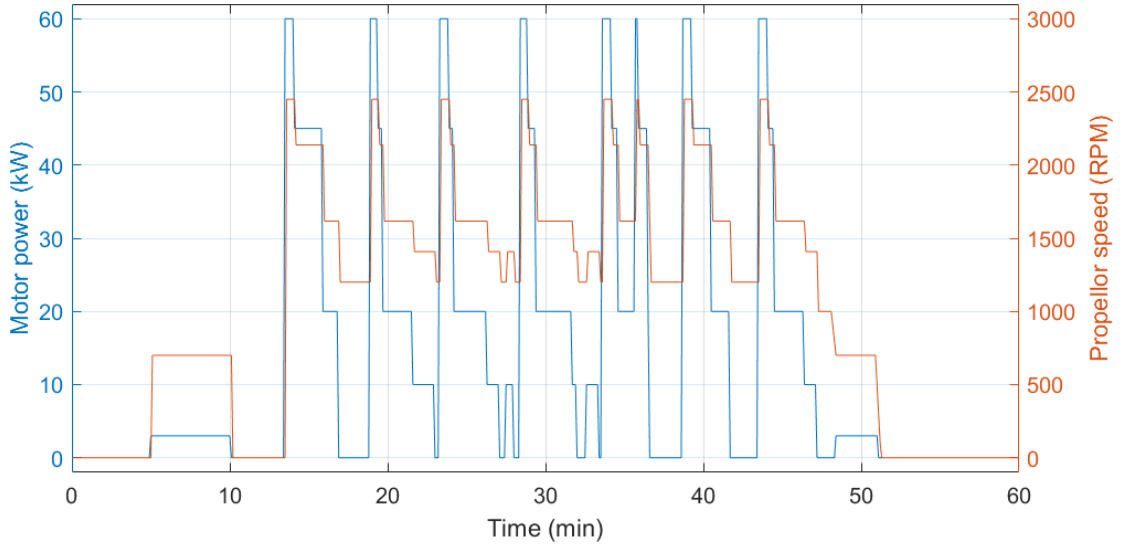0 A is expected, using the PowerCell V-stack as a benchmark [16]. To significantly increase the flight time of the aircraft, a goal of 2 additional hours at cruise load is set. In the other load states, the fuel cell can also provide power. The choice is made to run the fuel cell system in idle during the taxi and descent phases and in full power during the takeoff, climb and cruise phases.

Mass budget for the power electronics

Using the analysis on state of the art systems, a specific power of $0.5\frac{kW}{kg}$ can be expected of the fuel cell system. For the required 20 kW, with some headroom in power, this corresponds to a mass of 50 kg. The H2 tank will also add a significant amount of mass to the system, with a tank gravimetric index of 15% for current liquid hydrogen storage systems [3], a fuel cell efficiency of 50% and an electric energy requirement of 40 kWh, the storage tank mass is calculated to be around 20 kg. Resulting in a total mass of 70 kg for the entire hydrogen electric energy storage system. These two subsystems already eat up a fair share of the available 172 kg of payload that Pipistrel can cary [2]. This payload currently includes the pilot and passenger. The added weight of the fuel cell system can be compensated for by removing the passenger from the aircraft. Assuming pilot and passenger both accounted for half the payload, this would leave 16 kg for any additional systems including the power electronics required to connect the fuel cells to the rest of the system. As the mass of the existing PMSM controller is 8 kg, it should be possible to fit at least one additional converter into the system.

2.3 Hydrogen fuel cell systems

In an attempt to improve the range of the battery electric aircraft, a hydrogen fuel cell system is considered. As stated before, Proton exchange membrane fuel cells using pure hydrogen and air as fuel are considered in particular. By looking at the dynamic behavior of such a system, a power and energy distribution design can be made that incorporates the two energy storage systems.

2.3.1 Basic reaction

In proton exchange membrane fuel cells a combination of two half half-reactions converts hydrogen and oxygen into water. At the anode side of a fuel cell, hydrogen molecules are split into 2 hydrogen ions and 2 electrons as shown in Equation 2.1.

$$2H_2 \rightarrow 4H^+ + 4e^- \tag{2.1}$$

The hydrogen ions can diffuse through a membrane to the cathode side where oxygen is present. Electrons can't pass through the membrane and a potential difference is created between the electrodes. With a current through an external load electrons can rejoin with the hydrogen ions and oxygen to create water as shown in Equation 2.2. This means that hydrogen should be fed in at the anode side and oxygen at the cathode side. Which can either be in the form of pure oxygen or a mixture like air.

$$O_2 + 4H^+ + 4e^- \rightarrow 2H_2O \tag{2.2}$$

One ideal fuel cell creates an open circuit voltage of 1.23 V between the electrodes. To boost this voltage, a number of these cells are connected in series to create a fuel cell stack.

2.3.2   Secondary systems

A number of secondary systems are required to sustain the reaction in the fuel cells and to optimize the efficiency of the reaction. The controllable variables that influence the reaction are: the temperature of the fuel cells, the humidity of the membrane and the concentration of hydrogen on the anode side and oxygen on the cathode side.

Thermal management system

The reaction of hydrogen and oxygen to water and transportation losses of the electrons release heat into the fuel cell. The efficiency of the system depends on the temperature of the fuel cell and the optimal temperature is often above the environment temperature, this means that the fuel cell needs some time to reach the desired temperature upon startup. Once the fuel cell is at the desired temperature a cooling system is required to prevent the fuel cell from heating up further which could cause damage to the system. Either air, liquid or two-phase cooling can be used, depending on the requirements of the system.

Humidity management

The fuel cells need an appropriate level of humidity to sustain the reaction of hydrogen and oxygen. New water is generated by this reaction but this water can be removed with exhaust gasses. As the outflow of water through the exhaust is generally greater than the flow of water generated by the system, a humidity management system is required to prevent the fuel cells from drying out. This can be done with active injections of water into the ingoing air stream or by a passive exchange of water and heat between the ingoing and outgoing air streams through a membrane. With active injection the humidity can be controlled directly but with passive water transfer the humidity depends on the amount of air flow, humidity of the environment and temperature of the air.

Hydrogen concentration management

The amount of fuel consumed by the reaction inside the fuel cells needs to be continually replaced to sustain the reaction. For hydrogen stored in high pressure tanks this is rather straightforward and can be achieved with a pressure regulator, by sustaining the pressure any amount of hydrogen consumed is replaced by more hydrogen. Other storage technologies like liquid hydrogen storage or chemical storage like ammonia require an active system to convert the stored hydrogen into the standard temperature and pressure gaseous hydrogen. To prevent the accumulation of impurities in the hydrogen, a loop can be created to recirculate the hydrogen with a pump, where water can also either be added with a humidifier or removed with a water separator.

Oxygen concentration management

The oxygen concentration is harder to manage when it is taken from the environment. A pump is needed to introduce new oxygen into the system or a compressor may be needed when the system is run above ambient pressure. The flow rate of air often exceeds the amount that would be needed to exactly supply the required oxygen. This oxygen excess ratio is often between 2 and 3 to leave enough oxygen for cells at the end of the air flow path. Using this ratio the required air flow rate can be calculated from the oxygen concentration in the air and the output current of the fuel cell. When a passive humidification system is used, the humidity of the air going into the fuel cell can not be controlled independently and will depend on the flow rate of the air. This can put boundaries on the amount of air that is fed into the fuel cell to maintain the correct humidity in the cell membrane [17].

2.3.3 Steady state model

A model of a PEM fuel cell can help with understanding the response of a fuel cell to different converter architectures and control strategies. First, a steady state model is explored that results in the well known polarization curves.

Nernst voltage

The reaction of hydrogen and oxygen in the fuel cell generates an EMF or reversible voltage. Chapter 2 of Larminie and Dicks [17] derives the reversible voltage of a hydrogen fuel cell based on the Gibbs free energy, temperature and pressure. Table 2.2 in the book shows the maximum EMF at a range of temperature, for low temperature PEMFC's a linear fit can be made for the temperatures between 25 and 80 °C. In addition to this, the reversible EMF depends on the concentration and pressure of the fuels and products, the output of this equation is called the Nernst voltage. A final equation for the reversible voltage is shown in Equation 2.3. Here P_x is the partial pressure of substance x in bar, R is the ideal gas constant, F is Faraday's constant and T is the temperature of the fuel cell in K.

$$E_r = 1.229 - 8.46 * 10^{-4}(T - 298.15) + \frac{RT}{2F} \ln\left(\frac{P_{H2}\sqrt{P_{O2}}}{P_{H2O}}\right) \tag{2.3}$$

Voltage losses

The voltage measured at the output of the fuel cell does not equal this reversible voltage as some losses need to be considered. These losses are often divided into three parts, the activation, concentration and Ohmic losses. With a resulting output voltage as shown in Equation 2.4. These losses are often given based on current densities in $\frac{A}{cm^2}$ but these densities can be scaled with the active area of the fuel cell to get a current.

$$v_{cell} = E_r - v_{act} - v_{conc} - v_\Omega \tag{2.4}$$

Activation losses

The first of these losses considered is the activation loss. Which is caused by the slowness of the reaction in the fuel cell. This loss causes a steep decline in the voltage at lower current densities. An equation for this effect is shown in Equation 2.5 [17], it is a logarithmic equation based on a reference exchange current density i_o, a leakage current density through the membrane i_n, a charge transfer coefficient α and the thermal voltage $V_T = \frac{RT}{F}$. The activation losses depend on the temperature of the fuel cell and the temperature can be adjusted to minimize these losses, reaching an optimum around 80 °C as found by Song et al. [18].

$$v_{act} = \frac{RT}{\alpha F} \ln\left(\frac{i_n + i_{cell}}{i_0}\right) \tag{2.5}$$

When this equation is rewritten as seen in Equation 2.6, it can be split into a constant and a current dependent part. The constant part is also present when the current is zero and changes the open circuit voltage of the cell.

$$\frac{RT}{\alpha F} \ln\left(\frac{i_n + i_{cell}}{i_0}\right) = \frac{RT}{\alpha F} \ln\left(1 + \frac{i_{cell}}{i_n}\right) + \frac{RT}{\alpha F} \ln\left(\frac{i_n}{i_0}\right) = v_{act-diode} + E_{act} \tag{2.6}$$

The current dependent part of the equation resembles the Shockley diode equation. This can be seen better by inverting the current dependent part of Equation 2.6, which results in Equation 2.7. This means that the full activation loss can be modelled as a constant voltage drop in series with a forward biased diode with saturation current density i_n and ideality factor $\frac{1}{\alpha}$.

$$i_{act} = i_n \left(e^{\frac{v_{act-diode}}{\frac{1}{\alpha} v_T}} - 1\right) \tag{2.7}$$

Ohmic losses

The second loss in the fuel cell are the Ohmic losses, this is a combination of different linear resistances in the path of the electrons. Equation 2.8 shows the voltage drop based on a bulk resistance value r_i in Ωcm^2 [17]. The value of this resistance is shown to mostly depend on the resistance of the membrane which can change significantly based on temperature (T) and the water content (λ) of the membrane [19].

$$v_\Omega = r_i(T, \lambda) i_{cell} \tag{2.8}$$

Concentration losses

The final loss are the concentration losses, which are caused by a drop in the concentration of fuels at the membrane when a large amount of fuel is consumed and it can't be replenished fast enough. This drop in concentration at the reaction interface results in a drop in the Nernst voltage from Equation 2.3. The drop in the voltage compared to the open circuit voltage can be extracted and is given in Equation 2.9, here the output voltage goes to 0 at the limiting current density i_L. Once again, the equation fits the Shockley diode equation with a saturation current of i_L and ideality factor of $\frac{1}{2}$ as shown in Equation 2.10. Here the diode is placed in reverse bias, having a very large leakage current. The concentration loss is also found to change depending on the temperature, where the limiting current density increases at higher temperatures [18].

$$v_{conc} = -\frac{RT}{2F} \ln \left(1 - \frac{i_{cell}}{i_L} \right) \tag{2.9}$$

$$i_{conc} = -i_L \left(e^{\frac{-v_{conc}}{\frac{1}{2}v_T}} - 1 \right) \tag{2.10}$$

Polarization curve

The different losses in the fuel cell can be combined as was shown in Equation 2.4. When the required parameters are found at a certain temperature, pressures and water content, an iv curve can be created. Using some example parameters from a polarization curve can be generated as shown in Figure 2.4 [20, fig 3-8]. As stated before, most parameters depend on conditions like the temperature and age of the fuel cell and the optimal operating point of the fuel cell changes with the required load.
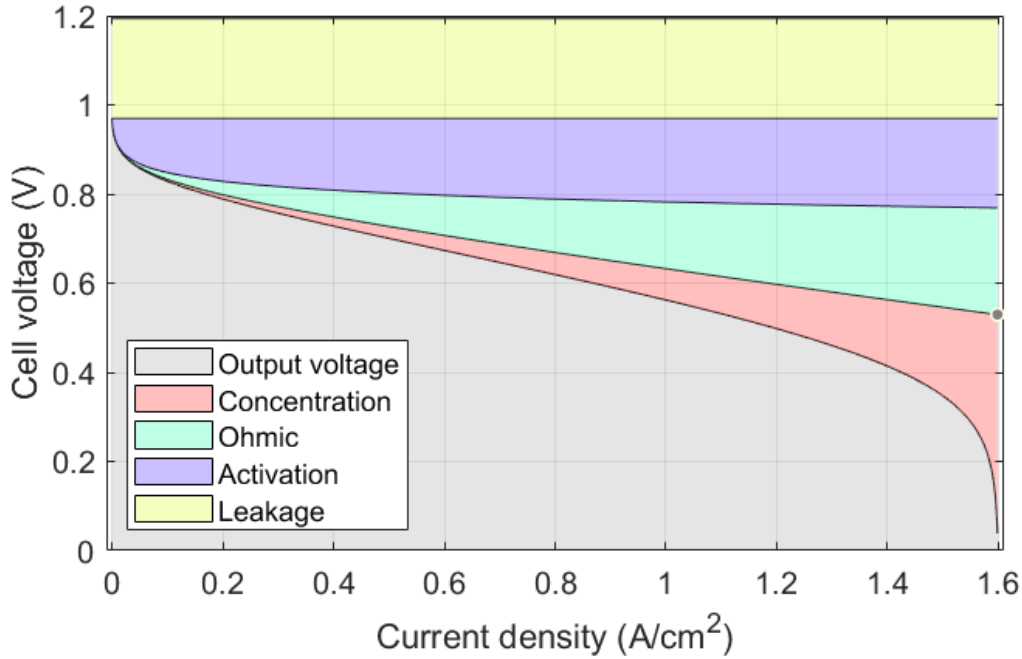
Figure 2.4: Typical polarization curve

2.3.4 Degradation mechanisms

A large challenge with implementing fuel cell systems in general are the durability and cost of the system [21]. By looking at the mechanism behind degradation of the fuel cell, the system lifetime can be optimized. Three degradation mechanisms are considered that can be influenced by external decisions: startup and shutdown, idling and dynamic loading [22].

Startup and shutdown

At startup and shutdown of a fuel cell, an interface of air and hydrogen can exist in the anode when the hydrogen supply is connected or disconnected. This interface generates a potential difference up to 1.5 V and can cause

damage to the catalyst layer in the cathode [22]. To minimize the effects of this behavior, the fuel cell system should be turned on and off as few times as possible. Ideally, the system is turned on before flight and kept operational for the entire duration of a flight mission.

Idling

After startup, some power is required to operate the secondary fuel cell systems. At this limited current density, a high potential is present in the cells and gas crossover is large, both resulting in degradation of the cells [22]. This means that the fuel cell system should not be turned on much earlier than required. In addition it may be wise to apply a base load to the fuel cell. This could be done by implementing an upper potential limit around 0.85 V per cell [23].

Dynamic loading

The dynamic model of the fuel cell showed that a fuel cell stack can respond well to rapid fluctuations in the load, this would suggest that a fuel cell system could be used to power a dynamic load on its own. It turns out that this is in fact not the best approach due to the large impact of dynamic loading on the fuel cell degradation [24]. In addition, limiting the rate of change in the load does not appear to decrease the degradation as shown in the similarity in results with square wave and trapezoidal wave cycling patterns [23]. The suggested approach is to set a fixed load for the fuel cell with only a limited number of changes in this load during a flight.

2.3.5 Equivalent circuit model

Starting from the polarization curve, additional behavioral aspects can be included to create a better model of a fuel cell in a dynamic situation. One parasitic element that is often included in equivalent circuit models is the double-layer capacitance that describes the build up of charge at the interface between electrode and the membrane [17]. This capacitance is placed in parallel to the activation and concentration losses. This capacitance smooths the a change in the output voltage and improves the dynamic behavior of the cell. The capacitance can take on large values in the order of a whole Farad and have a time constant in the order of 0.1s [25]. The final equivalent circuit model for a single fuel cell is shown in figure 2.5.
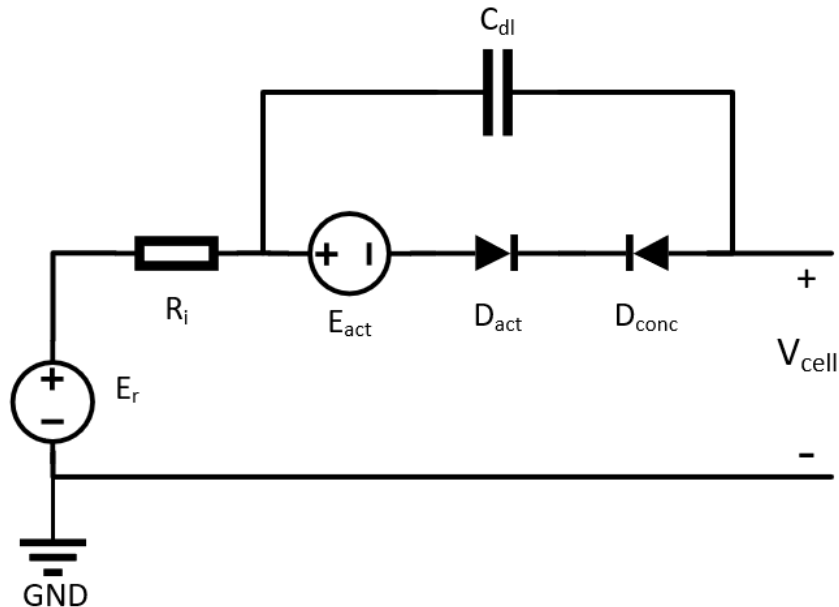

Figure 2.5: Equivalent circuit model of a single PEM fuel cell

The parameters in the circuit can be set to fixed values based on a steady state reference. This is a reasonable assumption on timescales below or around 1 second as the temperature and humidity of the fuel cell as well as the flow rate of the fuels take a longer time to reach a new steady state [25]. The step response can be split into two phases, a first-time delay and second-time delay [26]. For high frequency behavior and simulations the first-stage delay should give sufficient information. For longer simulations, regarding energy distribution for example, the second-time delay should be taken into account. This second stage behavior does depend a lot on the fuel cell control system and the time constants of secondary systems, which can vary a lot.

Modelling multiple cells

Thus far the fuel cell behavior is considered based on current densities of one cell. To convert the model to a stack of real cells with a known area A and N cells in series, the different parameters need to be scaled. The constant activation voltage and nernst voltage can be combined into an constant open source voltage as shown in Equation 2.11.

$$E_{oc} = N \left(E_r - E_{act} \right) \tag{2.11}$$

The internal membrane resistance of one cell is inversely proportional to the area of the cell, this is then multiplied by the number of cells in series and the total Ohmic resistance is found as shown in Equation 2.12.

$$R_i = \frac{N r_i}{A} \tag{2.12}$$

The double layer capacitance actually grows larger with the surface area of a cell but multiple capacitors in series decrease in size. This results in the relation shown in Equation 2.13 where c_{dl} is the area specific capacitance in $\frac{F}{cm^2}$.

$$C_{dl} = \frac{c_{dl} A}{N} \tag{2.13}$$

Next the logarithmic behavior of the activation voltage is considered. The voltage drop over a number of diodes in series can be added together and the current through the diodes can be converted back into a current density using the cell area. The resulting diode voltage is shown in Equation 2.14.

$$V_{act-diode} = N \frac{RT}{\alpha F} \ln \left(1 + \frac{I_{act}}{A i_n} \right) \tag{2.14}$$

By expressing this relation based on the current as shown in Equation 2.15 it can be seen that the total voltage drop of the activation polarization can be modelled with a diode with a saturation current of $A i_n$ and an ideality factor of $\frac{N}{\alpha}$.

$$I_{act} = A i_n \left(e^{\left(\frac{V_{act-diode}}{\frac{N}{\alpha} V_T} \right)} - 1 \right) \tag{2.15}$$

Finally, the relation between current and concentration losses can be adjusted as shown in Equation 2.16. The full concentration losses can now be modelled as a reverse biased diode with saturation current $A i_L$ and ideality factor $\frac{N}{2}$.

$$I_{conc} = -A i_L \left(e^{\left(\frac{-V_{conc}}{\frac{N}{2} V_T} \right)} - 1 \right) \tag{2.16}$$

Step response

The dynamic behavior of the fuel cell model can be observed by applying a step response in the fuel cell current. A stack with 50 cells and an area of 20 cm^2 per cell is tested using the polarization curve parameters from Figure 2.4 and a specific capacitance of $1 \frac{F}{cm^2}$ for the double layer capacitance of one cell. Figure 2.6 shows the result of instantaneously increasing the current from $100 \frac{mA}{cm^2}$ to $1100 \frac{mA}{cm^2}$ and back down after 2.5 seconds. The responds shows an instantaneous drop due the Ohmic resistance followed by an exponential decay due to the RC circuit of double layer capacitance and activation and polarization losses.
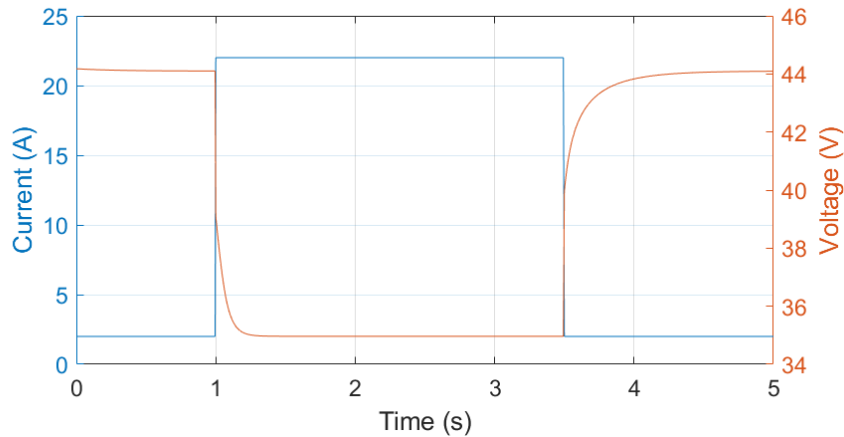

Figure 2.6: Example step response of the fuel cell equivelant circuit model

Scaled polarization curve

To get a representative model for a 30 kW fuel cell system, the polarization curve in Figure 2.4 is scaled to correlate with the 264 cell Powercell V-stack. This is achieved by using $N = 264$, to match the series cell count, and $A = 190\ cm^2$ to match the cell voltage at 150 A. The resulting polarization curve is shown in Figure 2.7. With these parameters, a effective double layer capacitance of 0.3 F is expected. The cruise operating point of 20 kW is now found at 178 V and 112 A. The idle operating point, where the cell voltage should stay below 0.85 V is set at 4 kW. At that point the cell voltage is around 0.83 V, the stack voltage 219.4 V and the output current 18.2 A.
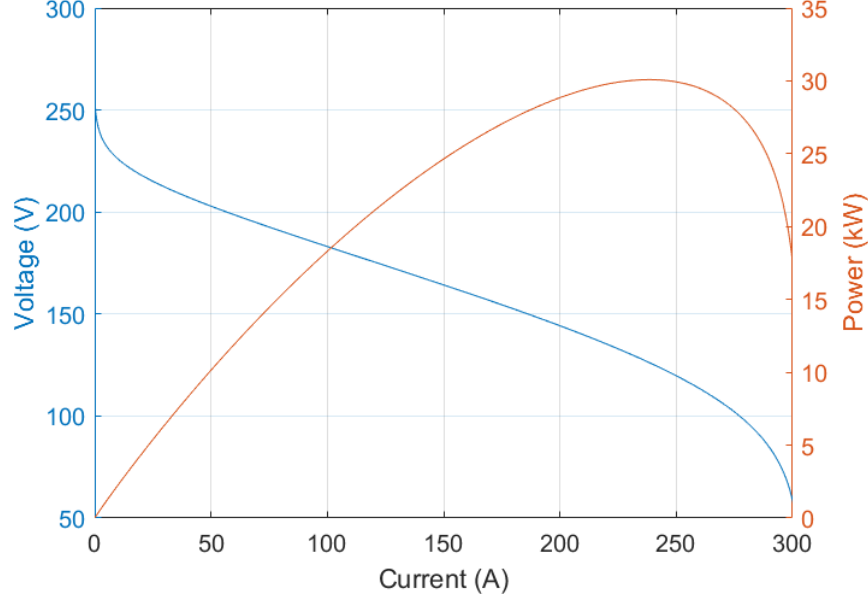

Figure 2.7: Scaled fuel cell polarization curve

2.4 Lithium ion battery packs

The Pipistrel Velis Electro currently uses energy stored in two lithium ion battery packs to power the electric drive and secondary systems. An analysis is done to find possible challenges or improvements to such a battery electric system.

2.4.1 Basic operation

A lithium ion battery is a specific method of storing electrical energy as chemical energy. This process is similar to that in a fuel cell but in a battery all of the fuel is stored inside the electrode, not fed by an external source. This means that the battery cell does not require secondary systems to maintain the output voltage. In exchange, the available charge of the cell, called the state of charge (SOC), influences the output voltage of the cell. Battery packs do often include a battery management system (BMS) that may monitor voltages and currents of the pack, have communication with other systems or implement some safety measures.

The cathode material used in the Pipistrel PB345V124E-L battery pack is a based on a nickel manganese cobalt oxide. Here a half reaction takes place as shown in Equation 2.17. For structural stability of the material, not all lithium can be extracted from the cathode [27], limiting the total charge that can be stored in the cell.

$$NiMnCoO_2 + Li^+ + e^- \leftrightarrow LiNiMnCoO_2 \tag{2.17}$$

The anode material used in most lithium batteries is graphite. The graphite material can be fully depleted from lithium. The half reaction in the anode is shown in Equation 2.18.

$$LiC_6 \leftrightarrow C_6 + Li^+ + e^- \tag{2.18}$$

As was the case in the fuel cell, the Li^+ ions can move between the anode and cathode through a membrane, leaving behind electrons that can pass through an external circuit.

Open circuit voltage

The voltage generated by the reactions inside a battery cell depends heavily on the temperature and the state of charge of the battery as well as possible aging of the battery over time. A similar analysis as with the fuel cells can be done with the Nernst voltage, gaining some insight in the dependency on concentration of reactants and the temperature. It appears however, that these dependencies are more complicated and can not be properly described using a set of theoretical equations. The other option is to use a fit equation for the relation between the open circuit voltage and the state of charge. There are a number of different fitting functions used in literature [28]. These fit functions go from a basic polynomial fit to more specific functions with exponential, Gaussian or logarithmic components. It is important to note that such a fit only holds true for specific conditions, including temperature and age, and would ideally be adjusted accordingly. Equation 2.19 [28, eqn 1] shows the exponential fit function used further analysis. This function has a small number of parameters and is well defined when the state of charge is 0 or 1.

$$V_{oc} = a_1 e^{b_1 SOC} + a_2 e^{b_2 SOC} + cSOC^2 \tag{2.19}$$

The exact point at which the battery is considered full and empty, or the state of charge being equal to 0 or 1 also depends on which definition is used. Using an open circuit voltage of 4.1 as full and 2.85 V as empty, an example curve as shown in Figure 2.8 is created.
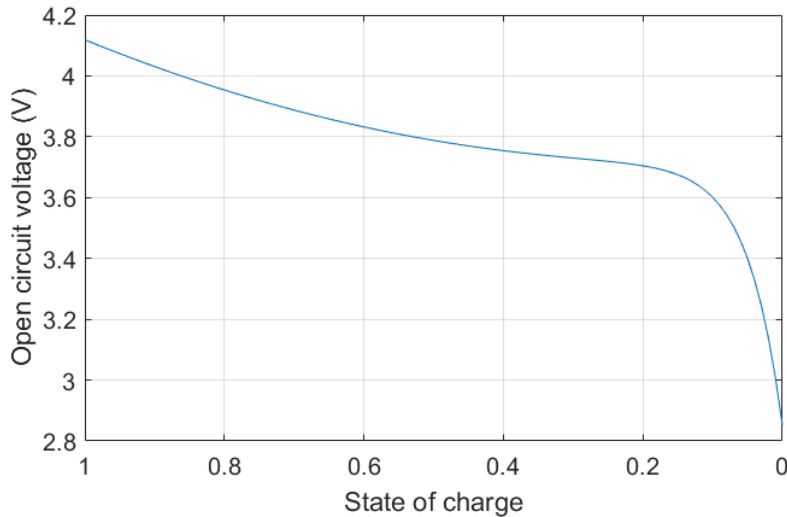

Figure 2.8: Example curve for the relation between state of charge and the open circuit voltage

2.4.2 Equivalent circuit model

To look at the dynamic behavior of a battery, another equivalent circuit can be applied. A number of different models can be created using standard linear circuit elements, depending on the desired accuracy [29]. The most simplest of these is a voltage source for the open source voltage, some internal resistance and finally a parallel RC pair. This is a very similar model to that of the fuel cell, using a linear resistance instead of the logarithmic activation and concentration losses. This model can be expanded with additional RC pairs, resulting in a higher level dynamic response and a more accurate model. If a measure of the impedance of a battery over a number of frequencies is made using impedance spectroscopy, it is possible to find a fit for the circuit parameters. For even more accurate measurements of the state of the battery, exotic circuit elements are used like the Warburg element or constant phase elements. These elements better fit the measurements of the impedance spectroscopy [30]. A challenge of these elements is the complexity when used in time domain simulations, where high order linear systems are required to represent a Warburg element [31]. A second order RC circuit is deemed to be a good balance between accuracy and simplicity. This circuit is shown in Figure 2.9. This circuit also holds for a battery pack with S series cells in P parallel strings. Where the open circuit voltage scales with S, the resistances scale with $\frac{S}{P}$ and the capacitances scale with $\frac{P}{S}$.
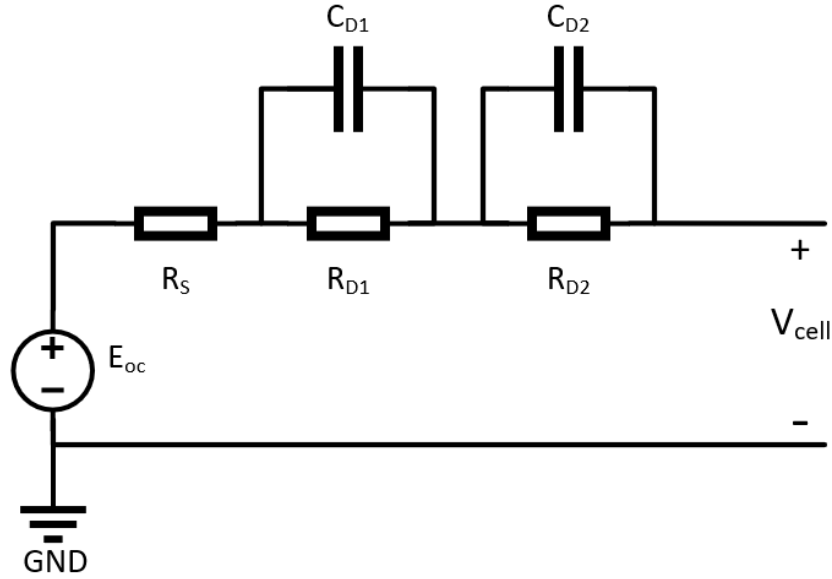
Figure 2.9: Equivalent circuit model of a single Lithium Ion battery cell

Battery pack parameterization

The flight data of the Pipistrel also includes information regarding the state of the battery packs. This information can be used to calibrate the models used for the output voltage of the battery packs. In this process, measurements on one of the two battery packs is used to create a model which is later used for both packs in parallel. The relation between the open circuit voltage and state of charge is considered with the flight data from Figure 2.3. Each time the aircraft was in descent the current of the battery packs was close to zero, after the RC behavior in the output voltage leveled out, a measurement could be done on the open circuit voltage. These voltages could be corresponded to the state of charge that is also stored in the flight data. As the battery packs should never go near empty, no source of the battery voltage is available. The empty battery voltage is estimated instead, at 300 V. The output voltage under load can go even lower, with 260 V listed as the minimum voltage and at full load the voltage is observed to drop around 40 V.
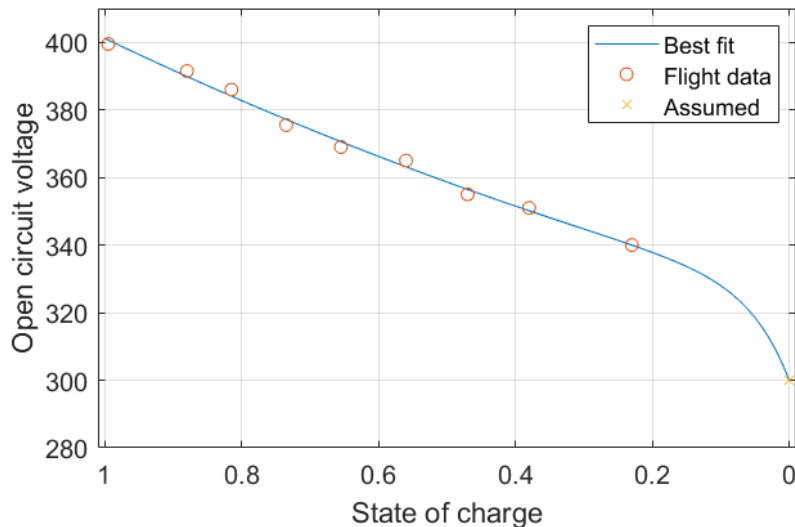
Figure 2.10: Fit of open circuit voltage and state of charge

Next, the voltage drop over the internal losses of the battery can be found looking at the difference between open circuit voltage and the output voltage at different points in the flight. The result is an estimate of $R_s = 0.26$ Ω, $R_{D1} = 0.2$ Ω, $C_{D1} = 250$ F, $R_{D2} = 0.05$ Ω and $C_{D2} = 100$ F. The time constant of the first RC circuit is 50 seconds and the second 5 seconds. Any behaviour is on a faster timescale is hard to describe as the sample time and resolution of the flight data are limited. For any fast simulation where converters are tested for example,

the capacitive elements will have a very low impedance and a simplified circuit with the open circuit voltage and internal resistance R_s appears to be sufficient.

2.4.3 Operational challenges

The use of lithium ion batteries comes with some challenges regarding safety, durability and functionality. By looking into some of these challenges, it can be possible to set some rules on battery utilization like with fuel cells. Here the focus is on the normal operation of a battery pack and the interaction with other systems.

Overcharging

Before a flight, the battery packs need to be charged. Currently, this only happens once each flight using dedicated hardware outside the aircraft that connects to the battery packs via a charging port. This charging procedure makes sure that the batteries are only charged up to a known maximum. If this charge is exceeded, it would cause damage to the cells internal structure and could result in thermal runaway, resulting in ignition in the worst case [27]. In a fuel cell battery hybrid system, the battery gains an additional function in storing excess power from the fuel cells. It can then occur that the battery is recharged with too much power during a flight. The battery management system is able to disconnect the battery pack when the SOC approaches 100% [8]. To prevent this, the state of charge of the battery should be taken into account by the power and energy management system.

Overdischarging

The battery is considered empty when it reaches a certain cut-off voltage. At that point the state of charge is 0%, but it is possible to extract energy from the system beyond this point, at the cost of damaging the cells, eventually resulting in an internal short circuit [32]. Again, the battery management system will disconnect the pack to prevent any damage to the battery in normal operation. Without the battery packs, the aircraft may run into a lack of available power and this state should be prevented early by the power management system by attempting to minimize the discharging of the battery or even recharging the battery when possible if the state of charge goes towards 0.

Thermal management

Both charging and discharging of the battery will release heat due to the inefficiencies of the system. The temperature of the battery pack should lie between 20 and 40 °C for optimal performance, higher temperatures decrease lifetime and temperatures between 0 and 20 °C have a higher internal resistance and thus a lower efficiency [27]. The Pipistrel battery packs are equipped with a liquid cooling system and an over temperature protection by the BMS. The packs are rated for temperatures between 0 and 45 °C when charging, 0 to 55 °C when discharging and 0 to 35 °C when in storage [8]. When staying within the given maximum power, the heat released by inefficiencies should not form a problem. It can be important however, to prevent the packs from freezing temperatures while in storage. The average power demand on the battery packs is reduced when the load is shared with fuel cells. This reduces the load on the battery cooling system. When operating in a cold environment the lack of heat from internal losses could make it necessary to introduce external heat to the batteries to stay within the rated temperature range.

Short circuit

The batteries can also be damaged when the discharging current is higher than the rated current or in the worst case, the system is short circuited. The battery packs are equipped with 125 A fuses to protect against this scenario. Staying below the rated current should be an important task of the power management system. A short circuit by failures in other systems can turn out to result in tripping the fuse, if and how this could be prevented depends on the power system design.

Aging

A number of different mechanical, chemical and electrical processes introduce imperfections to batteries. These imperfections can grow over time, reducing the maximum charge that the battery can hold as well as increasing the internal resistance. Eventually these processes can also lead to a battery failure [33]. The expected lifetime of a battery system is often based on a number of charge/discharge cycles. This makes sense for fully battery electric systems that charge once before and discharge once during a flight. For a hybrid system a cycle is much harder to define. Having many more cycles of shallow charging and discharging of varying magnitudes. Energy throughput may be a better measure for expected aging of batteries in hybrid systems [33].

3. Comparison of system architectures

A number of system architectures are considered for combining the power from the new fuel cell system to the battery packs and PMSM. First, some general subjects are considered to enable a fair comparison between the designs. The architectures will be represented by functional diagrams, where secondary systems, like EMI filters are assumed to be similar between the designs. The first architecture that is examined uses a boost converter in addition to a three phase inverter like the H300-C inverter of the Pipistrel Aircraft, which will be the benchmark to compare alternative systems with. To reduce the number of systems, and possibly improve the system compared to the interleaved boost converter with inverter system, a number of DC/DC/AC architectures are considered. These examples are based on the overview of dual-DC-port inverters by Neira et al. [34]. Some of these designs are only suited to fixed frequency grid applications and only a few are capable of the large range of frequencies and operating points found in the control of a PMSM. The ones that are considered suitable for use with machines are further tested as such using dynamic models.

3.1 Design rules and comparison

Two architectures can be very different in their functionality and design, this can make it difficult to make a useful comparison between these architectures. A difference might arise not from the architecture itself but from a choice in the component size or type and choices often lead to multiple dependent outcomes. To simplify this problem a number of subjects are generalised for the different designs.

3.1.1 Functionality

The different designs need to work in all loading conditions as found in the load profile in Figure 2.2 for the design to be suited for this application. In addition, the desired fuel cell operating points should be met if possible. It can be possible however, that a design only works in these scenarios when certain conditions are true. Like the battery voltage being higher than 360 V or the rate of change in setpoint variables. These conditions are allowed but should be reasonable.

3.1.2 Switching frequency and losses

Different architectures can have more or fewer switches that switch on and off at different intervals. The voltage and current stress on individual switches can also change between designs. The fundamental switching frequency is set at 48 kHz for each design which will result in similar noise and thus filter requirements between designs. Equation 3.1 shows a formula for the switching losses for a single switch given by Mohan [35], where V_d is the voltage over the switch when it is turned off, I_o the current through the switch when it is turned on, f_s the switching frequency and $t_{c(on)}$ and $t_{c(off)}$ the intervals where voltage and current are present at the switch.

$$P_s = \frac{1}{2} V_d I_o f_s (t_{c(on)} + t_{c(off)}) \tag{3.1}$$

When it is assumed that the same type of devices are used between designs and that the turn-on and turn-off delays are independent of voltage and current, the switching losses can be quickly calculated for different scenarios based on the frequency, voltage and current of the switch. A high current and voltage SiC Mosfet by Microsemi is used as a reference, which has a combined rise and fall time of 22 ns [36]. By adding together the proportional switching losses of all switches in a design, a full measure of the losses can be found, and a comparison can be made between designs. The switching losses do depend on what the operating point of the system is. For the comparison just the measurement at the peak power point of 20 kW for the fuel cell system and 60 kW for the motor output will be used. As the systems are all tested with the same load profile, the relative difference in this one operating point should be representative of the full load profile.

3.1.3 DC current ripples

The switching behavior of power electronics introduces large ripples in voltage and current in the path of power between systems. In general, these ripples are undesired and should be contained within the power electronic system as much as possible. These ripples can be mostly filtered out using passive filters, but there is a trade-off between noise reduction and filter size. A common requirement is set on all designs to have a current ripple of at most 0.2 A_{pp}, both for the fuel cell and battery systems.

3.1.4 Motor current

The different approaches to dual-DC-port inverters can introduce changes to the motor phase currents. Differences arise in the current ripple due to different switching strategies and the main AC current can also be larger in magnitude due to field weakening that can be required to operate certain designs.

3.1.5 Inductor size and availability

A problem with the considered fuel cell system is the large output current, going up to around 110 A at 20 kW. At these levels there are no off the shelf inductors with the required current rating. This makes it challenging to compare different solutions based on the required inductor sizes.

Figure of merit

In order to compare inductors of different sizes, materials and other parameters, a figure of merit is used. The goal is to get the required inductor mass based on the requirements of the design in terms of inductance and rated current.
An analysis is made using the equations on an ideal solenoid. The inductance of such a solenoid is given in Equation 3.2, where L is the inductance, μ the magnetic permeability, A the cross-sectional area, l the length and N the number of turns of the solenoid.

$$L = \frac{\mu A}{l} N^2 \tag{3.2}$$

In addition, the magnetic flux density of this solenoid can be described by Equation 3.3, where B is the magnetic flux density and I the instantaneous current through the solenoid.

$$B = \frac{\mu}{l} N I \Rightarrow I = \frac{Bl}{\mu N} \tag{3.3}$$

These equations can be combined to the figure of merit shown in Equation 3.4 where ρ is the density of the component in $\frac{kg}{m^3}$ and I_{sat} is the peak current through the inducted. Most importantly, the saturation current is squared to remove the number of turns N from the equation. This figure of merit can be calculated using the datasheet of most commercial inductors and only depends on material properties. By comparing with available inductors, inefficiencies in an inductor design are included in the FoM.

$$FoM = \frac{I_{sat}^2 L}{m} = \frac{B_{sat}^2}{\mu \rho} \tag{3.4}$$

A number of commercially available inductors are compared using this figure of merit. A caveat is that the limiting factor of the current in the inductor is not always core saturation as it is also possible for the inductor to overheat due to copper losses at a lower current than the given saturation current. This is given as the maximum DC current by manufacturers. To take this into account, the smallest of the two currents is used when comparing inductors. Table 3.1 shows a list of inductors, mostly selected for their high current rating and inductance, including the properties of interest and the resulting figure of merit. It can be seen that the resulting figure of merit is consistently between 0.1 and 0.3, even though there is a significant variation in inductance, current rating and size. The total required mass of inductors in different designs can be found using a representative value of $0.25 \frac{A^2 H}{kg}$ or $4 \frac{kg}{A^2 H}$.

Table 3.1: Table of commercially available inductors

Manufacturer	Series	Inductance (uH)	Current limit (A)	Mass (g)	FoM ($\frac{A^2H}{kg}$)
Coilcraft	SLC1480	0.17	83.0	5.3	0.221
Coilcraft	SLC1480	0.3	52.0	5.3	0.153
Coilcraft	AGP4233	22	34.0	135	0.188
Coilcraft	AGP4233	33	25.8	135	0.163
Coilcraft	MSS1210	120	2.3	6.0	0.106
Coilcraft	MSS1210	1800	0.63	6.0	0.119
TDK	B82559A	20	21.5	42	0.220
TDK	B82559A	10	36	60	0.216
Würth	WE-HCF	10	32.6	40	0.266
Würth	WE-HCF	22	21.7	35.4	0.293
Würth	WE-HCFT	22	40.6	179.2	0.202
Würth	WE-HCFT	47	31	179.2	0.269
Vishay	IHDF	4.7	59	80.9	0.202
Vishay	IHDM	10	30	61.6	0.146

3.1.6 Capacitor size and availability

The amount of capacitors that are commercially available at these high voltage ratings is also limited. In line with the battery packs, a voltage rating of 500 V or higher will be required. At that voltage range, SMD mount ceramic capacitors are only available up to a couple μF. Through hole film capacitors can have a high rating, going up to a couple hundred μF, like the KEMET C4AQ series [37]. The $210\mu F$, 500 V capacitor from that series weighs 209 grams and has an area of 30 cm^2 with an ESR of 1.6 $m\Omega$ [38]. The capacitor mass is expected to scale linearly with capacitance, which can also be found when multiple smaller capacitors are placed in parallel. This results in an common factor of 1 $\frac{mF}{kg}$, based on the C4AQ capacitor. To limit capacitor size, weight and cost, designs should keep capacitance requirements into account.

3.2 Simulink + PLECS models

The different designs are implemented and tested using the PLECS Blockset in the Simulink environment. Here, a combination of PLECS, Simulink and custom components can be used to create dynamic models of the different systems. These models can then be used to verify and adjust the designs based on the different requirements. Some parts of the models are the same in all systems and will be shown here.

3.2.1 Fuel cell model

The fuel cell system is modelled following the polarization curve described before, in addition to a double layer capacitance. This fuel cell system has an open circuit voltage of 256.1 V. At the cruise power of 20 kW, the voltage levels out at 178 V with a current of 112 A. At idle power of 4 kW the voltage levels out at 220 V and 18.2 A. It was not possible to implement the non-linear voltage drop directly as a voltage drop as a function of the output current however, and it needed to be converted to a voltage dependent resistor. The resulting system still has the same behavior as described initially. Figure 3.1a shows the PLECS model of this fuel cell system, built from a open circuit voltage, linear resistance and nonlinear resistance in parallel to a capacitance. The output voltage and current are measured and can be used by controllers. To enable a faster test of the designs the double layer capacitance was multiplied with a factor of 0.3. This should not significantly alter the behavior at the switching frequency but allows the fuel cell voltage to settle to a new value within 0.1 seconds.

3.2.2 Battery model

The battery packs are modelled as two voltage sources with series resistance. The RC behavior and state of charge dependency of the packs is left out as the simulations will be in the order of a couple of seconds, and these effects are only significant on much longer time frames. The open circuit voltage of the batteries is set to 350 V, corresponding to a state of charge of around 35% and is considered to be a nominal scenario. The resulting model of the battery system is shown in Figure 3.1b.
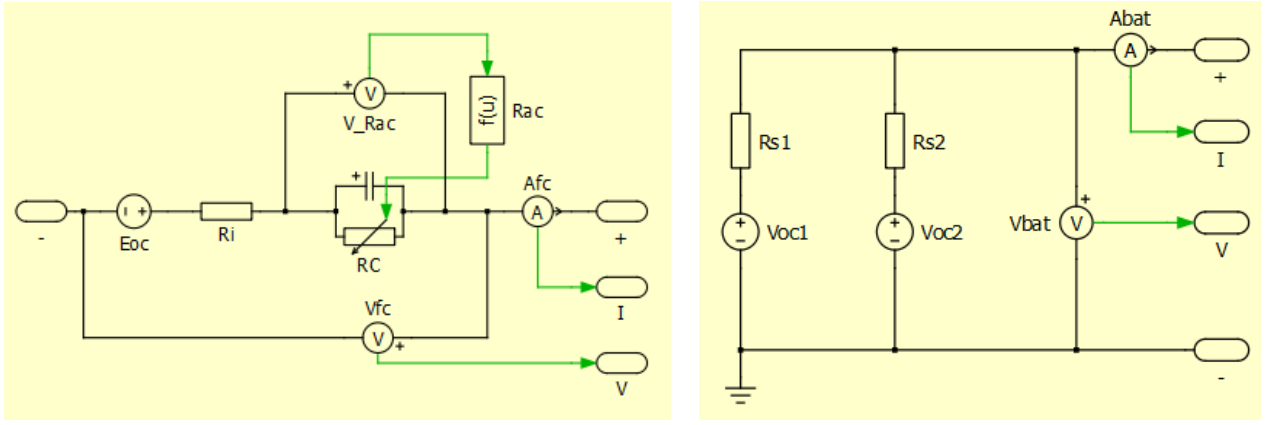
(a) Fuel cell system

(b) Battery packs

Figure 3.1: PLECS models of the energy storage systems

3.2.3 Motor and inverter model

The permanent magnet synchronous machine of the Pipistrel is modeled in PLECS using the standard PMSM block [39], which is able to give a good representation of the machine using parameters found in the datasheet [40]. The machine is assumed to have a symmetrical inductance where $L_d = L_q$ as only one inductance is given in the datasheet. The description of the motor model in the PLECS manual is now simplified and the relation between voltage and current in the DQ reference frame is now modelled as shown in Equation 3.5, where R_s is the internal phase resistance, L the induction of one phase, p the number of pole pairs, ω_m the mechanical angular velocity of the machine and φ_{pm} the magnetic flux of the permanent magnets.

$$\begin{bmatrix} v_d \\ v_q \end{bmatrix} = \begin{bmatrix} R_s & -p\omega_m L \\ p\omega_m L & R_s \end{bmatrix} \begin{bmatrix} i_d \\ i_q \end{bmatrix} + \begin{bmatrix} 0 \\ p\omega_m \end{bmatrix} \varphi_{pm} \tag{3.5}$$

The output torque of the machine is also simplified and is described in Equation 3.6. In turn, when the motor parameters are known the output torque can be indirectly controlled by controlling i_q.

$$T_m = \frac{3}{2}p\varphi_{pm}i_q \tag{3.6}$$

Simplified models of the propeller and the mechanical load are connected to the motor output. The propeller inertia was based on the actual propeller inertia initially, but it was later decreased to allow the motor speed to settle within 0.1 seconds. By adjusting the airspeed it is possible to match the mechanical output power and propeller RPM as observed in the load profile. The resulting model is shown in Figure 3.2b which also includes some sensors required to control the motor. This control is implemented using the standard PMSM Field Oriented Control block from Simulink, which is also common between designs. In addition, Figure 3.2a shows the generic inverter model that comes back in all designs, based on three half bridges, converting a DC voltage to three AC voltages using the incoming PWM signals.
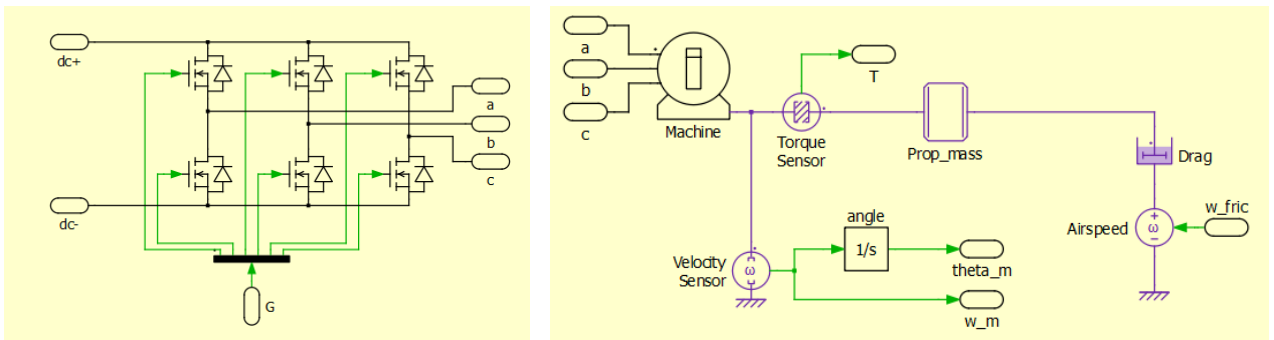
(a) Generic inverter bridge

(b) Model of the motor and mechanical load

Figure 3.2: PLECS models of the output stage

3.3 Interleaved step-up converter and three phase inverter

In the original battery electric architecture of the Pipistrel, the battery pack voltages are used as a varying DC-link voltage for the inverter. If a three-phase DC/AC inverter is used, like the existing H300C, it is also most efficient to not introduce additional converter steps in the battery to inverter line. A DC/DC converter is required however, to integrate the varying voltages of both the battery packs and the new fuel cell system. In this system, the voltage of the battery packs is always higher than that of the fuel cell system with a ratio of 1.2 at 300 V for almost empty battery packs and 250 V for an unloaded fuel cell system, up to 2.5 for a full battery pack at 400 V and a fully loaded fuel cell system at 160 V. With these ratios, a bidirectional boost converter is well suited to transfer power from one DC system to the other.

3.3.1 Interleaving

With the high current requirements seen in high power fuel cell systems, interleaving is often applied to reduce the current ripple and required inductor size of the converter [41]. Commercial examples include the Brusa BDC546 and the Fraunhofer Full SiC Traction 600 A DC-DC Converter. Interleaving works by sharing the load current between N copies of the original topology that switch out of phase from each other. This reduces the ripple in the input and output current by a factor of $\frac{1}{N}$, while also increasing the frequency of the ripple with a factor of N. A simplified diagram of the resulting system is shown in Figure 3.3.
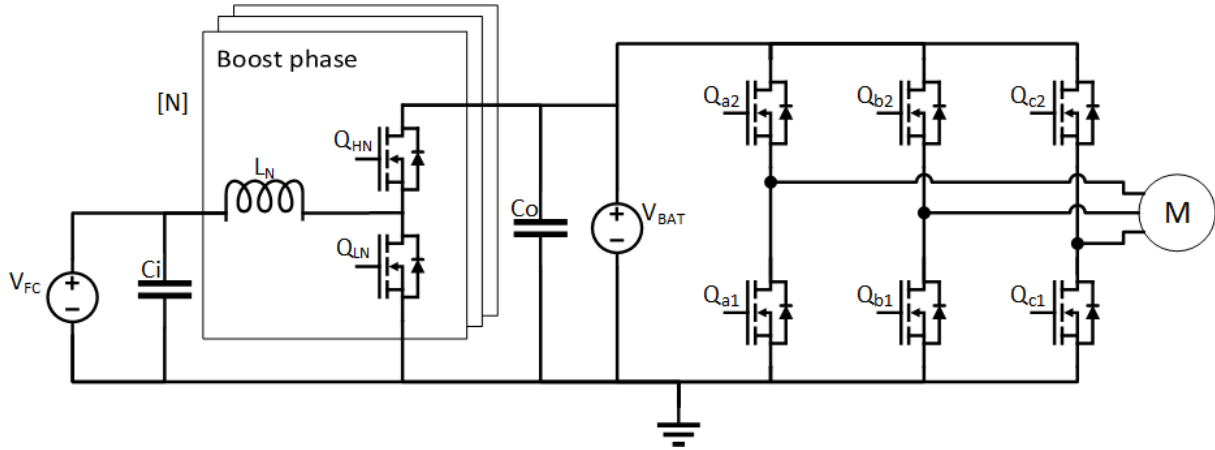

Figure 3.3: Interleaved boost converter with diagram

Number of phases and inductance

The peak to peak ripple in the current $I_{L,ripple}$ of each phase inductor with inductance L can be found by using Equation 3.7, which also depends on the switching period T_{sw} and input fuel cell voltage V_{FC}. The worst case scenario is found when the battery is fully charged and the fuel cell is exactly half the battery voltage, with a duty cycle D of 0.5. The peak current of the inductor $I_{L,max}$ is found by adding half the ripple to the expected fuel cell current $I_{FC,max}$ as seen in Equation 3.8.

$$I_{L,ripple} = \frac{DT_{sw}V_{FC}}{L} \tag{3.7}$$

$$I_{L,max} = \frac{I_{FC,max}}{N} + \frac{I_{L,ripple}}{2} = \frac{150}{N} + \frac{0.00104}{L} \tag{3.8}$$

The expected inductor mass can be found by combining the current rating, inductance and amount of phases N as seen in Equation 3.9. It turns out that this equation always has a minimum inductor mass of 2.5 kg, independent of the amount of phases. This minimum is found when the current ripple is equal to two times the maximum DC current per inductor. Although the minimum mass of the inductors does not decrease with the number of phases, the ripple current does significantly decrease when multiple phases are added, adding more and more phases yields diminishing returns and increases complexity however.

$$m_{L,total} = 4NLI_{L,max}^2 \tag{3.9}$$

Figure 3.4a shows the total inductor mass for a range of input current ripples and number of phases. The required inductor mass for reasonable input current ripples is much lower when multiple phases are used. The

target is set to reduce the input ripple current to 2 A_{pp} which results in the inductor mass shown in Figure 3.4b. For the optimal inductor mass, the system should be made with $\sqrt{150} \approx 12$ phases. A twelve phase interleaved inverter would be too complex however, and with an additional 1.5 kg, the same ripple current can be achieved with just 6 phases. The resulting 6 inductors have an inductance of $180\mu H$, with a current rating of 31 A.
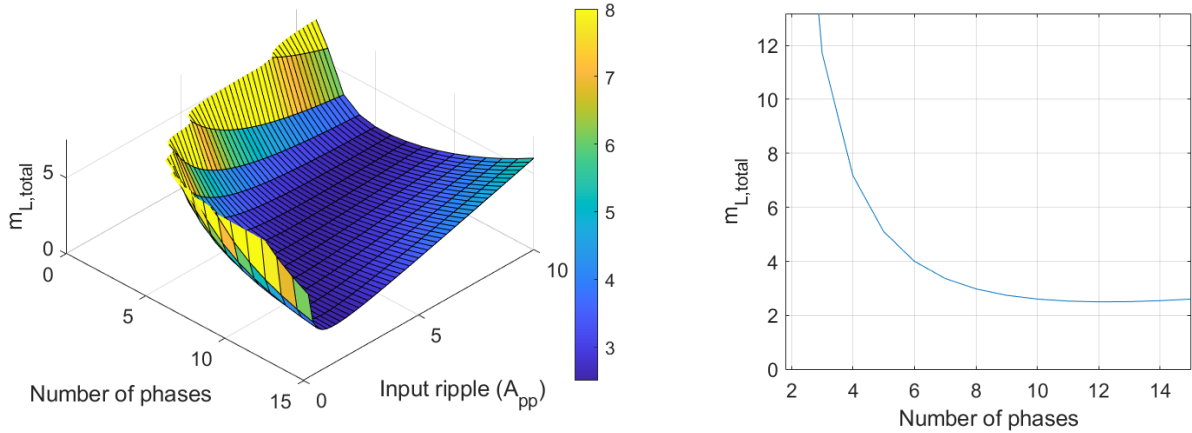

(a) Inductor mass for varying phases and input current ripple

(b) Inductor mass for varying phases at 2 A_{pp}

Figure 3.4: Resulting inductor mass under different design variables

3.3.2   PLECS model

The interleaved boost converter with inverter was implemented in PLECS and controlled based on the desired fuel cell current using a PI controller using the input current as a feedback signal. A single duty cycle D is then fed into six triangle wave based PWM generators that run 1/6th of the switching cycle out of phase from each other. Figure 3.5a shows the full converter, with the six phases and some additional components. Figure 3.5b shows the submodel of one of the six phases, consisting of the inductor, series resistance and the two switches.
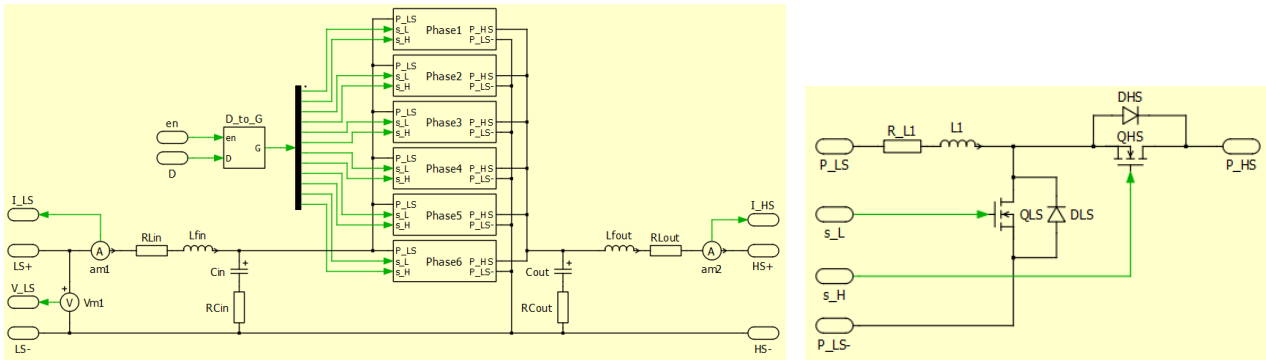
(a) Full converter

(b) Converter phase

Figure 3.5: PLECS model of the interleaved boost converter

3.3.3   Results

The PLECS model was tested on a sped-up load profile, and the results are shown in Figure 3.6. Figure 3.6a shows the propeller speed as well as the motor torque and its setpoint. The torque remains slightly below the setpoint due to the internal friction of the PMSM. Figure 3.6b shows the resulting power distribution between the motor, battery packs and fuel cell system, as well as the setpoint of the fuel cell system. These two figures show that the control of the two set points was achieved and that it is indeed possible to use this system to implement the hydrogen range extender. Figure 3.6c and Figure 3.6d show the voltage and current behavior of the fuel cell and battery systems respectively. The fuel cell system can be seen to take some time to settle to a new voltage after a change in the output power, corresponding to the polarization curve and output capacitance.
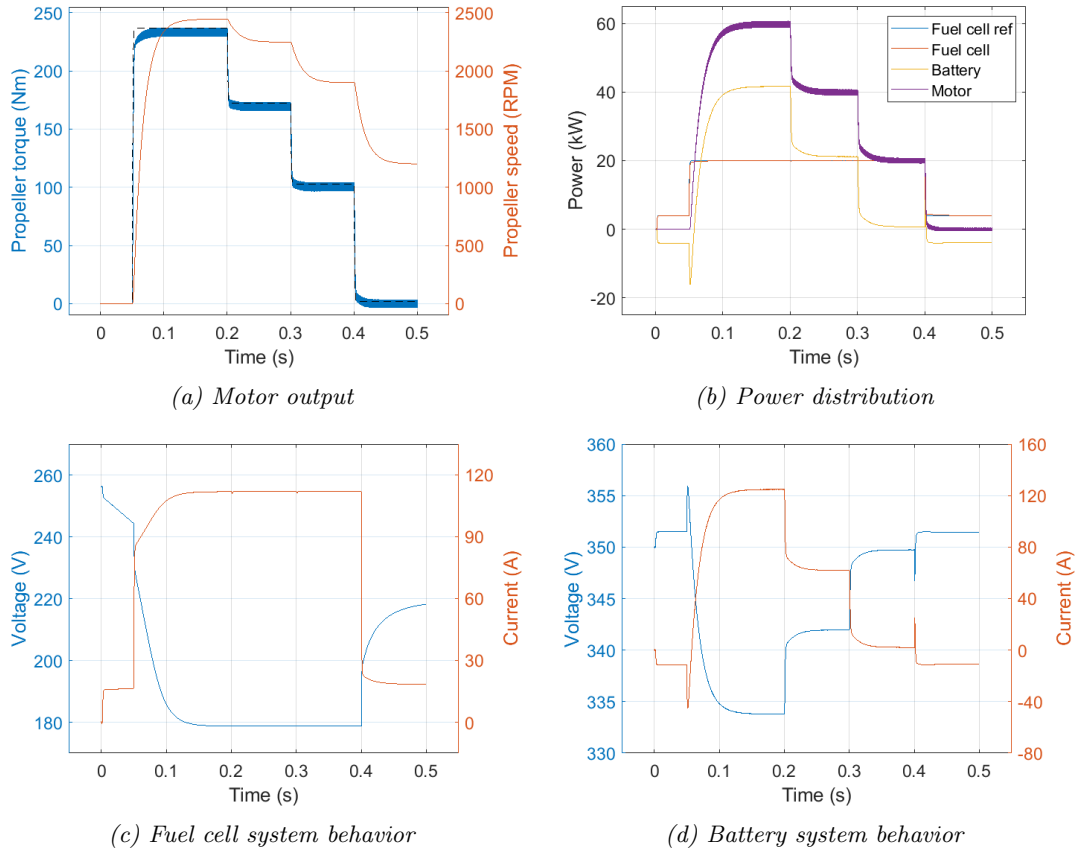
(a) Motor output

(b) Power distribution

(c) Fuel cell system behavior

(d) Battery system behavior

Figure 3.6: Dynamic behavior of interleaved boost converter with basic inverter

Interleaved current ripple

The unfiltered input and output current of the interleaved converter are shown in Figure 3.7 for the duration of one full switching period at an operating power of 20 kW. The input current is the addition of the six inductor currents, which is a continuous ripple at six times the fundamental switching frequency. The output current is the sum of a switching number of inductor currents, here it is switching between 3 and 4 inductors. With a duty cycle of 0.47 an average of $6 \times (1 - 0.47) = 3.176$ inductors connected to the output is also expected. As the switching between 3 and 4 inductors causes a larger ripple than the ripple in inductor current, increasing the phase inductance would do little to decrease the size of the output CL filter.
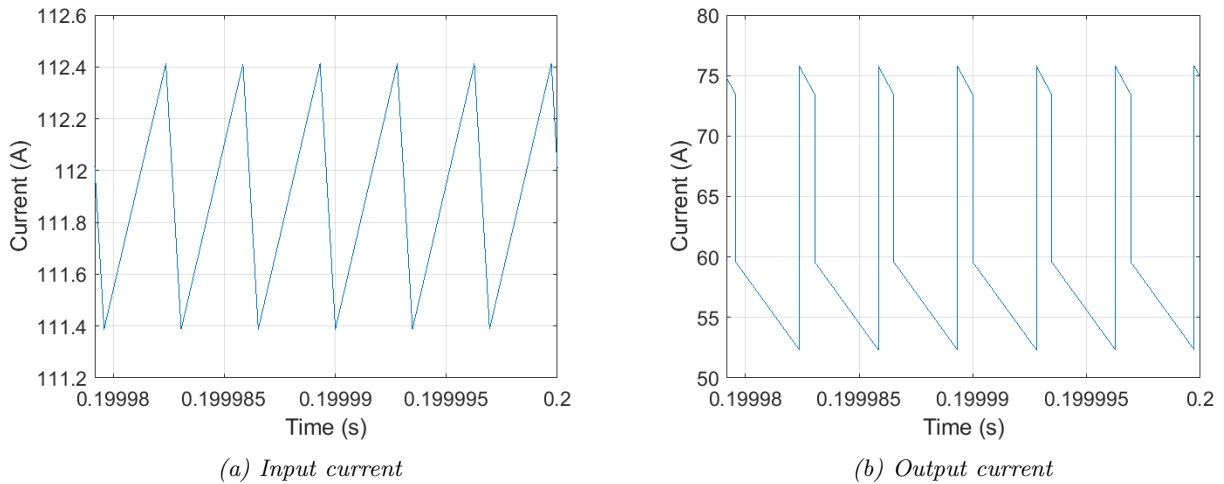

(a) Input current

(b) Output current

Figure 3.7: Current ripples of interleaved phases

Functionality

The addition of the fuel cell with interleaved boost converter successfully reduced the load on the battery packs. It was able to control the motor as well as the fuel cell power, with some settling time on both fuel cell power

27

and motor torque. One drawback became apparent in this system, as there is no communication between the motor controller and the fuel cell power controller, the fuel cell output power experienced a dip when the motor power was increased or decreased. This happens due to the changing output battery voltages, which requires the boost converter to change its duty cycle accordingly. A different or faster control algorithm may mitigate these effects, but they are inherent of this setup.

Switching losses

In this design, the switching losses can be found by considering the 12 switches in the interleaved boost converter as well as the 6 switches in the inverter. When the fuel cell output is set at 20 kW the switching losses in the boost converter add up to $12 \times 0.5 \times 335 \ V \times 17 \ A \times 48000 \ Hz \times 22 \ ns = 36 \ W$. At 60 kW the inverter has an average absolute current of $\frac{2}{\pi} \times 262 \ A$, resulting in an additional $6 \times 0.5 \times 335 \ V \times 166 \ A \times 48000 \ Hz \times 22 \ ns = 177W$. The total switching losses of this design are now estimated to be 213 W.

Passive component size

The inductors of the boost converter were selected with a weight of $4 \ kg$. In addition, the boost converter's input capacitor of 50 μF and the output capacitor of 210 μF amount to an expected mass of 0.3 kg. It turned out that the ripple requirements of the fuel cell and battery could not be met yet with this design and additional filters were added. Two additional 1 μH, 150 A inductors are added at the input and output of the boost converter, adding up to an additional 0.2 kg. The switching of the inverter also introduces large ripples in the battery currents. These ripples were mitigated with an LC filter, reducing the ripple to within the 0.2 A_{pp}. The inductor of 10 μH weighs around 1.6 kg due to the large current requirement when operating at 60 kW. One additional 1 mF capacitor adds another 1 kg. The total sum of the passive components now adds up to 7 kg.

Motor current

The motor current during the simulation is shown in Figure 3.8. To apply torque, a positive Iq is required and Id remains zero on average. The ripple in Id and Iq reaches a maximum at 60 kW motor power, with a ripple of 8.3 A_{pp} in Iq and 15.6 A_{pp} in Id. This ripple remains largely constant once the inverter is active.
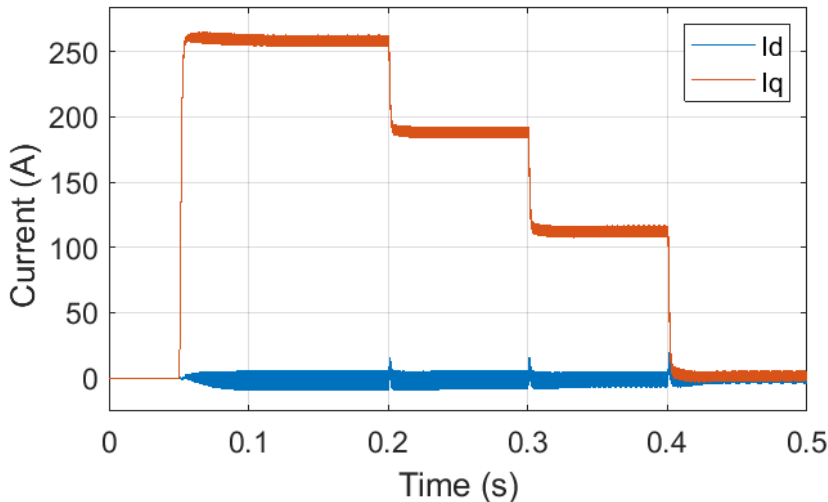

Figure 3.8: DQ motor current

3.4 Z-source inverter

The Z-source inverter is the first dual-DC-port inverter that is considered, what these systems have in common is that they start with the basic three phase legs of the basic inverter, to which some components are added to enable some form of power transfer between the two DC sources and the AC output. The Z-source inverter uses an impedance network at the DC-link side of the inverter, which enables the use of a shoot-through state, where the two switches of one or more inverter legs are both turned on. Normally this would cause a short circuit and damage the inverter, here the inductance's in the impedance network prevent an instantaneous increase in the current and but are charged instead. Figure 3.9 shows the architecture of interest. Although a Z-source inverter can also be used as a boosting DC/AC inverter for a single DC power source, here it is converted to

a dual-DC-port inverter by placing the battery system in parallel to one of the capacitors in the impedance circuit, following Hu et al. [42].
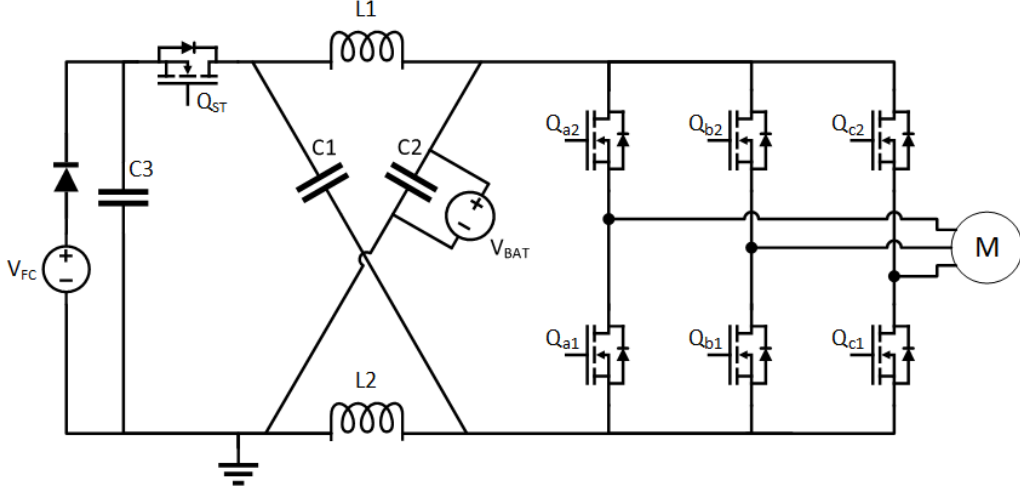

Figure 3.9: Z-source inverter diagram

3.4.1 Shoot-through behavior

When both switches of one of the inverter phase legs are turned on, the inverter is in shoot-through mode. At these moments, Q_{ST} is turned off, and inductor L_1 is placed in parallel with capacitor C_1 and L_2 is placed in parallel to C_2, charging the inductors. When there is no shoot-through, a voltage path can be drawn from the negative terminal of the inverter to the positive terminal through C_1, C_3 in reverse and C_2, the resulting DC-link voltage is $V_{C1} + V_{C2} - V_{C3}$. In a quasi steady state, capacitor C_3 will follow V_{FC} and capacitors C_1 and C_2 will follow V_{BAT}. The DC-link voltage experienced by the inverter is the sum of these individual voltages as shown in Equation 3.10.

$$V_{o,eff} = 2V_{BAT} - V_{FC} \tag{3.10}$$

In the non shoot-through state, inductor L_1 is discharged into C_2 through C_3 and inductor L_2 is discharged into C_1 through C_3. The system can be analysed by looking at the average voltage over the inductors over one switching period T_{SW}. To have a volt-second balance and a constant inductor current between the beginning and end of a switching cycle, the equation in Equation 3.11 should be equal to zero.

$$\frac{L\Delta I_L}{T_{sw}} = D_{ST}V_{BAT} + (1 - D_{ST})(V_{FC} - V_{BAT}) \tag{3.11}$$

The resulting shoot-through duty cycle D_{ST} can now be described as in Equation 3.12. When a slightly larger duty cycle is used, the inductors current will start to increase over time. This allows a feedback controller to control the fuel cell output power. The control algorithm now requires three sensors, that of the fuel cell current as well as the fuel cell and battery voltage. The fuel cell voltage also being used to convert the reference power into a reference current.

$$D_{ST} = \frac{\frac{V_{BAT}}{V_{FC}} - 1}{2\frac{V_{BAT}}{V_{FC}} - 1} \tag{3.12}$$

Voltage modulation limit

A normal inverter using space vector modulation has a maximum output voltage amplitude of $\frac{V_{DC}}{\sqrt{3}}$. For the original inverter, this amounts to about 200 Vp at a battery voltage of 350 V. With this Z-source inverter, the maximum modulation depends on the effective DC-link voltage, as well as the duty cycle required for the shoot-through times. It turns out that when Equation 3.10 is combined with Equation 3.12, the increase by the higher effective output voltage cancels out with the decrease by shoot-through time, resulting in the same output voltage range as before.

$$V_{ac,peak} = \frac{V_{o,eff}}{\sqrt{3}}(1 - D_{ST}) = \frac{V_{BAT}}{\sqrt{3}} \tag{3.13}$$

Unidirectional power transfer

When a fuel cell is used as the lower voltage source, it is important that no current flows back into the fuel cell. It is possible to use a diode instead of Q_{ST} to enforce this, however, it would also cause the inductors to go into a discontinuous current regime for certain operating points. This also sets a minimum power on the fuel cell, which is not desirable. The use of Q_{ST} does allow the inductor current ripple to be negative. As long as the average current is positive, the fuel cell will provide the desired output power. To prevent accidental power transfer into the fuel cell system during start-up for example, an additional diode is added in series with the fuel cell as can be seen in Figure 3.9.

Modified space vector modulation

The inverter was originally controlled using the PLECS space vector modulation block. To get the Z-source working, some additions had to be made to this block that enabled shoot-through states. The shoot-through time is subtracted from the zero vector duty cycle, as a shoot-through is effectively also a zero vector from the machine's perspective. The shoot-through is realized by adding 1/6th of the shoot-through time during each transition between output vectors. During each such transition one switch turns on and the other switch in that phase turns off. By making these events happen out of order and first turning the new switch on, wait the required shoot-through time and then turn the other switch off, the shoot-through is realized without any additional switching losses. The block also gets an additional output that switches the new transistor Q_{ST} on when there is no shoot-through and turn it off when there is a shoot-through. Figure 3.10 shows the switching states of the inverter for two switching cycles, the shoot-through states can be observed when the positive and negative gate signals overlap.
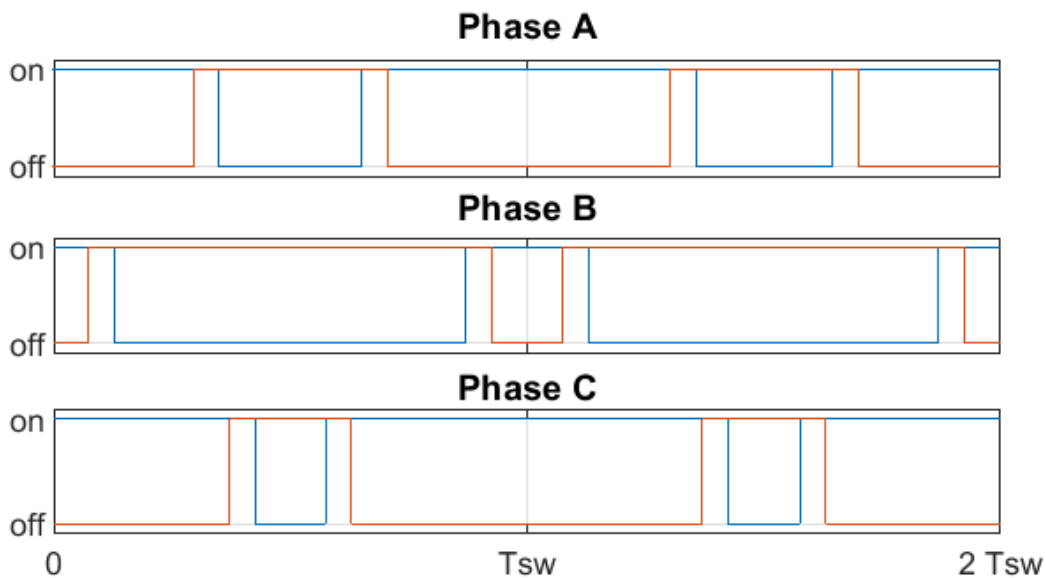

Figure 3.10: Inverter gate signals with shoot-through states

3.4.2 PLECS model

The Z-source inverter was also implemented and tested using the PLECS Blockset in Simulink. Figure 3.11 shows the two main parts of interest in this design as implemented in PLECS. Figure 3.11a shows the implemented impedance network, here it is unfolded with different ports of different systems on opposite sides. Figure 3.11b shows the final filter as used between the fuel cell and the impedance network. The third order CLC filter was required to remove the large steps in the current going into the impedance network and to reduce the current ripple below 0.2 App. Not shown here is an additional filter step in line with the battery packs based on a single inductor to move the current ripples to the capacitor in parallel with the battery packs. The final impedance network was created using two 80 μH inductors and two 1 mF capacitors. This setting allowed for stable operation at the lowest component size.
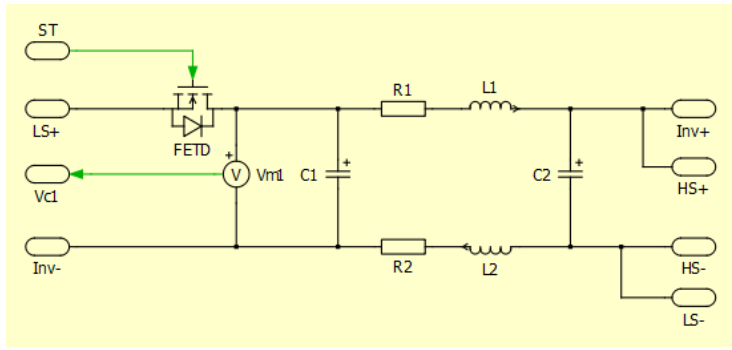
(a) Impedance network
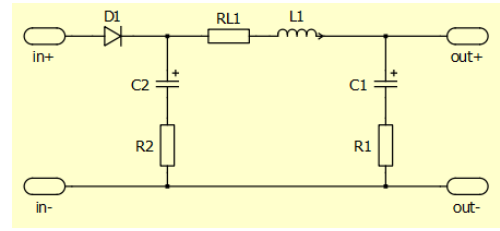
(b) Fuel cell output filter

Figure 3.11: PLECS models of the Z-source inverter

3.4.3 Results

The model was initially tested of the same load profile as the previous test on the interleaved converter with inverter. It turned out however, that sharp transitions in the set points caused some resonance within the impedance network this would damp out over time but made it more difficult to control the system. By applying a low-pass filter on the reference signals, the high frequency components that caused the resonance could be filtered out beforehand, resulting in a better system behavior. Figure B.1 in appendix B shows the data from the final simulation on this design, showing largely similar results as seen in Figure 3.6, but slightly smoothed out.

Low frequency current ripple

During the simulations, a significant low frequency ripple was detected in the fuel cell current, as can be seen in Figure 3.12. This ripple had a frequency equal to three times the inverter current frequency, and seemed to be in phase with peaks in the phase currents. The capacitance of C_2 in the fuel cell filter of Figure 3.11b mainly impacted the size of the current ripple, reducing it sufficiently at $1\ mF$. The likely cause of these ripples are conductive losses in the inverter that cause a sinusoidal voltage drop that reflect back to the fuel cell control.
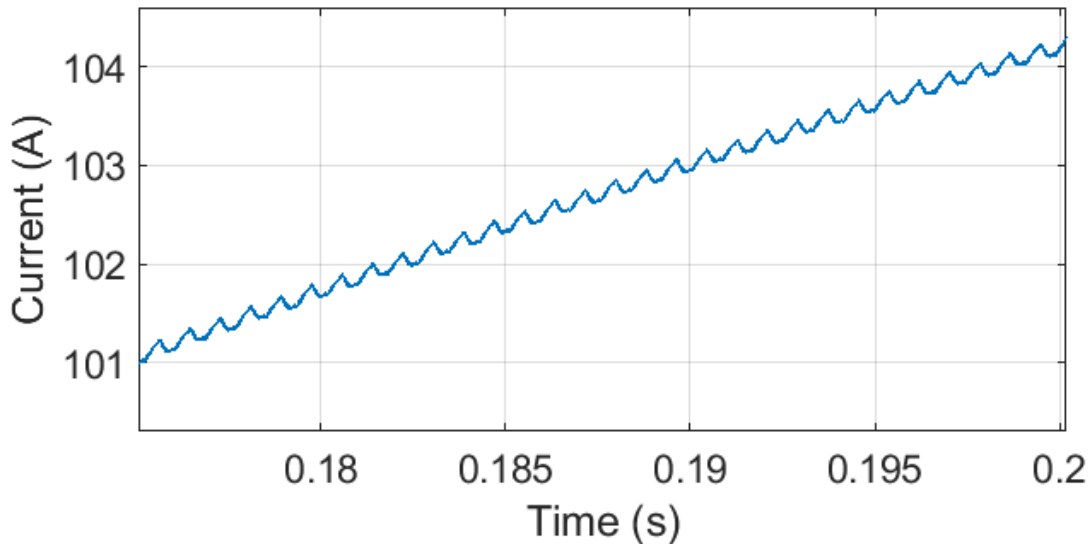

Figure 3.12: Fuel cell ripple current

Functionality

As mentioned before, the bandwidth of the controllers and reference signals had to be reduced to maintain a stable operation of the system. This should not pose a big problem however, as a delay of a few milliseconds in the response of the motor should not be noticeable for the pilot. In addition, this design suffers from a similar problem as the interleaved converter with inverter design, having noticeable hick-ups in the fuel cell output power during a transient in the motor power. This too can be explained by the limited response time of the

control loop, which can't be made more aggressive without making the system unstable. Other than that, the system is able to perform well in the required operating conditions.

Switching losses

In this design, there are fewer switches than in the interleaved converter design, but the switches in the inverter have a larger blocking voltage. The single switch Q_{ST} also has to turn on 6 times per cycle for shorter intervals. The current through Q_{ST} is zero in shoot-through states but depends on the inverter current in non shoot-through states. The current in these non shoot-through states was measured to be 186.6 A on average. The blocking voltage is equal to the effective output voltage described in Equation 3.10, which is about 475 V at peak power. This results in a switching loss of 280.8 W. These high losses can be mitigated significantly by only having two shoot-through events instead of six. These two moments would be when switching between two active vectors, where the current is low. This would reduce the switching losses of this switch to about 60 W. This does generate a much larger current ripple in the fuel cell current, where the low frequency component becomes three times as large, which would require a significant increase in passive component size.
The inverter switches always switch on and off with a shoot-through event, the current at these times is similar to the average current through Q_{ST} and, for six switches, this adds another 286 W of power, resulting in a total of 567 W in switching losses.

Passive component size

The main drawback of this design is the presence of the large passive components. The average current through inductor L_1 is equal to the fuel cell current, the average current through inductor L_2 however, is equal to the sum of the fuel cell and battery current. In normal operation this could go up to 252 A, when some headroom is added, the resulting 300 A, 80 μH inductor will have a mass of around 29 kg. The other inductor adds another 7.2 kg and the residual passive components add up to another 1.1 kg in inductors and 3.1 kg in capacitors. This all adds up to 40 kg in passive components.

Motor current

The motor current during this simulation is shown in Figure 3.13. The less aggressive motor current control is reflected in the bumps in Id. The ripple in Id and Iq is similar to that in the interleaved DC/DC with inverter design. The maximum ripple was also seen at 60 kW motor power with a ripple of 14.4 A_{pp} in Iq and 14.7 A_{pp} in Id.
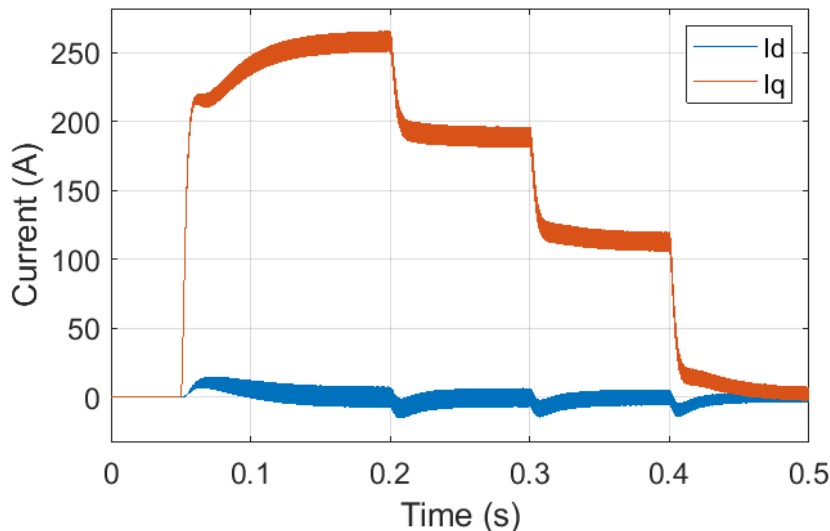

Figure 3.13: DQ motor current

3.5 Integrated dual-source inverters

A second type of dual-DC-port inverter is the integrated dual-source inverter. Multiple variations exist, all of which connect the second dc port at the center of the inverters phase legs. There are multiple variations on this concept, each with a different set of components that interface the second dc port with the phase legs.

Figure 3.14 shows the general design of such an inverter, where a common element and separate phase elements can be filled in depending on the design.
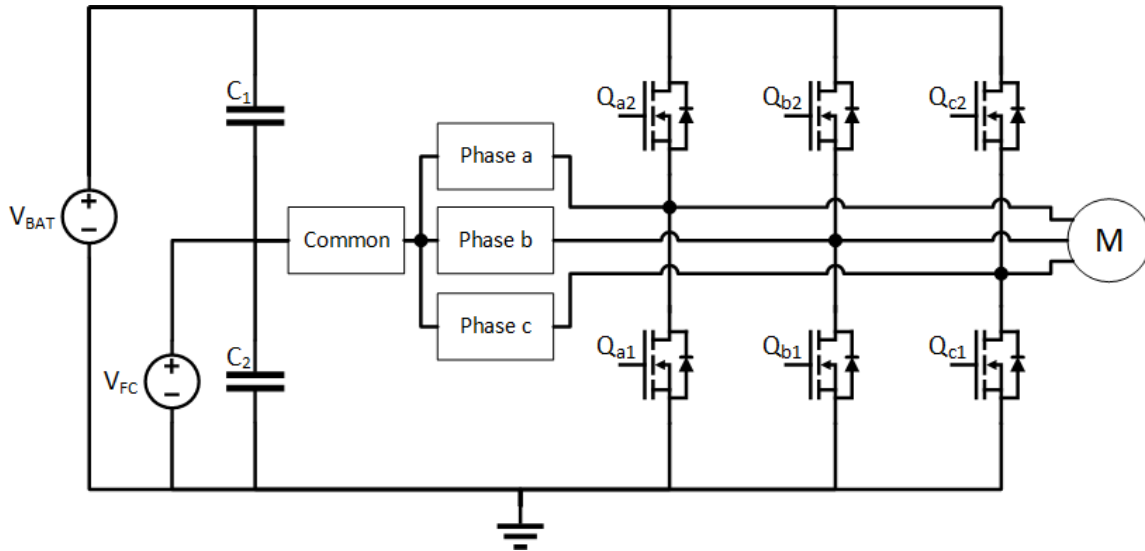

Figure 3.14: General integrated dual source inverter diagram

3.5.1   Interfaces

Three different types of integrated dual-source inverters are considered for this application and are shown in Figure 3.15. The first shown in Figure 3.15a is the split-source inverter that uses a single inductor with three diodes to boost the fuel cell power through the switching of the inverter [43]. This design is originally used with a capacitor at the battery voltage, the voltage of which would vary depending on the inverter AC output. Whether it also work when used with a fixed battery voltage needs to be investigated. The second design shown is a modified split-source inverter [44]. Here, the phases contain the inductors, which separates the DC current over three separate paths and could decrease the inductor size. A diode is added in the common path, to ensure uni-directional power for the fuel cell system. The third design is a multi-source inverter [45]. This design does not use passive elements in the interface, but effectively uses the machines phase inductances to enable power transfer between the three ports. The resulting topology is very similar to that of a T-type three-level inverter, with the difference in that it is used with asymmetric DC voltages.

(a) Split-source inverter   (b) Modified split-source inverter   (c) Multi-source inverter

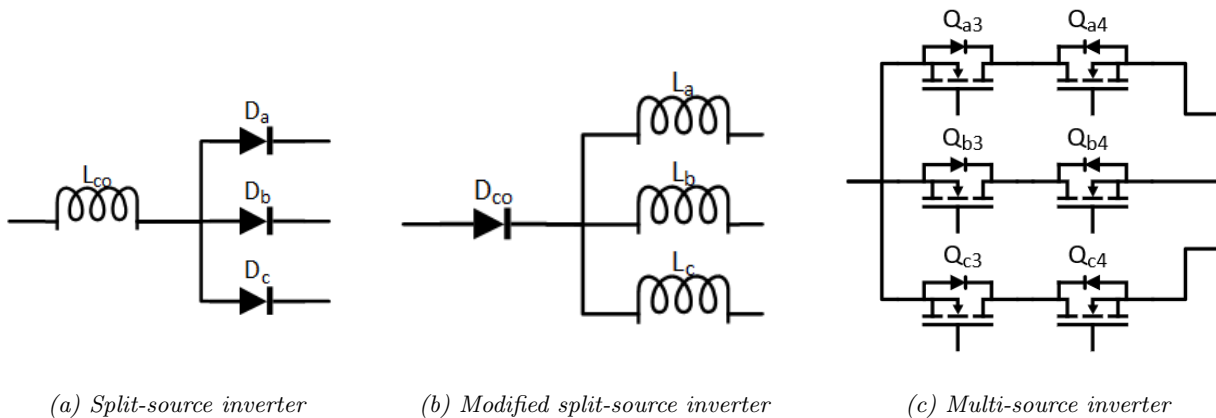*Figure 3.15: Considered interfaces for the integrated dual-source inverter*

3.6   Split-source inverter

The split-source inverter uses an inductor and three diodes to boost the voltage of one DC source to the inverter DC link voltage. The resulting diagram is shown in Figure 3.16. This inverter can distribute power as each of the three phases now behaves like a boost converter leg with a shared inductor.
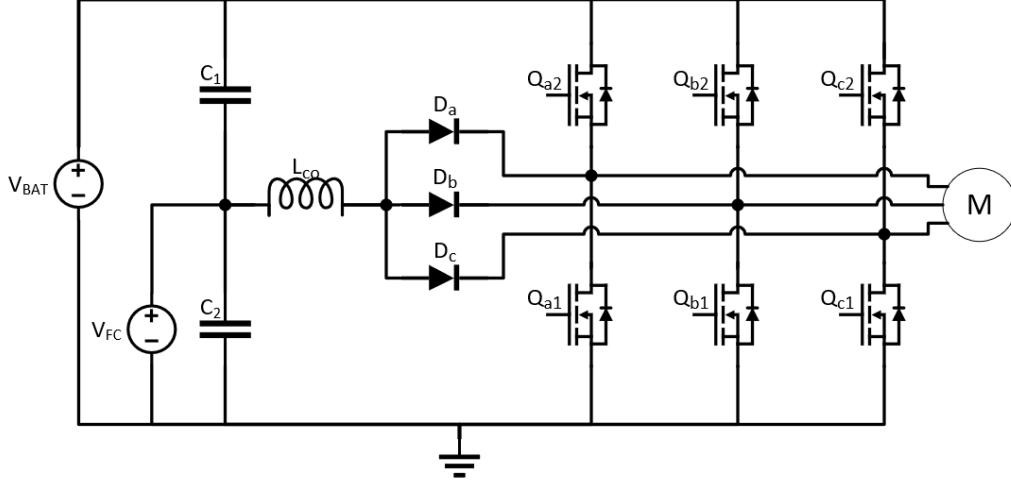
Figure 3.16: Split-source inverter diagram

Boosting duty cycle

When one of the three phases is low, the inductor is charged through the corresponding diode. Only when none of the three phases are low, the inductor is discharged. By calculating the volt-second balance required to keep the inductor current constant, the relation shown in Equation 3.14 can be found describing the required duty cycle in which the inductor is charged. This equation follows that of a normal boost converter [43].

$$D = 1 - \frac{V_{FC}}{V_{BAT}} \tag{3.14}$$

Modified space vector modulation

A modified space vector modulation algorithm is used to enforce this duty cycle on the inverter output. This is done by redistributing the zero vector time, which is normally divided equally between the $(1,1,1)$ and $(0,0,0)$ vectors. The time allotted to the $(1,1,1)$ vector is made equal to the desired duty cycle times the entire switching period T_s. Table 3.2 shows the resulting time for each vector, where U_a and U_b are the two active vectors, $U_{0,h}$ the all high zero vector and $U_{0,l}$ the all low zero vector.

Table 3.2: Vector timing for modified space vector modulation

Vector	$U_{0,h}$	U_b	U_a	$U_{0,l}$	U_a	U_b	$U_{0,h}$
States	$(1,1,1)$	1 low 2 high	2 low 1 high	$(0,0,0)$	2 low 1 high	1 low 2 high	$(1,1,1)$
Length	$\frac{(1-D)T_s}{2}$	$\frac{1}{2}T_b$	$\frac{1}{2}T_a$	$DT_s - T_a - T_b$	$\frac{1}{2}T_a$	$\frac{1}{2}T_b$	$\frac{(1-D)T_s}{2}$

Voltage modulation limit

The length of $U_{0,h}$ is limited by the available zero vector time, which in turn, depends on the AC voltage on the output. This results in the constraint seen in Equation 3.15. This relation shows that the available AC voltage can be increased by increasing the battery voltage or decreasing the fuel cell voltage.

$$D \geq |V_{\alpha\beta}| \frac{\sqrt{3}}{V_{BAT}} \tag{3.15}$$

The maximum voltage vector magnitude seen in the simulations is 165.7 V, which occurs during the takeoff scenario, at maximum torque and RPM. Figure 3.17 shows the available AC voltage magnitude, with the 165.7 V_p requirement. This requirement can not be met initially but the required AC voltage can be decreased by introducing a field weakening current which is further described in subsection 4.2.1. With a field weakening current of $I_d = -200$ A the maximum AC voltage is reduced to 132.3 V_p which is also shown in the figure. This field weakening current increases the current magnitude by 26% which will come with additional losses and cooling requirements. Even at this reduced voltage, the requirement can only be met when the fuel cell is at a low voltage and the duty cycle is high. For this reason, the design is tested with a modified fuel cell stack, with a reduced cell count of 211, instead of 264. The polarization curve is also updated accordingly. Even with the reduced fuel cell voltage, the open circuit battery voltage needs to be 375 V or higher, which is only the case for a state of charge of 75% or higher.
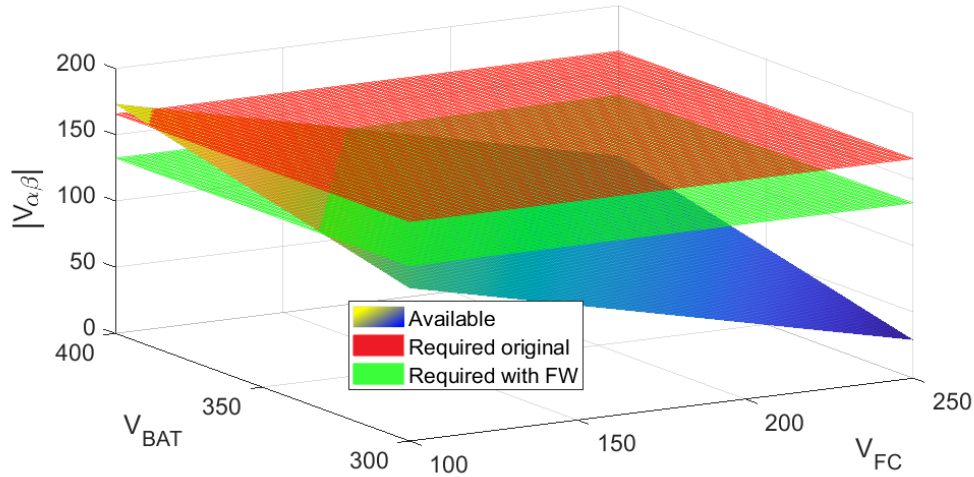
Figure 3.17: Available output voltage for different fuel cell and battery voltages

3.6.1 PLECS model

The split-source inverter was modelled in PLECS and Figure 3.18 shows the most interesting parts of the model. Figure 3.18a shows the two CLC filter used for filtering the switching noise out of the fuel cell and battery ports. Figure 3.18b shows the interface between the fuel cell port and the motor phases. The diodes forward voltage and series resistance were modelled after two parallel PCFF75H120SWF diodes from Onsemi [46]. The inductor size is mainly influenced by the current ripple that should be significantly smaller than the fuel cell idle power current, which allows the converter to always operate in continuous conduction. Here, a value of 80 μH was selected.
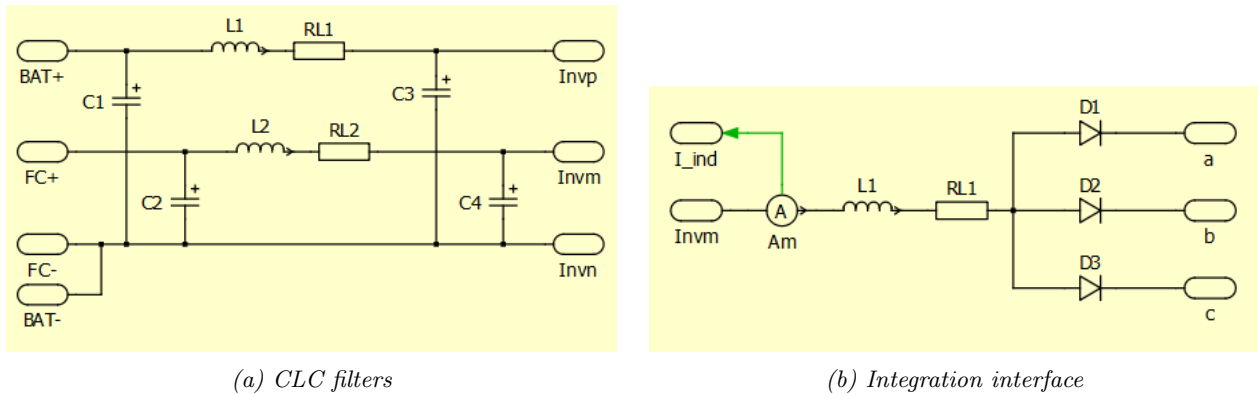

(a) CLC filters

(b) Integration interface

Figure 3.18: PLECS models of the Z-source inverter

3.6.2 Results

The model was tested with the same load profile as the other scenarios and the results are shown in Figure B.2 in appendix B. Due to the adjustment to the number of fuel cells, the fuel cell system had a lower output voltage and higher current than the other designs which can be seen in Figure B.2c.

Functionality

The reduced voltage operating range is a large downside of this design, effectively reducing the energy storage capacity of the battery packs by 75%. At the same time, the smaller fuel cell produces the same output power at a lower efficiency, 50.8% instead of the original 54.8%. The fuel cell control is better than the previous designs and does not show any ripples in the fuel cell power during motor load transients, which appears to be inherent to the modified space vector algorithm.

Switching losses

The switching losses in this design should be very similar to those in the original inverter as there are no additional switching elements and the designs operate at the same frequency. The on average higher battery

voltage and significant field weakening current result in a switching loss of 242.5 W for this design. It is expected that parasitic effects of the diodes at the interface will introduce additional losses during a switching event but these are not calculated here.

Motor current

The motor current during the simulation is shown in Figure 3.19. The Iq curve is very similar to the previous simulations, but the Id curve is now non-zero due to the large amount of field weakening. The ripple in Id and Iq reaches a maximum at 60 kW motor power, with a ripple of 14.8 A_{pp} in Iq and 13.6 A_{pp} in Id.
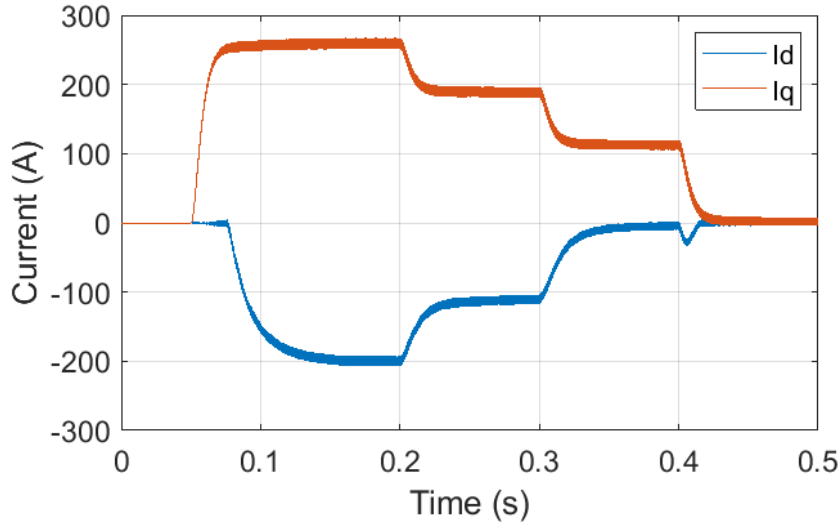

Figure 3.19: DQ motor current

Passive component size

The main fuel cell inductor has the largest contribution to the passive component mass in this design. The size of this component is further increased by the higher current rating due to the lower fuel cell voltage. The resulting mass is 10.4 kg. The two CLC filters add to this with 1.2 kg in inductors and 2.3 kg in capacitors. The total mass now adds up to 13.9 kg.

3.7   Modified split-source inverter

The modified split-source inverter uses one inductor per phase, the AC current of which cancels out at the DC port as the phases are 120° apart. A DC current can be generated that is common between the phases and adds up instead. This design quickly showed a large flaw when used to control a machine. When used as a grid inverter, the AC current in the inductors has a manageable magnitude. When the system is used with a machine at very low speeds, like during startup, the inductor impedance approaches zero and the current rapidly increases until eventually something will break. This means that this design was not suitable for this application.

3.8   Multi-source inverter

The multi-source inverter connects a second DC voltage source to the inverter phases using two switches to block the current in both directions, resulting in a T-type three level inverter topology. This design is shown in Figure 3.20. The negative voltage of the secondary source is connected to the negative of the main inverter DC-link. The positive voltage of the second DC link is connected to the bidirectional blocking switches and should always be smaller than the main DC-link to prevent the top switches from conducting when the secondary source is active. Here, the main DC-link is implemented by the battery and the secondary is the fuel cell voltage.
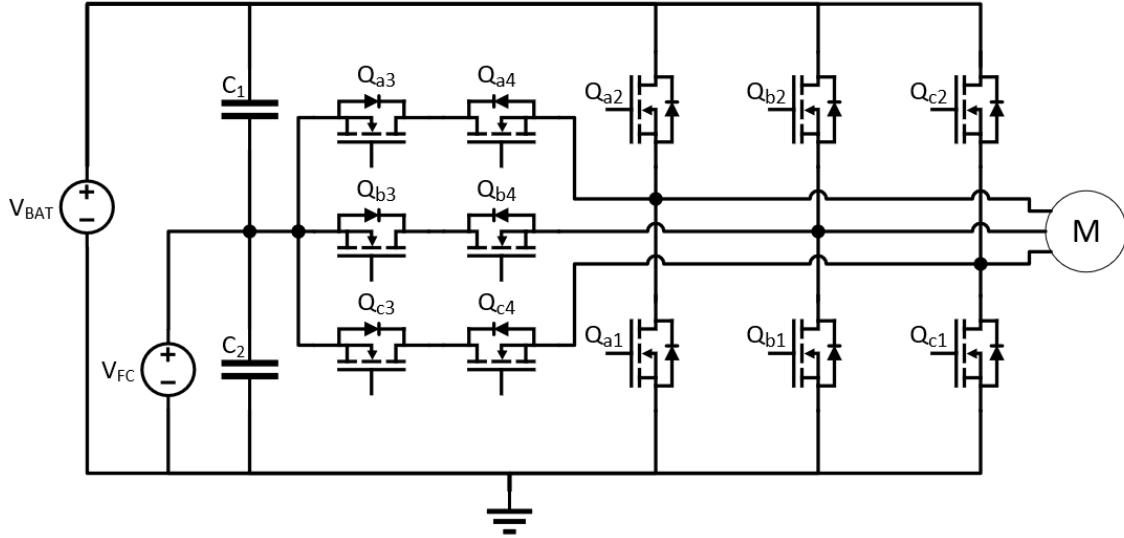
*Figure 3.20: Multi-source inverter diagram*

3.8.1 Modulation algorithm

To enable bi-directional power transfer to the batteries, as well as direct control of the fuel cell power, a multi-objective vector modulation algorithm was developed. This algorithm is further explained in chapter 4. The results of simulations on the final system are shown here. To match the other designs, the control frequency is set at 24 kHz, which results in switching frequency of 48 kHz.

3.8.2 PLECS model

Two PLECS models of interest were required to implement the multi-source inverter as seen in Figure 3.21. The interface to the inverter legs was implemented as seen in Figure 3.21b. The two DC ports were filtered using an CLC filter as seen in Figure 3.21a. The output of these filters are used as the DC link voltages.
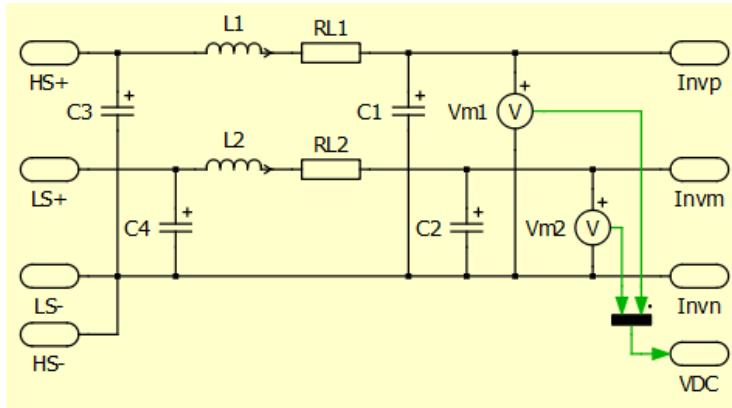
(a) CLC filters
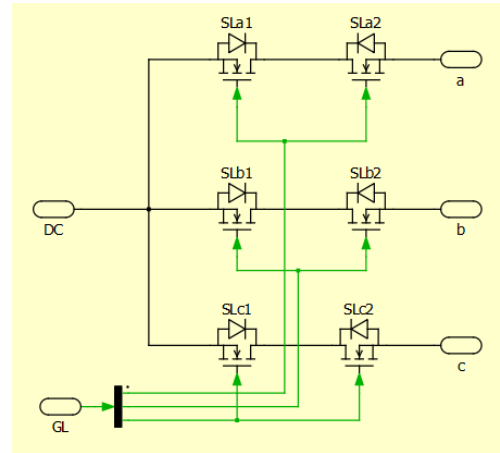
(b) Integration interface

Figure 3.21: PLECS models of the Z-source inverter

3.8.3 Results

This final model was also tested with the flight load profile and the main results are shown in Figure B.3 in appendix B. No large differences are observed compared to those of the interleaved and Z-source simulations and the test was successful.

Port power accuracy

The port power control of the multi-objective modulation algorithm can be observed in Figure 3.22 for part of the experiment. The modulation algorithm used the voltage closest to the interface or the link voltages as

measured at the end of the CLC filter shown in Figure 3.21a. With changes in the fuel cell power, the output voltage gradually changes. This change in output voltage also requires some energy to be stored or released from the filter capacitors, this causes the gap between the port power and the fuel cell power. Once the voltage has settled the filter inductor series resistance creates an additional error of 22 W, which can all be seen in Figure 3.22. During transients in the motor velocity and power, the DQ0 current measurement is delayed, causing the dips in the output power. Finally, some steady state error exists in the port power. In total, the port power stays within 0.2% of the target. In a real system, errors and delays within the multiple sensors required to operate the system could add up and result in a significant steady state error.
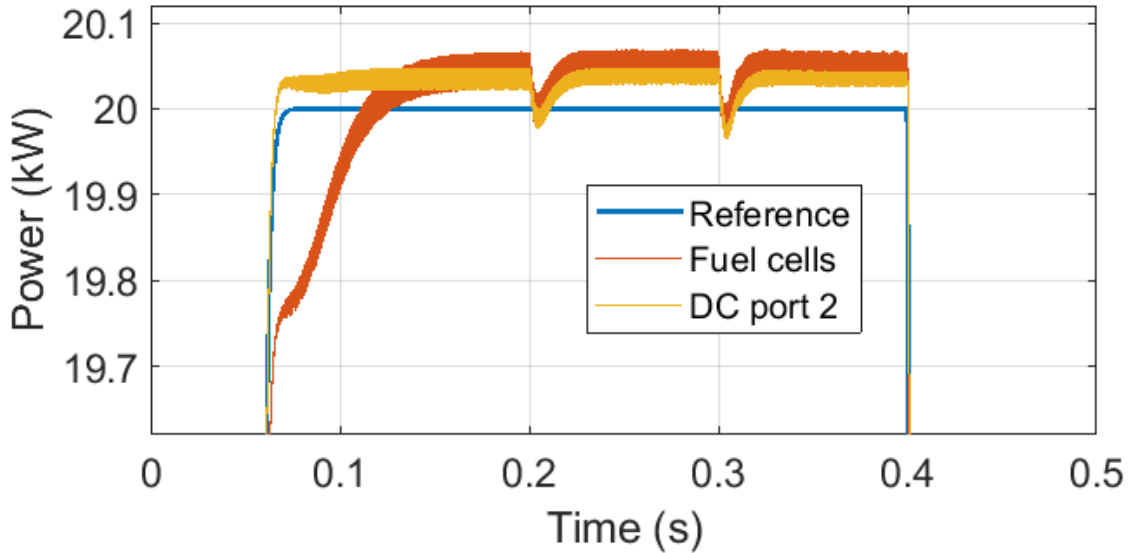

Figure 3.22: Accuracy of the fuel cell output power

Functionality

The torque and power references were filtered like with the Z-source inverter to reduce the impact of transients on the control algorithm. This filter was much less intense than with the Z-source however, and there is barely any noticeable difference with the interleaved inverter. The control algorithm proved to work as expected but had some error as discussed. With the selected fuel cell system and battery voltage, the design was able to generate the desired output voltages while maintaining the set fuel cell power. If the fuel cell or battery voltage had been lower, the amount of required field weakening current would have been higher, eventually going beyond what would have been reasonable. This means that the design may not be suitable for all other applications.

Switching losses

The six standard inverter switches were measured to have a total loss of 159 W during the takeoff scenario, operating in similar conditions as the standard inverter test. One important difference is the modified switching algorithm that can clamp one of the phases to ground for up to a third of an output voltage period. During this clamping, no switching losses are present, reducing the average switching losses. The three pairs of bidirectional blocking switches add an additional 53 W in losses, resulting in a total of 212 W.

Passive component size

The only passive components present in this design are in the two CLC filters for the DC ports. Two 210 μF and two 1 mF capacitors add up to 2.4 kg and two 10 μH inductors add up to 1.8 kg. The total passive component mass is now 4.2 kg.

Motor current

The motor current during the simulation is shown in Figure 3.23. The Iq curve is again similar to the previous simulations and Id changes depending on the required field weakening. An advantage with this design is that the required field weakening goes down with both fuel cell and battery voltage. In addition, the required field weakening current is lower when there is already a large Iq present in the motor, causing the field weakening to peak when Iq is lower and the cooling system has some capacity leftover. The ripple in Iq is 16.1 A_{pp} at 60 kW motor power, but at the descent stage with no motor output power the ripple is slightly larger at 16.5 A_{pp}.

The power sharing between the DC sources through the motor inductance is reflected in the larger Id ripple. During the idle power transfer before takeoff, where the motor is not rotating the ripple in Id is 37.7 A_{pp} and during the descent stage when the motor output power is zero the ripple in Id is 31.5 A_{pp}. In the other parts of the load profile the ripple is also larger than in the other designs, around 19 A_{pp} on average.
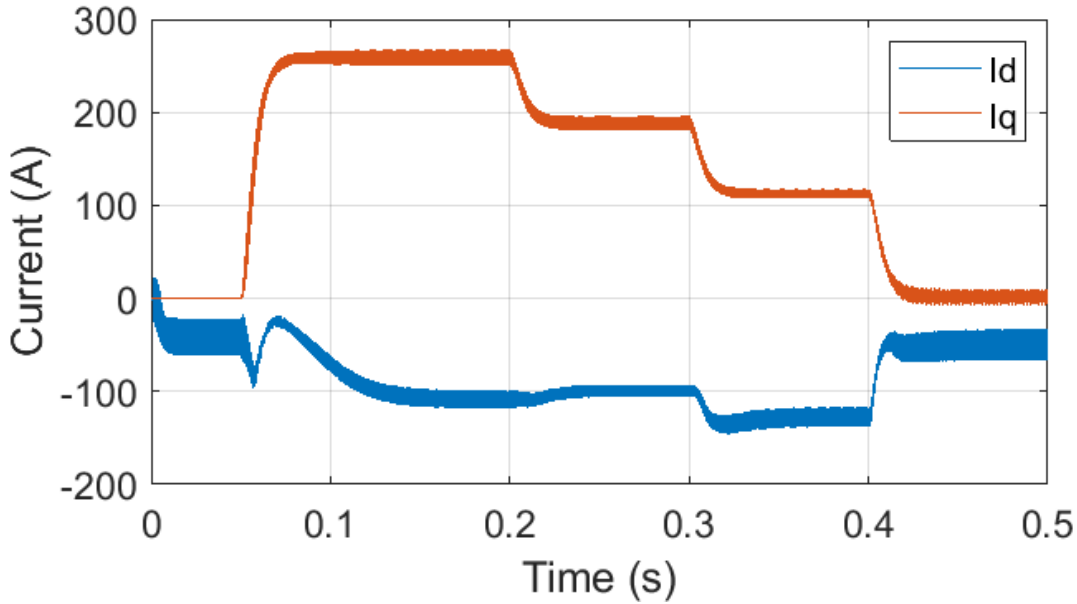

Figure 3.23: DQ motor current

3.9 Comparison of architectures

With the simulations on the different designs, a comparison can be made to find which design is suited for the fuel cell range extender application. This comparison is based on the original characteristics described in section 3.1 as well as some additional observations from the simulations.

3.9.1 Functionality

The modified split-source inverter was not able to function in the desired operating conditions and is not suited for this application. The four other designs were able to function correctly in the desired operating conditions are further considered.

Transient response

The interleaved, Z-source and multi-source designs all suffered from bumps in the fuel cell power at transients in the motor power. Only the split-source did not show significant effects at the times. The simulations were run on a sped-up load profile, which significantly increases the effects of these transients. When the propeller inertia and fuel cell double layer capacitance are returned to their original values and the load profile is executed at its original speed, the controllers should suffer less from delays in sensor data and be able to better control the fuel cell power.

Output voltage range

The inverter output voltage was sometimes limited by the adjustments in how the inverter operates in different designs. When the output voltage range was too low, a field weakening current was sometimes introduced. The standard maximum output voltage was 165.7 V_p. The basic inverter in the interleaved boost design was able to provide the output voltage at all times with a limit of $\frac{V_{BAT}}{\sqrt{3}} = 196 \ V_p$, just like the Z-source inverter. The split-source inverter had a significantly reduced output voltage range, being able to provide $\frac{V_{BAT} - V_{FC}}{\sqrt{3}} = 135 \ V_p$ with a reduced fuel cell voltage, high battery state of charge and a field weakening current of $-200 \ A_p$. Finally, the multi-source inverter has a more complicated voltage limit, but with a field weakening current of $-108 \ A_p$ it was able to create an output voltage of 147.5 V_p with the original fuel cell and battery settings.

3.9.2 Switching losses

The switching losses are quite similar between designs as the six main inverter switches turn on and off once at 48 kHz for each design. Some designs introduce additional switching elements or increase the current going through these switches that increase the losses. The results are summarized in Table 3.3 and the main outlier is the Z-source inverter. The single shoot-through switch turns off and on during each of the six shoot-through states which effectively doubles the total switching losses.

Table 3.3: Switching losses in different designs

Architecture	Interleaved + inverter	Z-source inverter	Split-source inverter	Multi-source inverter
Power (W)	213	567	243	212

3.9.3 Passive component size

The different designs varied greatly in the required passive component size. The main contribution comes from large inductors in the path of the fuel cell power. The inductor of the interleaved boost converter was reduced significantly due to the interleaving, something that was not an option for the Z-source and split-source inverters. Table 3.4 shows the passive component mass of the different designs. The multi-source inverter scored best here, as it only required two CLC filters which are also found in other designs.

Table 3.4: Passive component mass in different designs

Architecture	Interleaved + inverter	Z-source inverter	Split-source inverter	Multi-source inverter
Mass (kg)	7.0	40	13.9	4.2

3.9.4 Motor current

The motor current was influenced by the different architectures and corresponding control algorithms and can be compared by looking at the maximum phase current seen in a simulation as well as the high frequency ripple in this current.

Current magnitude

The maximum motor current largely influences the required cooling of the motor and can increase the motor size. Table 3.5 shows the maximum current found in different designs. The interleaved and Z-source have the same original current without field weakening, the split-source has an increase of 26% and the multi-source has an increase of 8.3%.

Table 3.5: Maximum motor current in different designs

Architecture	Interleaved + inverter	Z-source inverter	Split-source inverter	Multi-source inverter
$|I_{dq}|$	259.1	259.1	327.3	280.7

Current ripple

The current ripple can introduce noise and vibrations in the motor and introduce undesirable consequences for the motor. Table 3.6 shows the ripple in direct and quadrature components of the motor current for the different designs. Each dual-DC-port inverter has a larger ripple in the Iq current but the Z-source and split-source have a slightly improved ripple in Id compared to the standard inverter. The multi-source inverter shows the worst ripple overall. This was expected as the multi-objective control algorithm actively uses the motor inductance to store energy for the power transfer between the two DC ports whereas the other dual-DC port inverters use their own large inductors to boost the fuel cell voltage and share power with the battery.

Table 3.6: Maximum motor current ripple in different designs

Architecture	Interleaved + inverter	Z-source inverter	Split-source inverter	Multi-source inverter
Id	15.6	14.7	13.6	37.7
Iq	8.3	14.4	14.8	16.5

3.9.5 Final comparison

The different comparisons between the designs are summarized in Table 3.7, here 0 means the performance was almost equal to that of the interleaved boost converter with inverter design, a + is used when the design improves the performance and a - is used when the design has a worse performance. When the performance is significantly different, two ++ or −− are used. As the output voltage range and maximum output current are strongly related by required field weakening, only the maximum output current is included in the final comparison. The result of the comparison is that the overall performance of the dual-DC-port converters is lower than what is found when the boosting of the fuel cell voltage is separated from the generation of the AC voltage. The multi-source inverter is the only dual-DC-port inverter that had a comparable result to the reference design, with its main advantage being the reduced passive component size. The advantage of reducing the number of converters and thus simplifying the system makes it worth further exploring the multi-source inverter for this application in a lab setting, which is done in chapter 5.

Table 3.7: Performance of dual-DC-port inverters compared to the standard boost converter with inverter

Architecture	Z-source inverter	Split-source inverter	Multi-source inverter
Transient response	0	+	0
Maximum current	0	−−	−
Current ripple	0	0	−
Switching losses	−−	−	0
Passive component mass	−−	−	++
Total	-4	-3	0

4. Multi-objective vector modulation

A solution is required to control the three phases of the T-type multi-level inverter. This method should generate the output voltage as desired by the motor controller while maintaining the desired fuel cell power at the same time. A vector modulation approach is considered that can satisfy these requirements in the different scenarios encountered during a flight mission. The main challenge compared to existing solutions is to control the desired fuel cell power, independent of the output voltage, torque and power factor of the motor.

4.1 Vector space

The three phase legs of the inverter can take three different states each, choosing from V_{DC_1}, V_{DC_2} or a common 0 voltage. Each combination of (V_a, V_b, V_c) represents a basic vector, which is converted to the $\alpha\beta0$ reference frame using the Clarke transform. In total, 27 possible basic vectors are available. In an effort to separate calculations on the power delivered by the two DC voltage sources only the independent active vectors and the common zero vector are used. The 13 basic vectors of interest are shown in figure 4.1. A given reference vector can be created in this vector space in an infinite number of ways using any combination of basic vectors with certain scalar duty cycles that scale the individual basic vectors. A number of constraints can be introduced to reduce the number of possibilities and to choose the best vectors for a certain situation. This method and the following port vector approach are based on the control strategy described by Liu et al. [47] but this strategy makes use of six more active vectors to improve the output voltage range.
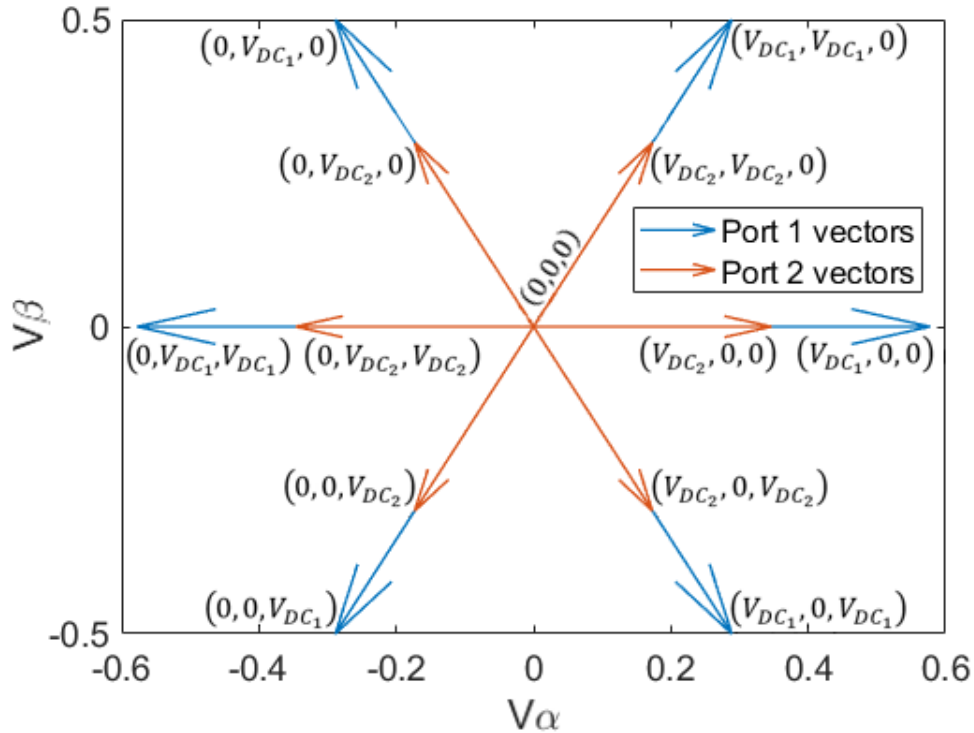

Figure 4.1: Vector space of the multi-source inverter

4.1.1 Port vectors

The motor controller generated reference voltage U_{ref} can be separated into two port vectors U_1 and U_2, one for each DC voltage source. These vectors add up to U_{ref} as shown in equation 4.1. In turn, these port vectors can be constructed using the 6 basic vectors of the respective port.

$$U_{ref} = U_1 + U_2 \tag{4.1}$$

The two port vectors can each be generated from their respective basic vectors using the rules of normal two-level SVPWM. This means that each port vector is generated by the two closest active vectors in the vector space which minimizes the required duty cycle to generate the port vector. In total, 4 active vectors with a respective duty cycle τ and a remaining zero vector generate the reference vector as shown in equation 4.2. An example of this method is shown in figure 4.2.

$$U_1 = \tau_{1a}U_{1a} + \tau_{1b}U_{1b}$$

$$U_2 = \tau_{2a}U_{2a} + \tau_{2b}U_{2b}$$

$$U_{ref} = \tau_{1a}U_{1a} + \tau_{1b}U_{1b} + \tau_{2a}U_{2a} + \tau_{2b}U_{2b} + \tau_0 U_0 \tag{4.2}$$
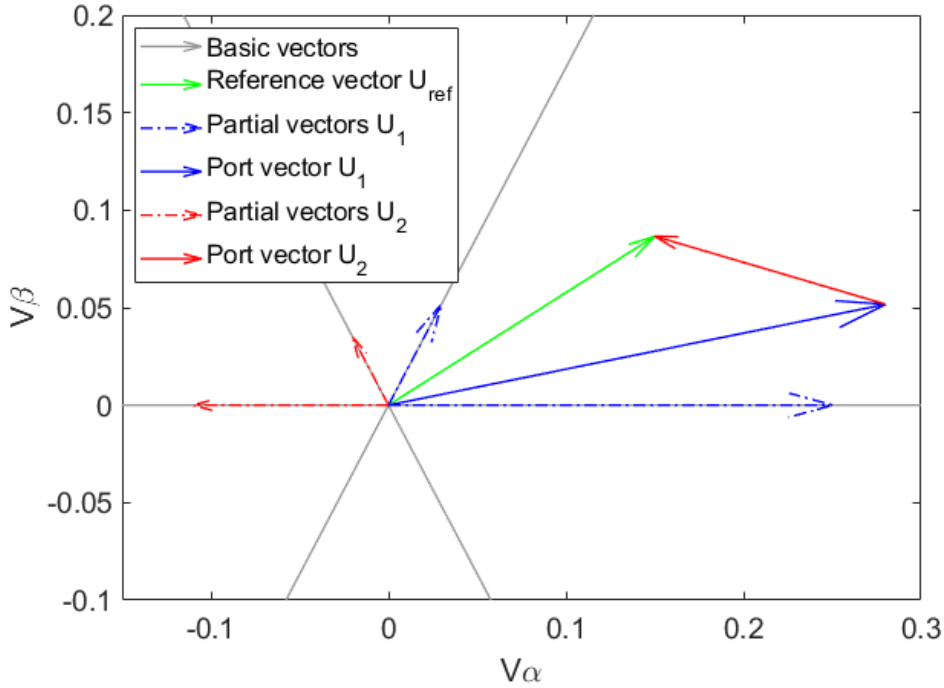

Figure 4.2: Port vector creation and addition

4.1.2 Available vector magnitude

With standard SVPWM the magnitude of the ac voltage vector is limited by the available basic vectors. When aligned with one of these vectors the magnitude can go up to $\frac{2}{3}V_{DC}$ but when the vector is created with two neighbouring basic vectors some range is lost and when the reference vector is exactly between two basic vectors the magnitude is limited to $\frac{1}{\sqrt{3}}V_{DC} \approx 0.577V_{DC}$. This limit is approximately 15% higher than the $0.5V_{DC}$ limit of SPWM. In general the lower limit of $\frac{1}{\sqrt{3}}$ is used for all angles of the reference vector. With the dual DC ports, the magnitude of the AC reference vector $|U_{ref}|$ is still limited by the largest dc voltage at port 1 with $\frac{V_{DC_1}}{\sqrt{3}}$. In addition to this, individual port vectors are limited by their respective DC voltages, where $|U_1|$ is also limited by $\frac{V_{DC_1}}{\sqrt{3}}$ and $|U_2|$ is limited by $\frac{V_{DC_2}}{\sqrt{3}}$. As only one vector can be placed on the output at a given time, the two port vectors also have a shared limit as shown in equation 4.3, it can be seen that when one of the vectors has a magnitude of 0, the equation returns to the individual limit of the other vector. When this shared magnitude limit is combined with the vector addition of equation 4.1 a solution can be found for the available vector magnitude of the second DC port.

$$\frac{|U_1|}{\frac{V_{DC_1}}{\sqrt{3}}} + \frac{|U_2|}{\frac{V_{DC_2}}{\sqrt{3}}} = 1 \tag{4.3}$$

To simplify the relations, $|U_{ref}|$ and V_{DC_2} are normalized to V_{DC_1} as shown in equation 4.4.

$$U = \frac{|U_{ref}|}{\frac{V_{DC_1}}{\sqrt{3}}} \quad \text{and} \quad V = \frac{V_{DC_2}}{V_{DC_1}} \tag{4.4}$$

The lower limit of the vector magnitude of port 2 can now be solved to the formula shown in equation 4.5. This equation shows a dependence of the available vector magnitude on the angle between vectors U_{ref} and U_2 (θ_{2-ref}) and the normalized U and V, which is scaled back with $\frac{V_{DC_1}}{\sqrt{3}}$.

$$|U_{2,max}| = \frac{V_{DC_1}}{\sqrt{3}} \frac{V}{1-V^2} \left(1 - UV\cos(\theta_{2-ref}) - \sqrt{U^2 + V^2 - U^2V^2 - 2UV\cos(\theta_{2-ref}) + U^2V^2\cos^2(\theta_{2-ref})} \right) \tag{4.5}$$

Figure 4.3 shows an overview of the vector space of the multi-source inverter with the full and lower limits of individual vectors as well as the upper limit of $|U_2|$ that satisfies equation 4.3 which could only be found numerically and the lower limit of $|U_2|$ that was found with Equation 4.5. The upper limit was found to be up to 20% larger than the lower limit, however, this upper limit is not reliable and will change depending on the angle of U_{ref}. This dependence will cause a ripple in the fuel cell power with a frequency of 6 times the fundamental frequency of the AC output voltage, due to the six segments of the hexagon. The lower limit in equation 4.5 is independent of θ_{ref} however and will yield a constant maximum port voltage when rotated through the vector space.
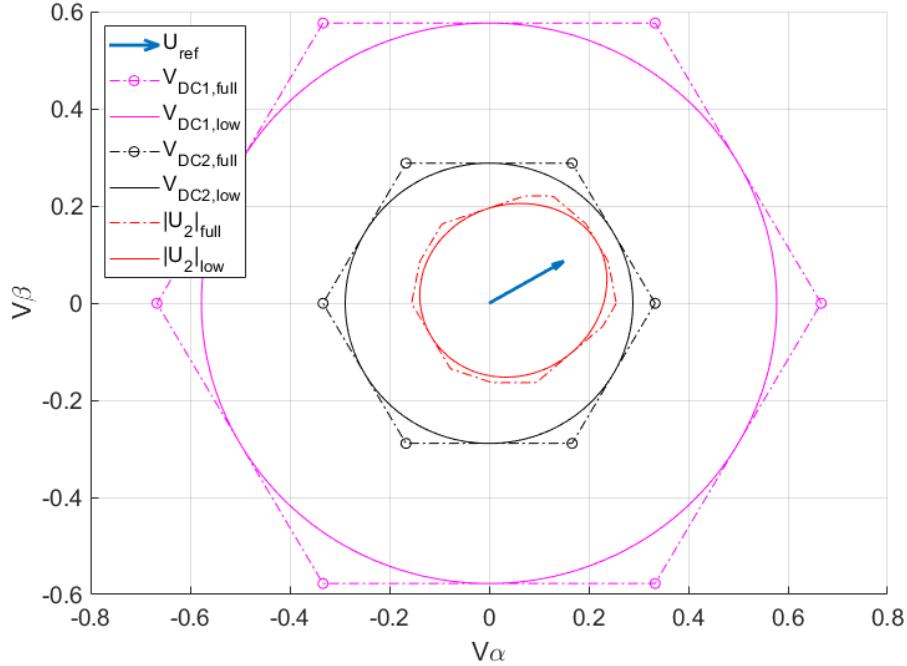

Figure 4.3: Vector limits when V = 0.5 and U = 0.3

4.2 Available port power

The active power delivered by a DC port can be calculated using the port voltage vector and the measured phase current vector as shown in 4.6. This equation can be rewritten to calculate the magnitude of a port vector based on the desired power and the power factor as seen in equation 4.7. In this way, the fuel cell power of the aircraft can be controlled using the existing measurements of the motor currents and the DC voltages. It can be possible however that the desired vector magnitude exceeds the limits shown in 4.5, meaning that the desired power can not be reached. The maximum power that can be delivered by port 2 is calculated using equation 4.8.

$$P_x = 1.5|U_x||I_L|\cos(\theta_{I-x}) \tag{4.6}$$

$$|U_x| = \frac{P_x}{1.5|I_L|\cos(\theta_{Ix})} \tag{4.7}$$

$$P_{2,max} = 1.5|I_L||U_{2,max}|\cos(\theta_{I-2}) \tag{4.8}$$

The maximum available power for the second DC port is now shown to depend on V_{DC_1}, V_{DC_2}, θ_{I-2}, θ_{2-ref} and $|U_{ref}|$. Most of these variables can not be controlled directly without interfering with the motor control algorithm. Two things that can be changed are the amount of field weakening current I_D and the angle of the port vector θ_2. For a power factor of 1 or -1, where θ_{I-ref} is zero, this limit corresponds to the limit described by Fedele et al. [45, Fig. 7]. The novelty of the algorithm discussed in this chapter is that it improves the available port power for all other power factors.

4.2.1 Field weakening

In a permanent magnet synchronous machine a sinusoidal back EMF is generated in the motor windings. This back EMF is proportional to the angular velocity of the motor ω_m, the number of pole pairs p in the motor and the flux φ_{pm} generated by the permanent magnets as shown in equation 4.9. Due to the alignment of the DQ reference frame in the motor model, this back EMF is added to v_q as seen in Equation 3.5.

$$E_b = p\omega_m\varphi_{pm} \tag{4.9}$$

The voltage generated by the inverter needs to be at least as large as this back EMF for the motor to have a positive output power. This means that the rotational velocity of the motor is limited by the DC voltage following equation 4.10. At this limit the available vector magnitude for port 2 reduces to zero. Once a torque is applied to the motor output, the voltage drop over the phase resistance and inductance decreases this limit.

$$\omega_{m,max} = \frac{V_{DC_1}}{\sqrt{3}}\frac{1}{p\varphi_{pm}} \tag{4.10}$$

Field weakening allows the motor velocity to go beyond this limit by reducing the required output voltage by placing a negative current on the d-axis. Equation 4.11 shows the equation for v_q from Equation 3.5 but rewritten to show how the flux generated by i_d in the phase inductance can be added to the motor flux. When i_d is negative the total flux is effectively reduced, resulting in a lower v_q. The addition of i_d also results in a change in v_d due to the resistive losses.

$$v_q = R_s i_q + p\omega_m(\varphi_{pm} + Li_d) \tag{4.11}$$

The field weakening current will now decrease the overall output voltage $|U_{ref}| = \sqrt{v_d^2 + v_q^2}$, which will increase the available port vector magnitude following equation 4.5. In addition, the magnitude of the motor current $|I_L| = \sqrt{i_d^2 + i_q^2}$ will increase which will also increase the available port power following equation 4.6. Finally, the angle of the current vector θ_I will also change, which can improve the output power if θ_I becomes closer to θ_{ref} but it can also have a negative effect on the available power. These changes all occur without interference on the control of the motor. In general, field weakening boosts the available power for port vector 2. The trade-off is that this current introduces additional losses in the motor windings and reduces the system efficiency. To prevent the motor from overheating the total current magnitude $|I_L|$ is often limited. The resulting objective is to minimize the field weakening current to improve efficiency while still generating the desired port power at the desired motor RPM.

4.2.2 Optimal power angle

The second parameter that can be adjusted is the angle of port vector U_2. From equation 4.6 it seems intuitive to place the vector in phase with I_L, as this results in a port power factor of 1 which results in the most active power for a given port vector magnitude. At the same time it also seems intuitive to align the vector with U_{ref} as that maximizes the limit of the port vector magnitude and in turn maximizes the apparent power of the port. It turns out that the optimal angle, or the angle where the available power of port 2 is the highest, is located between θ_{ref} and θ_I. This can be seen in figure 4.4 where a maximum in the active power can be found between θ_I and θ_{ref}, this optimal angle depends on the voltages of both DC sources, the magnitude of the output voltage $|U_{ref}|$ and the angle between U_{ref} and I_L. If this maximum angle is found and used, it decreases the amount of field weakening required to operate the fuel cell at the desired output power.
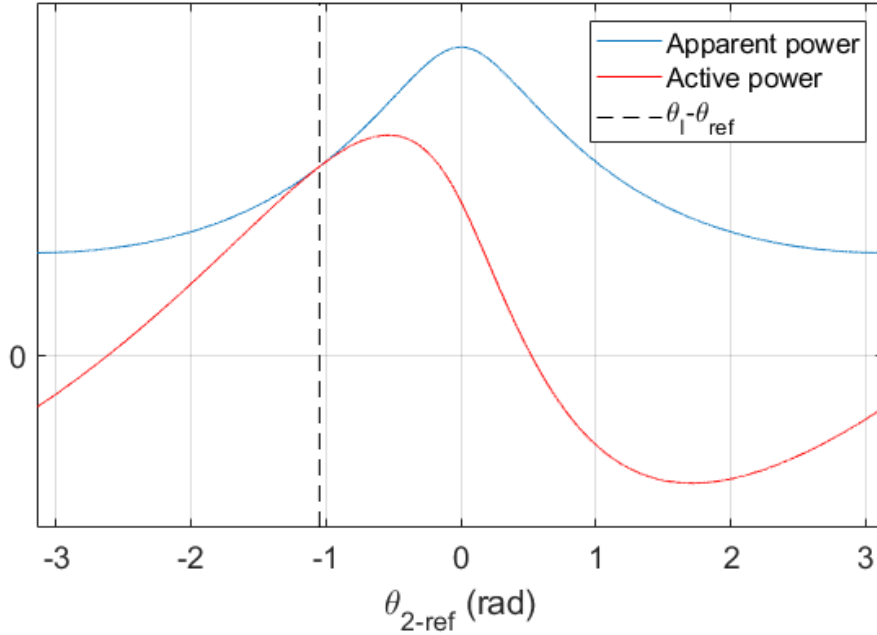
Figure 4.4: Example of the available apparent and active port power for port 2 as a function of the angle between U_{ref} and U_2. This example is made with $V_{DC_2} = \frac{2}{3}V_{DC_1}$, $|U_{ref}| = 0.5\frac{V_{DC_1}}{\sqrt{3}}$ and $\theta_{I-ref} = \frac{1}{3}\pi$
.

Sadly, no complete analytical solution for this optimization problem was found. The optimal angle θ_{2-ref} could be approximated for certain values of U, V and θ_{I-ref} by testing a large number of solutions and selecting the one where the available power was the largest. This process was very computationally intensive however and it is not feasible to test this many potential solutions in a real-time application. An alternative is to search for an analytical function that gives an estimate of the optimal angle using U, V and θ_{I-ref} as inputs. This function should be easier to solve for the controller hardware, balancing accuracy and computational resources. Figure 4.5 shows the optimal angle as it was found for a range of values of U and θ_{I-ref} where V is 0.5. This cross section looks similar for all other version of V and is symmetric between U and V. Certain aspects of this space follow known patterns which will be used to create the approximation.
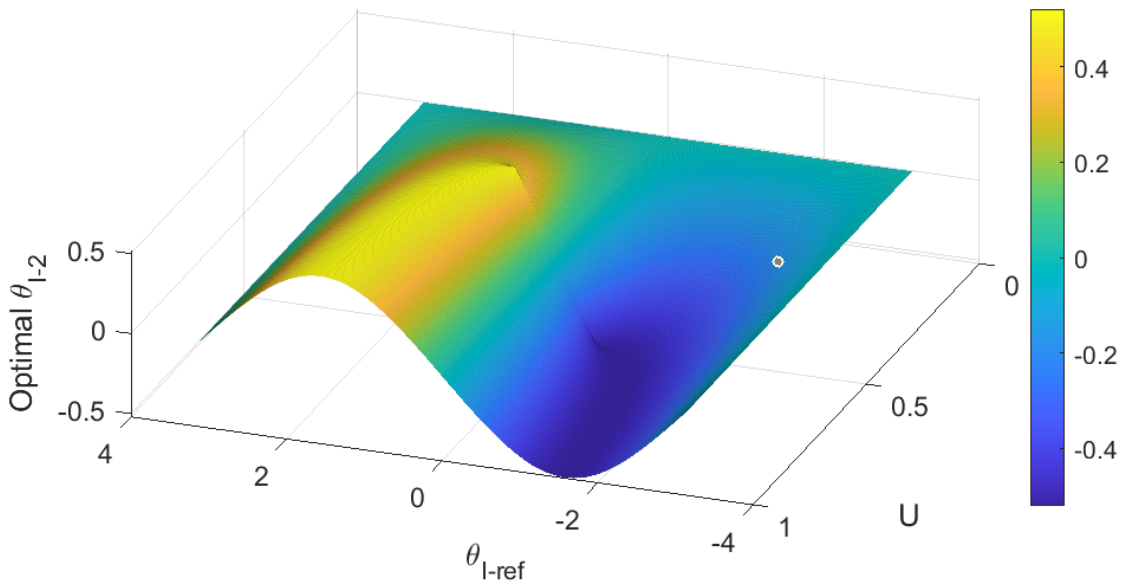

Figure 4.5: Cross section of the optimal angle space

Skewed sine wave

When the optimal angle is shown for a certain constant value of U and V and θ_{I-ref} is varied from $-\pi$ to π, the pattern shown in 4.6 appears. The optimal angle appears to follow a sinusoidal pattern, being equal to 0 when θ_{I-ref} is 0, π or $-\pi$ and following a similar curve. The observed pattern does not exactly match a sine wave but appears tilted, becoming more tilted when $U \approx V$. This behavior can be mimicked by using the skewed sine function shown in equation 4.12. This function has an amplitude of 1 and remains 0 at $\theta = 0$, π and $-\pi$ but it moves the location of the maximum of the function with $\frac{\pi}{2}n$, where n is the skew factor. This skew factor was found to be approximately $n = \frac{V}{U} - V$ when $U > V$ or $n = \frac{V}{U} - U$ when $U < V$. This skewed sine wave closely follows the data for most values of U and V, but becomes less accurate when $U \approx V$.

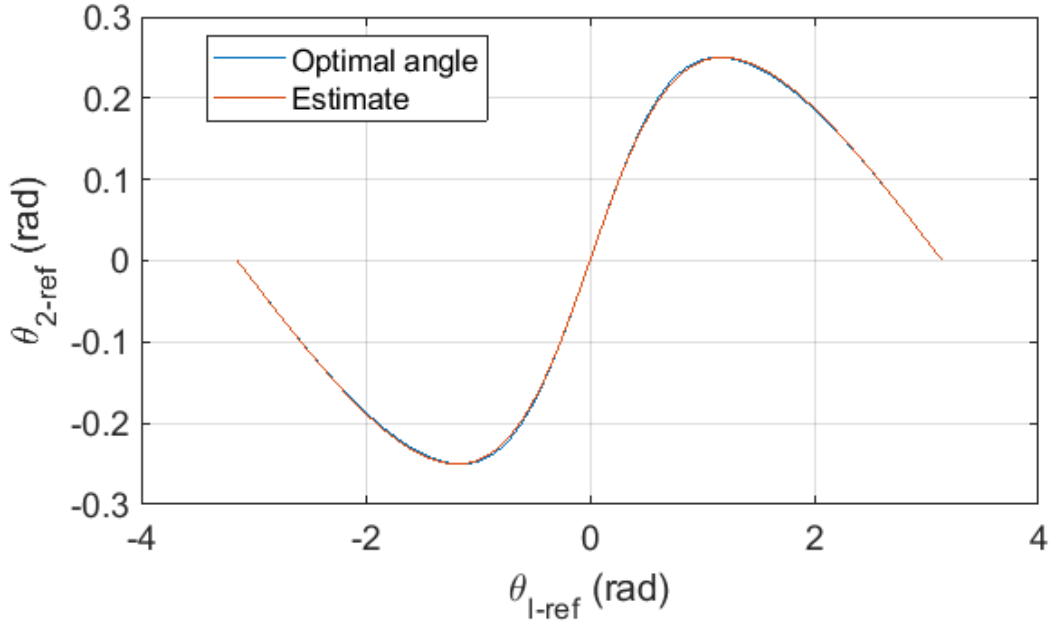$$\text{Skew}(n, \theta) = \frac{sin(\theta)}{\sqrt{1 + n^2 - 2n \cos(\theta)}} \tag{4.12}$$

Figure 4.6: Values for the optimal angle where U = 0.25 and V = 0.4

Magnitude of skewed sine

In addition to the skewed sine wave, the magnitude of the skewed sine wave was observed to follow the relation shown in Equation 4.13. This relation was found after observing the surface shown in Figure 4.7, here the amplitude of the skewed sine wave is observed to follow $sin^{-1}(U)$, up until $U = V$, after which it remains constant, this holds true for all values of U and V. When U or V is equal to 1, the amplitude follows the full arcsine function. This relation is still an estimate based on observation and could not be solved algebraically.

$$\theta_{I-2}(U, V, \theta_{I-ref}) = \begin{cases} \arcsin(V \, \text{Skew}(\frac{V}{U} - V, \theta_{I-ref})) & \text{if } U > V \\ \arcsin(U \, \text{Skew}(\frac{U}{V} - U, \theta_{I-ref})) & \text{otherwise} \end{cases} \tag{4.13}$$
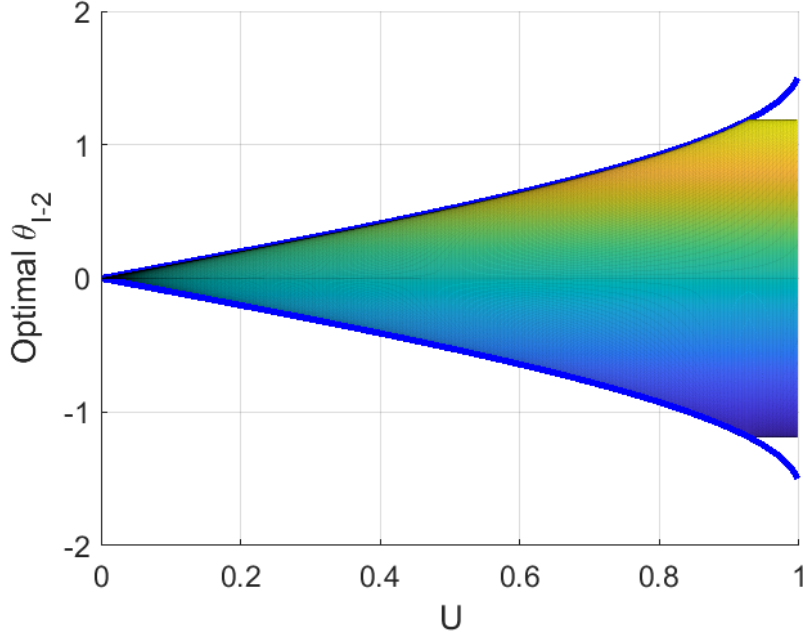
Figure 4.7: Side view of the optimal angle cross section where V = 0.93 with $\pm \sin^{-1}(U)$ in blue

Accuracy of optimal angle estimate

To find out how good this approximation performs, the available output power of the system at the previously calculated optimal angle is compared with the available output power using the estimated optimal angle. Figure 4.8a shows the error for varying V and U, the error was measured for all values of θ_{I-ref} and only the worst error is shown. As stated before, the approximation is less accurate when $U \approx V$, but even in the worst case it still retains 90% of the power. This can be compared to the intuitive estimate of aligning the port vector with the current for a port power factor of 1, which is shown in Figure 4.8b and shows a much larger error over the entire space. Although the minimum accuracy shown in Figure 4.8 is most important, the average accuracy over the entire space is about 99.99% when Equation 4.13 is used and the accuracy is only below 99% for 0.22% of the possible states.
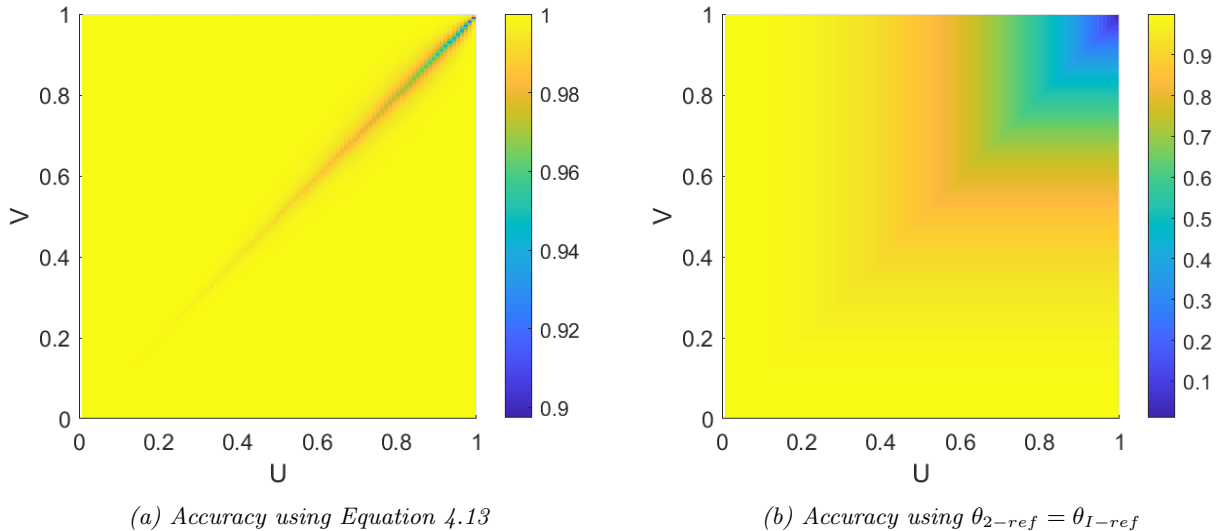

(a) Accuracy using Equation 4.13

(b) Accuracy using $\theta_{2-ref} = \theta_{I-ref}$

Figure 4.8: Accuracy in the available power of port 2 with different functions for θ_{2-ref}

Field weakening reduction in flight scenarios

The question remains, how much the field weakening can be reduced when the optimal power angle is used. To quantify the improvement, the required field weakening is calculated using equations 3.5, 3.6 and 4.6. First, a benchmark is found by placing the port vectors in line with the reference vector resulting in $\theta_{2,ref} = 0$, this corresponds to the method of Fedele et al. [45]. A second calculation is done using the optimal angle

selection method of Equation 4.13. The angular velocity and torque of the motor are based on the load profile of Figure 2.2 and the DC voltage levels are based on the simulations of section 3.8. These input parameters and the resulting field weakening currents are shown in Table 4.1. It can be seen that the difference is small for the first three scenarios, in these scenarios the power factor of the motor is high and the angle between the current vector I_L and reference vector U_{ref} is small, which also results in a small optimal angle $\theta_{2-ref,opt}$ and a small difference with the benchmark. In the cruise scenario the power factor is around 77% when the required field weakening is applied and the difference when using the optimal angle is more significant, reducing the field weakening current by 7.9%. Finally, in the descent scenario the power factor is almost zero and the required field weakening current is reduced by 89% when the optimal angle is used. In this descent scenario the benchmark current is higher than the rated current of the motor. This means that the multi-source inverter would not have been a valid solution for this application without the optimal angle approach.

Table 4.1: Reduction of the field weakening current for different scenarios

Scenario	$P_{FC}(W)$	$\omega_m(\frac{rad}{s})$	$T(Nm)$	$V_{DC_1}(V)$	$V_{DC_2}(V)$	$I_{d,old}(A_p)$	$I_{d,opt}(A_p)$	$\theta_{2-ref,opt}(°)$
Standstill	4000	0	0	351.5	220.0	-34.1	-34.1	0.0
Takeoff	20000	256.6	237	333.7	178.3	-91.0	-91.0	1.0
Climb	20000	235.6	172.6	342.1	178.3	-101.7	-99.2	4.7
Cruise	20000	199.0	102.9	349.7	178.3	-133.5	-123.0	11.6
Descent	4000	125.7	1.5	351.5	220.0	-344.1	-37.5	66.2

4.3 Modulation scheme

The sum in equation 4.2 can be realised by applying each vector to the output for their respective duty cycle, resulting in an average output voltage equal to the reference vector. A modulation scheme is considered that limits the number of switching events, has a symmetric pattern and can be applied in an experimental setup.

4.3.1 RT Box digital output

As will be described in more detail in chapter 5, the algorithm will be tested using an RT-Box CE. When the controller is implemented on this RT-Box, the controller is limited to a fixed time-step operation which puts some additional constraints on the modulation scheme.

Digital out

One way to switch between different output states is by directly applying the desired output state via the Digital Out block from the RT-Box library in PLECS. The selected sample time now limits how accurate the time of switching is. In theory, the RT-Box CE can operate at up to 1 MHz, however, as the control algorithm takes some time to compute, a practical upper limit of 200 kHz was found. This means that the resolution in the switch duty cycles is limited to 5 μs. At the desired control cycle frequency of 16 kHz only 12.5 periods of this fundamental frequency are available to apply the 5 different output vectors to the output. As this is not sufficient an alternative has to be used.

PWM Out (Variable)

One alternative to the Digital Out block of the RT-Box software is the variable PWM Out block. This block has access to the internal 133 MHz FPGA clock which allows the output to vary with a more accurate pulse width. Instead of a direct output value this block accepts a duty cycle, variable frequency and delay of the carrier waveform. For the purpose of this project the frequency is kept constant. The duty cycle and delay can now be used to generate a series of alternating pulses that match the desired output.

4.3.2 Vector selection

To use the variable PWM Output block, the 5 output vectors needs to be arranged so that each switch only turns on and off once in a fixed period. This means that equal states of the three phases need to be grouped together into one continuous period. It is important to note that a port vector is always constructed with two basic vectors that are closest to the port vector. To find these nearest vectors the vector space is cut into 6 sectors based on the angle of the vector. A set of two basic vectors always consists of 1 vector with two phases at 0 V and one phase at either V_{DC_1} or V_{DC_2} and another vector with a second phase at V_{DC_1} or V_{DC_2}. Vectors with one high state will be assigned as U_{1a} and U_{2a} and the vectors with two high states to U_{1b} and U_{2b}. The

resulting vector assignment is shown in table 4.2, this selection is done for both port vectors which can have different sector numbers.

Table 4.2: Vector selection for port vector x

Sector	1	2	3	4	5	6
Range	$0 \leq \theta < \frac{1}{3}\pi$	$\frac{1}{3}\pi \leq \theta < \frac{2}{3}\pi$	$\frac{2}{3}\pi \leq \theta < \pi$	$\pi \leq \theta < \frac{4}{3}\pi$	$\frac{4}{3}\pi \leq \theta < \frac{5}{3}\pi$	$\frac{5}{3}\pi \leq \theta < 2\pi$
U_{xa}	$(V_{DC_x}, 0, 0)$	$(0, V_{DC_x}, 0)$	$(0, V_{DC_x}, 0)$	$(0, 0, V_{DC_x})$	$(0, 0, V_{DC_x})$	$(V_{DC_x}, 0, 0)$
U_{xb}	$(V_{DC_x}, V_{DC_x}, 0)$	$(V_{DC_x}, V_{DC_x}, 0)$	$(0, V_{DC_x}, V_{DC_x})$	$(0, V_{DC_x}, V_{DC_x})$	$(V_{DC_x}, 0, V_{DC_x})$	$(V_{DC_x}, 0, V_{DC_x})$

4.3.3 Switching pattern

Once the correct basic vectors have been selected, a switching pattern can be created as shown in table 4.3. The complete pattern lasts for one control cycle but an interface is used that updates the PWM output halfway through the control cycle resulting in a PWM frequency of twice the control frequency. The second half of the cycle is equal to the first half of the cycle in reverse to create a symmetric pattern. As only the $(0, 0, 0)$ zero vector is used, the transition from U_0 to U_{1a} or U_{2a} only requires one phase to change state. This is also true for the transition from U_{1a} to U_{1b} and U_{2a} to U_{2b}. Only on the transitions from U_{1b} to U_{2b} more than one phase changes state at the same time. In total, there are at most 14 state transitions during one control cycle.

Table 4.3: Switching pattern

Name	U_0	U_{1a}	U_{1b}	U_{2b}	U_{2a}	U_0	U_{2a}	U_{2b}	U_{1b}	U_{1a}	U_0
Duration	$\frac{\tau_0}{4}$	$\frac{\tau_{1a}}{2}$	$\frac{\tau_{1b}}{2}$	$\frac{\tau_{2b}}{2}$	$\frac{\tau_{2a}}{2}$	$\frac{\tau_0}{2}$	$\frac{\tau_{2a}}{2}$	$\frac{\tau_{2b}}{2}$	$\frac{\tau_{1b}}{2}$	$\frac{\tau_{1a}}{2}$	$\frac{\tau_0}{4}$

4.3.4 Variable delay and duty cycle

The vectors from the switching pattern can be converted into 9 duty cycles and delays, one for each switching state of each phase. The delay can be used to place the different vectors in the right order and the duty cycle is based on the duration of each state, which is the sum of the vector duty cycles where this state is present. Figure 4.9 shows an example of such a control cycle based on two PWM periods. A sawtooth carrier is used where the delay corresponds to the start or end of a pulse, depending on the polarity. For each phase the 0 state is based on a reverse polarity where the switch Q_1 is on when $m < c$ and the delay is equal to when the switch turns off. The other switches are on when $m > c$ and the delay corresponds to the moment the switch turns on.
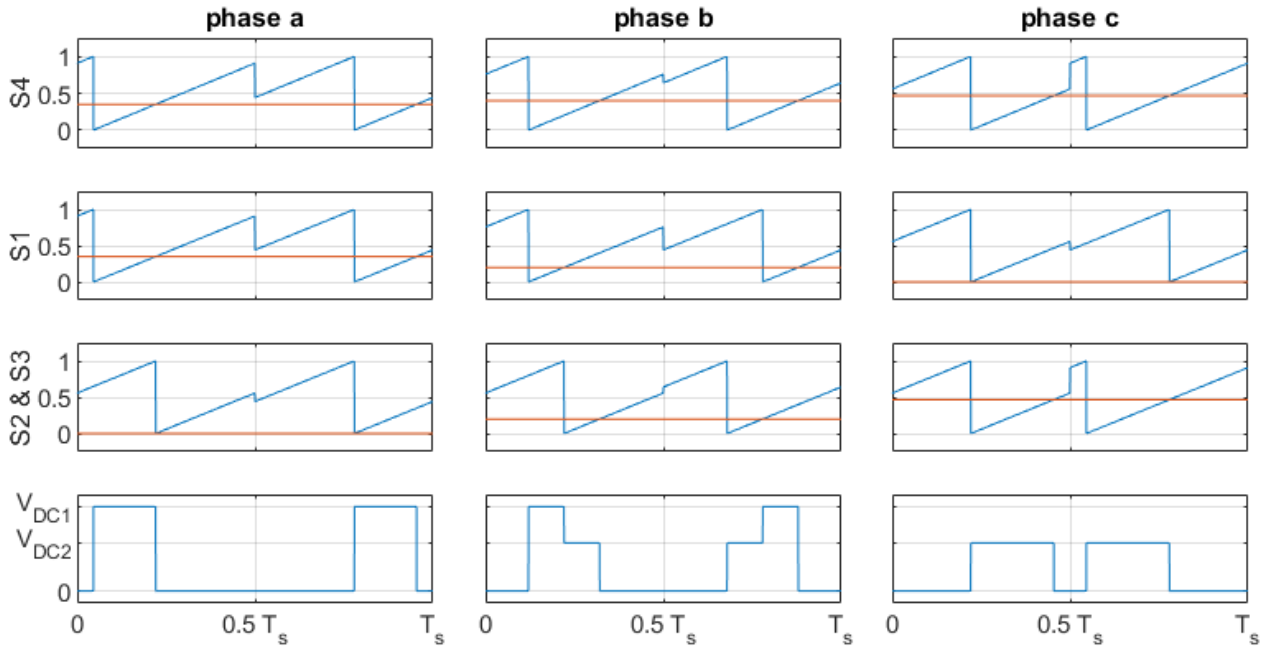

Figure 4.9: Output of the inverter over one controller cycle

5. Experimental results

The multi-objective vector modulation algorithm is tested in an experimental setup to validate the theoretical analysis in chapter 4. As suitable batteries, fuel cell and motor are not available for these tests, this setup will replace these systems with devices that are equivalent from the perspective of the MOVM algorithm.

5.1 Setup

The final setup used for validating the MOVM algorithm is shown in Figure 5.1. In short, the RT-Box and T-type inverter are the device under test. The LC filter and Cinergia EL-15 are an equivalent of the motor and mechanical system under certain conditions and the two DC power supplies replace the battery and fuel cell systems. In this section, these systems are further explained.
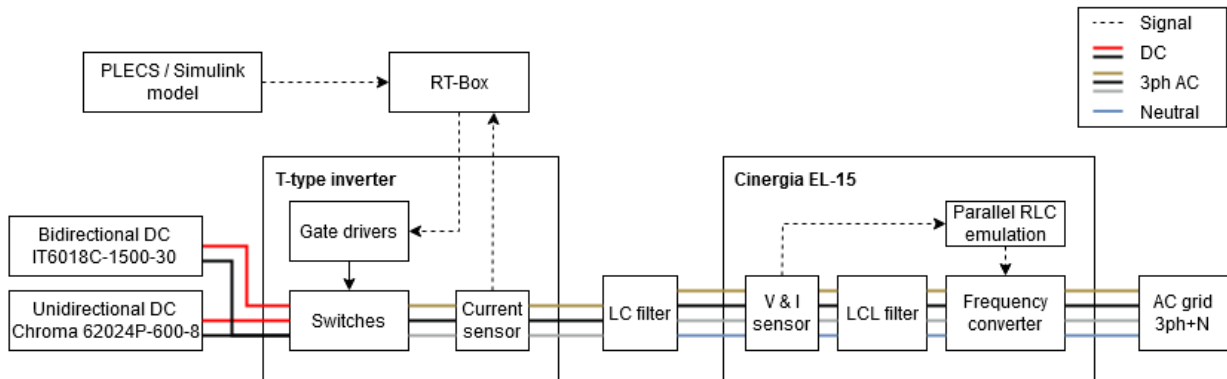

Figure 5.1: Diagram of the experimental setup

5.1.1 RT-Box

As mentioned before, the controller is implemented on a RT-Box CE [48], which enables the deployment of PLECS models to hardware with some RT-Box specific PLECS components. This system has a number of Digital outputs used for enable and PWM signals as well as digital and analog inputs which can be used to read sensors. In this setup, three digital input channels are used to measure the inverter outputs currents and one PWM Out block generates the twelve PWM signals on individual digital output pins that connect to the inverter gate drivers. Some additional connections are implemented to read and control safety and enable signals. In the RT-Box, the motor control algorithm is replaced with a constant voltage reference and a current sensor. In addition, a constant fuel cell power is set for the MOVM algorithm.

5.1.2 T-type inverter

An existing T-type inverter was available in the lab, although this inverter would normally be used as a symmetric and balanced three-level inverter using one DC input, it was possible to connect the second DC source to the center voltage and to use it as the desired asymmetrical multi-source inverter.

Current sensors

The inverter included current sensors that could be used to operate the design in closed loop. The current sensor had an analog voltage as output, which was converted to a digital signal with a 10 MHz delta-sigma modulator. This delta-sigma data signal could be captured with the PWM In block of the RT-Box library, which measures the average input value over one time step.

5.1.3 DC power supplies

The battery and fuel cell systems are replaced with constant voltage power supplies. The fuel cell is replaced with an uni-directional power supply, the current of this supply is measured to validate the power control segment of the modulation algorithm. The battery system is a bi-directional power supply which makes it possible to test the system in scenarios where the battery is recharged.

5.1.4 Cinergia EL-15

As it was not possible to find a suitable permanent magnet machine to test the inverter on, a regenerative electronic load was used instead. The available system was the Cinergia EL-15. This machine can operate as a load for frequencies between 10 and 400 Hz, just shy of the up to 408 Hz seen in simulations. This means that the load can be used to test most load scenario's except for the idle power transfer from fuel cell to battery at standstill. The input voltage range is 480 Vrms phase-phase for frequencies below 100 Hz, but gradually decreases to 115 Vrms phase-phase at 400 Hz due to limited $\frac{dV}{dt}$ capabilities of the system. The Cinergia was set up as a parallel RLC load, where it measures the voltage at its output and controls its switches to generate the appropriate current.

LC filter

As the Cinergia generates its current based on the output voltage, it is important to filter the inverter output to some degree, removing most of the high frequency components generated by the PWM voltage. In addition, it allows the three wire inverter to interface with the neutral port of the Cinergia. The phase inductors were wound in the lab and measured to have an inductance of 600 μH with a series resistance of about 0.14 Ω. The phase to neutral capacitance was made with two parallel capacitors for a total of 4.4 μF. This results in a attenuation of 30 dB or more at the switching frequency range of 16-48 kHz.

5.2 Equivalent operating conditions

The goal is to run the setup in a configuration that is as similar as possible to the simulations, but different constraints from the electronic load, dc power supplies and the inverter can limit the output voltage, current and frequency. In turn, multiple methods are considered that can bring the output conditions to within the specifications without changing the behavior of the MOVM algorithm.

5.2.1 Loading scenarios

The setup is suited to test quasi steady state scenarios found in the load profile of a flight as seen in Figure 2.2. With the frequency range of the Cinergia, it is possible to test takeoff, climb, cruise and descent scenarios in quasi-steady state, where the output frequency, voltage and current are constant. An early set of simulations was done with a simplified battery and fuel cell model that resulted in the load scenarios shown in Table 5.1.

Table 5.1: Simulated load scenarios

Scenario	Frequency (Hz)	$U_{ref,dq}$ (Vp)	$I_{L,dq}$ (Ap)	V_{BAT} (V)	I_{BAT} (A)	V_{FC} (V)	I_{FC} (A)
Takeoff	400	(-46.5, 149.5)	(-35.5, 264)	350	120	200	100
Climb	375	(-31.5, 138.5)	(-40.5, 187)	350	63	200	100
Cruise	318	(-16, 108.5)	(-106, 107.5)	350	0	200	100
Descent	200	(-0.8, 70.3)	(-73.2,0)	350	-20	220	34.5

5.2.2 Voltage and current scaling

The inverter, Cinergia and DC power supplies are not able to supply the high current and power found in Table 5.1 and at high frequencies the Cinergia also is not able to handle the amplitude of U_{ref} seen in the takeoff and climb scenarios. The load scenario can be adjusted to be within the device ratings by lowering all currents and or voltages by the same ratio. If the reference fuel cell power is also scaled by the current and voltage, all ratios and angles should stay the same. The MOVM algorithm already normalizes everything and the outputs of the controller should be the same as before scaling. The takeoff and climb voltage is divided by 2 to stay within the Cinergia voltage rating, the current is divided by 25 to stay within the inverter and DC supply current rating. At the lower frequencies of cruise and descent, the voltage can remain at the original levels. As the power is also lower in these scenarios, the current is only divided by 20.

Scenario	Frequency (Hz)	$U_{ref,dq}$ (Vp)	$I_{L,dq}$ (Ap)	V_{BAT} (V)	I_{BAT} (A)	V_{FC} (V)	I_{FC} (A)
Takeoff	400	(-23.3, 74.8)	(-1.4, 10.6)	175	4.8	100	4
Climb	375	(-15.8, 69.3)	(-1.6, 7.5)	175	2.5	100	4
Cruise	318	(-16, 108.5)	(-5.3, 5.4)	350	0	200	5
Descent	200	(-0.8, 70.3)	(-3.7,0)	350	-1	220	1.7

5.2.3 Equivalent machine impedance

Figure 5.2 shows the power circuit of the system in more detail. The voltages V_a, V_b and V_c are the PWM output voltages as set by the controller and will correspond to U_{ref} but V_a^*, V_b^* and V_c^* are the filtered voltages as seen by the Cinergia. The goal is for the circuit at the interfaces of the inverter to behave like what is seen in the load scenarios.
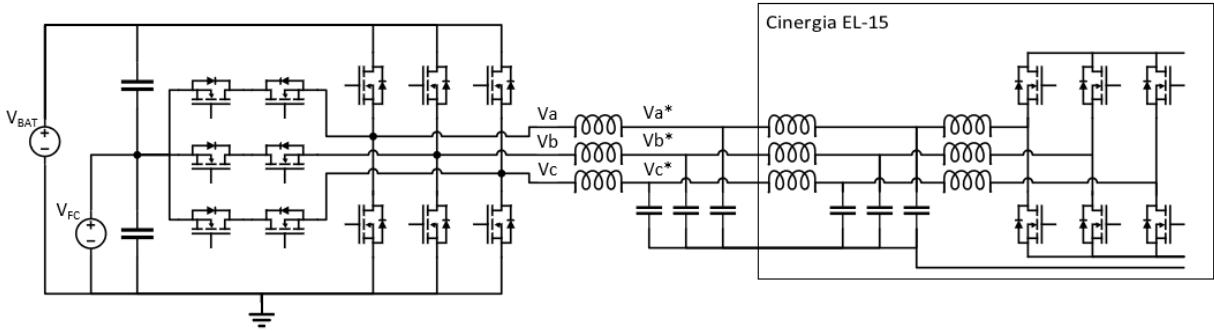

Figure 5.2: T-type inverter feeding a Cinergia load with filter to emulate the power distribution system of the electric aircraft

The parallel RLC impedance of the Cinergia should be configured to generate the correct output current at the inverter, this means that the delay and voltage drop over the LC filter should also be taken into account. A phase to neutral equivalent circuit is shown in Figure 5.3 where the filter inductor L_f and capacitor C_f are combined with the Cinergia output inductor L_o, capacitor C_o and resistor R_o. Once some initial tests were done the actual output voltage was found to be lower than expected, following a resistive voltage drop of around 0.7 Ω in series with L_f, which is included as the resistor R_f.
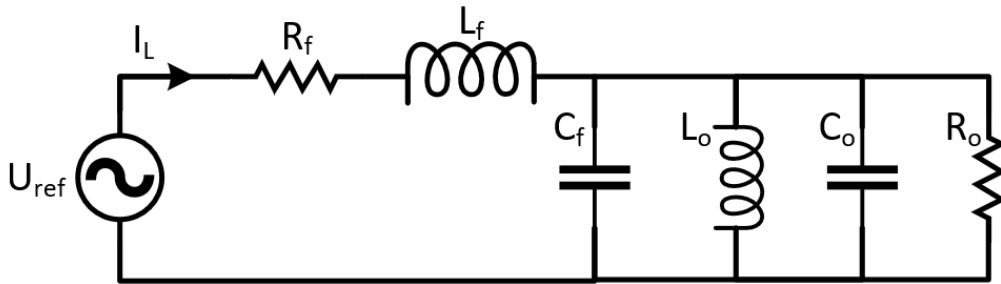

Figure 5.3: Equivalent circuit of the inverter output

The dq components of $U_{ref,dq}$ and $I_{L,dq}$ can be converted into complex values with the direct component as the real value and the quadrature component as the imaginary value. After this, the ratio between the two results in the complex output impedance, which can also be calculated for the output circuit as shown in Equation 5.1. The values of R_o, C_o and L_o now need to be selected to match this equation.

$$Z_o = \frac{U_{ref,d} + U_{ref,q}j}{I_{L,d} + I_{L,q}j} = R_f + j\omega L_f + \frac{1}{j\omega C_f + j\omega C_o + \frac{1}{j\omega L_o} + \frac{1}{R_o}} \tag{5.1}$$

The output resistance can be calculated by looking at the real part of the admittance behind the filter inductor. The resulting equation is shown in Equation 5.2.

$$R_o = \frac{1}{\Re(\frac{1}{Z_o - j\omega L_f - R_f})} \tag{5.2}$$

The output inductance and output capacitance are not as straightforward to calculate as there is more than one valid combination of the two. The choice was made to minimize the output capacitance and to use a corresponding output inductance. If the capacitance was too small the required inductance could be negative, the capacitance was increased in steps of $10\mu F$ until a valid inductance was encountered. This was calculated using the imaginary part of the admittance behind the filter inductance as seen in Equation 5.3.

$$L_o = \frac{1}{\omega}\frac{1}{(C_o + C_f)\omega - \Im(\frac{1}{Z_o - j\omega L_f - R_f})} \tag{5.3}$$

This process was used for the four different scenarios seen in Table 5.2. The resulting impedance, power factor and RLC parameters are shown in Table 5.3. The final descent impedance is slightly different from the target as the series resistance R_f is larger than the target resistance. As a result, the lowest possible real impedance was selected with R_o and L_o at their maximum values and C_o was selected to get the correct imaginary part of the impedance.

Table 5.3: RLC parameters for each load scenario

Scenario	Z_o (Ω)	PF (%)	R_o (Ω)	L_o (mH)	C_o (μF)
Takeoff	7.2 + 1.2j	98.6	6.6	86	0
Climb	9.3 + 0.13j	100.0	8.8	22.6	10
Cruise	11.7 - 8.5j	80.8	19.7	21.1	30
Descent	0.22 - 19j	1.14	1000	1000	36.5

5.3   Results

The four scenarios were executed on the setup and the most interesting waveforms were captured on an oscilloscope. These waveforms are the voltage between phase A and the DC ground in yellow, the voltage between phase B and phase C in cyan, the current of phase A in pink and finally the current of the second DC power supply in green. In addition, the oscilloscope data was stored for data processing and some of the signals on the RT-Box were also captured during the experiments.

5.3.1   Takeoff

The first scenario that was tested is during takeoff. After some initial debugging, the systems mostly behaved according to expectations: the measured DC current was 3.95 A on average where the goal was 4 A, The measured phase current was 7.59 A_{rms} compared to the targeted 7.56 A_{rms} and the measured frequency was indeed 400 Hz. A few noteworthy differences with the simulations will be explored further.
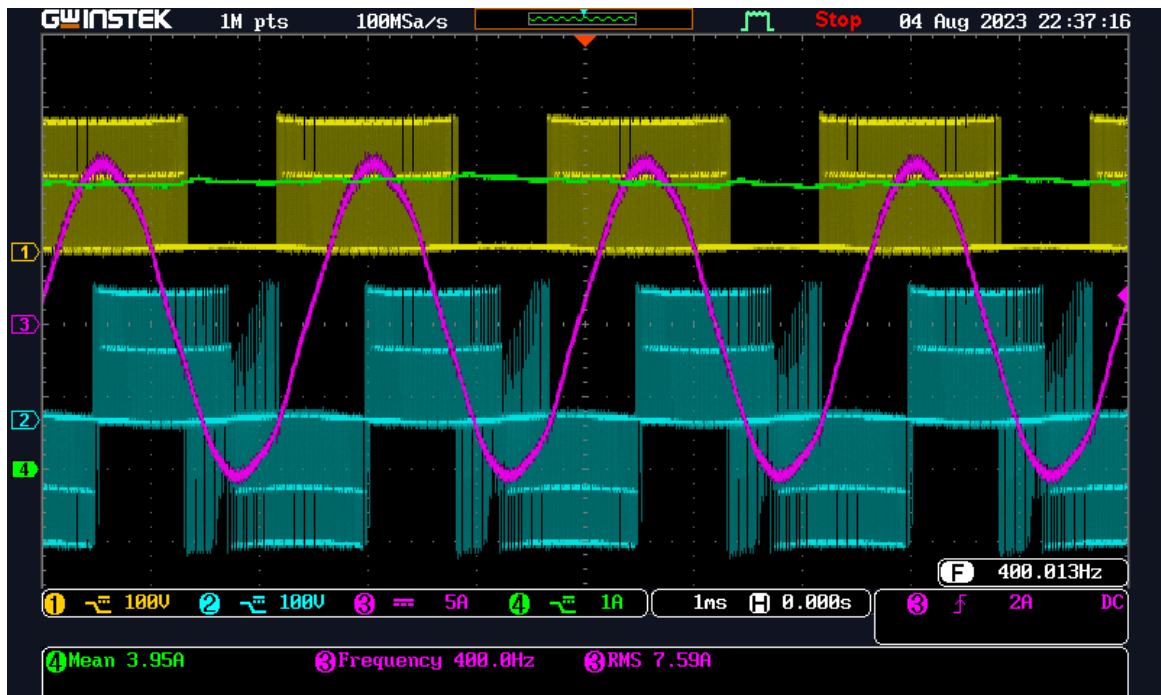

Figure 5.4: Experimental waveforms during the takeoff scenario

AC current distortion

The AC current waveform seen in Figure 5.4 shows some amount of low frequency distortion. This distortion appears to be mainly in the 5th and 7th harmonic of the current. This distortion was not present in the output voltage waveforms and it is not clear where the distortion comes from.

DC current distortion

The DC current from the second DC power supply in Figure 5.4 also shows some deviation from the target $4\ A$ with a standard deviation of $40\ mA$, about 1%. If the power estimation was perfect, this current would be constant without distortion. There are multiple causes for imperfections to the power estimate, including inaccuracies in the current sensing and DC voltage levels or the dead time which influences the output voltage. This may be the largest challenge for the power control algorithm, which requires accurate measurements of the current with small delays.

Dead time behavior

The general switching behavior is as expected, however, there are some unexpected voltage spikes in the phase to phase voltage as seen in Figure 5.4. Upon closer inspection, these spikes are present in the transition between vectors, during the dead time of switches as seen in Figure 5.5. The spikes also last around 200 ns, which matches the dead time set at 175 ns. This behavior can be explained due to the filter inductors which push the voltage up to the positive battery voltage or down to the common ground, depending on the direction of the current, once the voltage reaches one of the rails, a switch body diode will start to conduct.
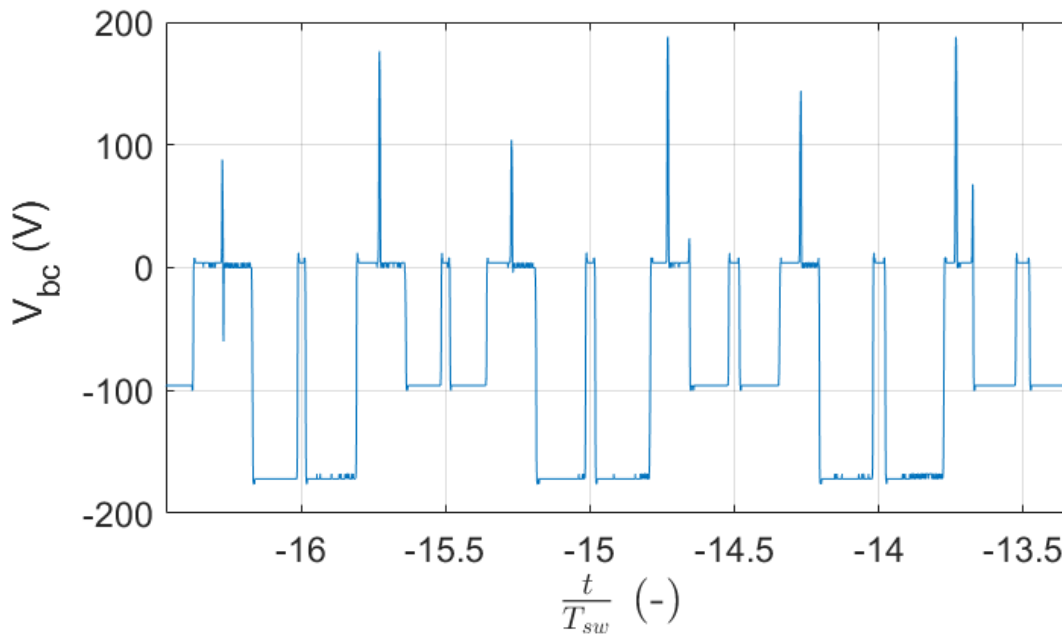

Figure 5.5: Dead time spikes

Instability of the output current

During this test, the Cinergia would sometimes switch off after the voltage at the terminal became too high. This event was preceded by oscillations in the input current of the Cinergia. The stability was improved when the digital filters on the current measurements of the RT-Box were relaxed, decreasing the delay in this signal. This problem was not present at lower operating frequencies, which makes sense as the different delays in the sensors of both the Cinergia and the RT-Box would have caused a lower phase delay, improving stability.

Common mode currents

In initial tests the Chroma 62024P showed odd behavior. This was investigated and a large common mode current was found in the going into both DC supplies. After analyzing the spectrum of this current, it was found that the main frequency components were at the switching frequency of the inverter and its harmonics. Figure 5.6 shows the common mode current of the second DC supply with the multi-source inverter operating at 48 kHz, before and after introducing a 9 mH common mode choke. This reduced the noise floor by 10 dB

and the first harmonic by 40 dB, successfully removing most of the common mode current and mitigating the problems.
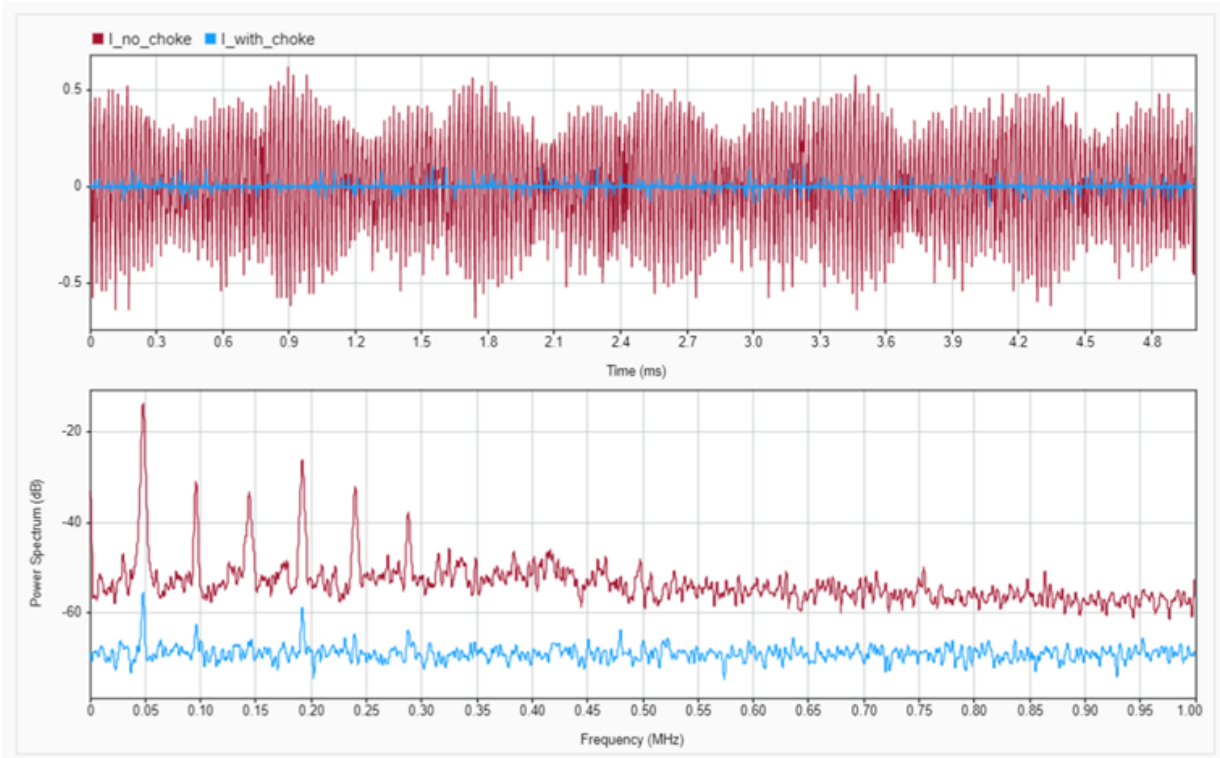

Figure 5.6: Common mode current with and without a common mode choke

Filtered voltage waveforms

The PWM voltages measured by the oscilloscope can be filtered to show the intended 400 Hz waveform. Figure 5.7a shows the voltage difference between phase A and the common DC ground voltage. It can be seen that the filtered waveform resembles the pattern seen with a DPWMmin modulation scheme for a 2-level inverter [49], this is the case because the two port vectors are in phase with each other due to the high power factor during this experiment. Figure 5.7b shows the resulting voltage difference between the other two phases, here it can be seen that the non-sinusoidal elements in phases cancel out with each other and result in a sinusoidal phase-phase voltage. The phase-phase voltage amplitude was measured at 129.3 V_p which is lower than the reference of 135.7 V_p. A decrease in the voltage is expected due to different inefficiencies like the voltage drop over the switches and switch dead time and is included in the series resistance R_f seen in Figure 5.3.
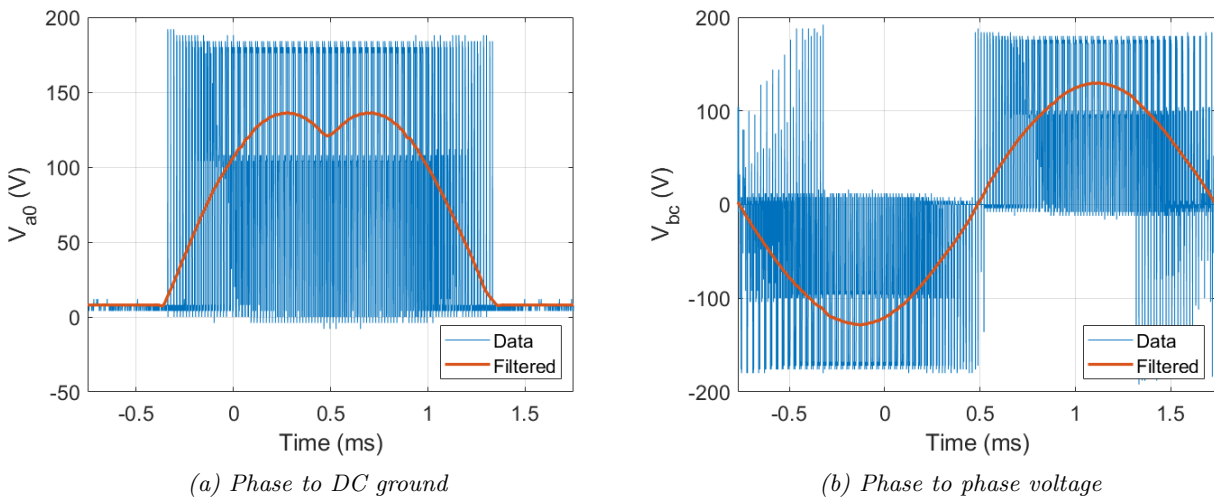
(a) Phase to DC ground   (b) Phase to phase voltage

Figure 5.7: Filtered voltage waveforms during the takeoff scenario

5.3.2 Climb

The second scenario is that during climb and the waveforms are comparable to those during takeoff, as can be seen in Figure 5.8. Here, the power factor should be almost exactly 100%. This can also be seen as the AC current wave is in line with the voltage of phase A. The DC current was measured at 3.97 A with a standard deviation of 32 mA, which is better than during the takeoff experiment. The AC current also has less noteworthy low frequency distortion and the fundamental component had a current of 5.39 $Arms$ comparable with the target 5.42 A_{rms}. The filtered phase-phase voltage was measured to be 117.6 V_p instead of the reference 123.1 V_p, again having a significant voltage drop.
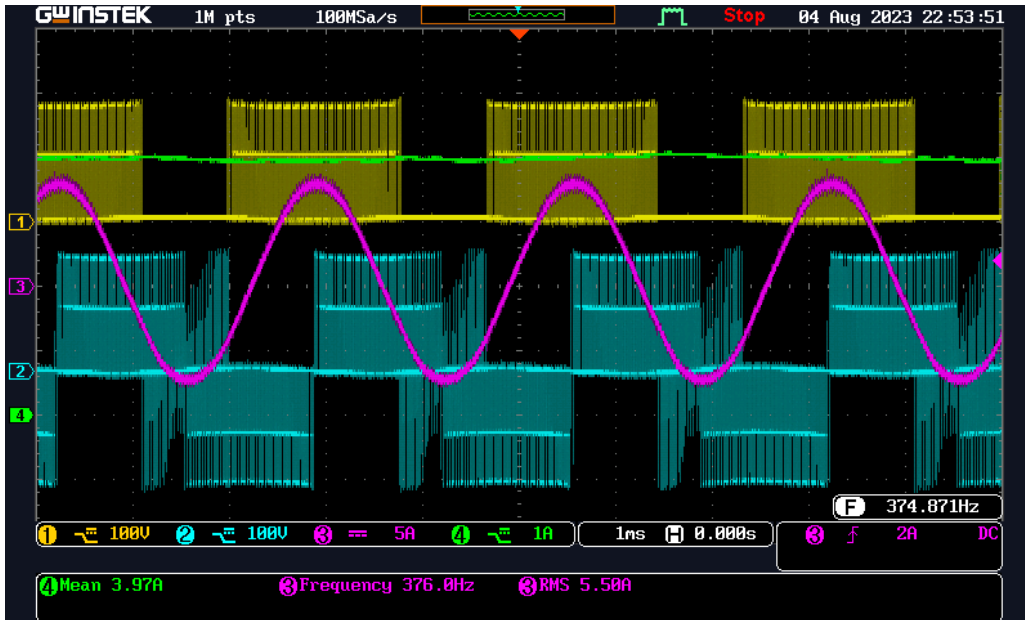
Figure 5.8: Experimental waveforms during the climb scenario

5.3.3 Cruise

The third scenario is that of the cruise phase of a flight. The introduction of a significant amount of field weakening current decreased the power factor of the machine in simulation. This means that the optimal angle algorithm comes into play, separating the PWM contributions of the two DC ports, as can be seen in Figure 5.9. The DC current is 4.98 A on average with an standard deviation of 33 mA which is very close to the desired 5 A. The AC current of 5.1 A_{rms} is smaller than the desired 5.3 A_{rms}
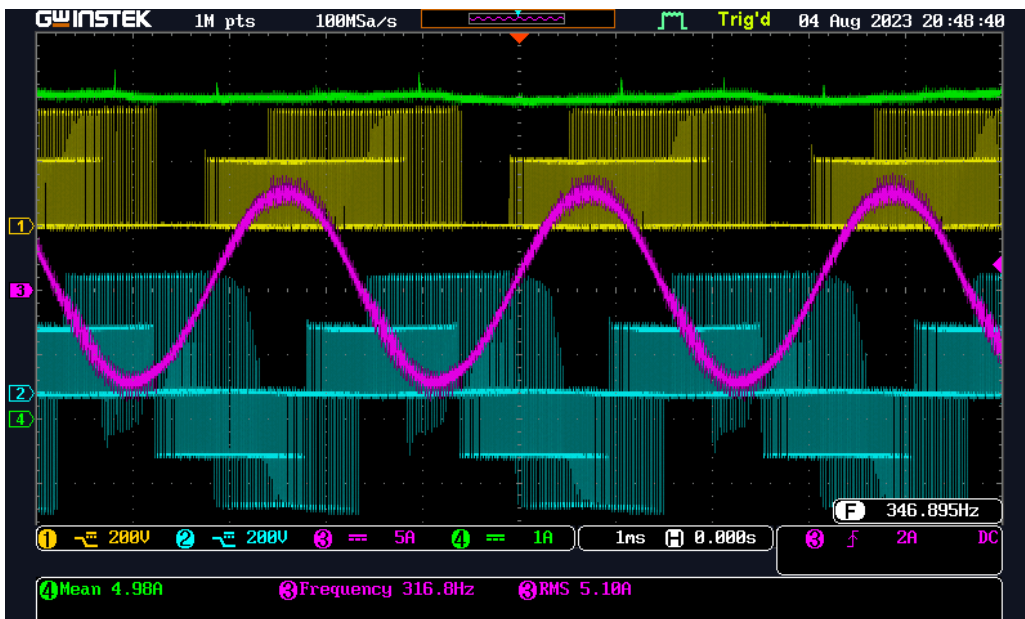

Figure 5.9: Experimental waveforms during the cruise scenario

When the voltage between phase A and DC ground is filtered the waveform is more chaotic than those in the previous scenarios. This is expected with the lower power factor of 80.8% and is the result of the fuel cell and battery port vectors having a different angle. Figure 5.10 shows this filtered voltage as well as the expected voltages from a simulation with the same scenario. The two were aligned in time and in addition to the expected output voltage the individual DC port components are also shown in the figure. As the current measured by the controller during this point in the experiment is not exactly known, some differences can be expected. It can be seen that the output voltage largely behaves as expected, with a small voltage difference at higher voltages and the angle between the two port vectors appears to be slightly different.
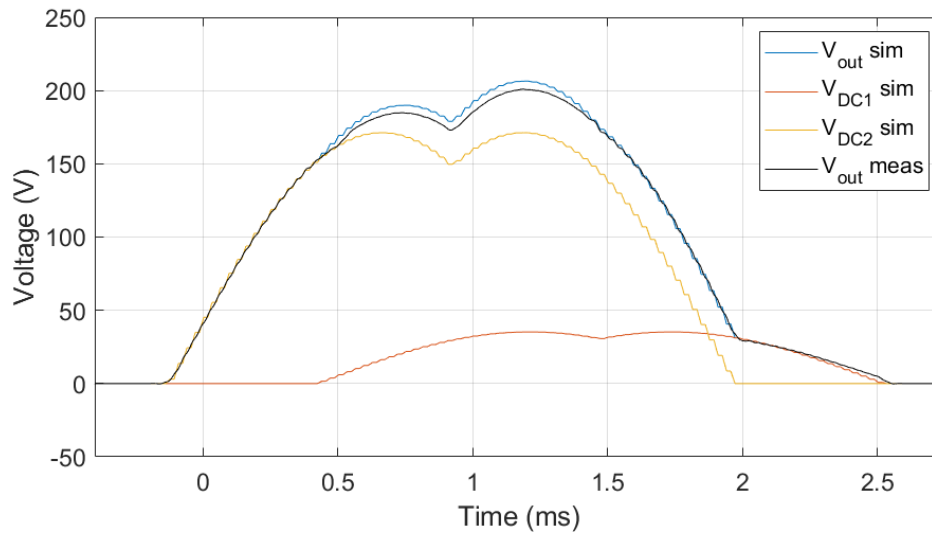

Figure 5.10: Comparison between simulated and measured phase voltage

5.3.4 Descent

The final test was on the descent stage of the flight and in this scenario the power factor is almost zero as the machine does not produce any torque. The small amount of real power is used to overcome the copper losses of the large field weakening current. The large reactive power on the machine is used to transfer power from the fuel cell to the battery. Figure 5.11 shows the resulting measurements. The fundamental component of the AC current was measured at 2.55 A_{rms}, close to the expected 2.62 A_{rms} but there is a large ripple present which will be explored further. The DC current was measured at 1.73 A with a standard deviation of 39 mA, slightly larger than the expected 1.71 A.
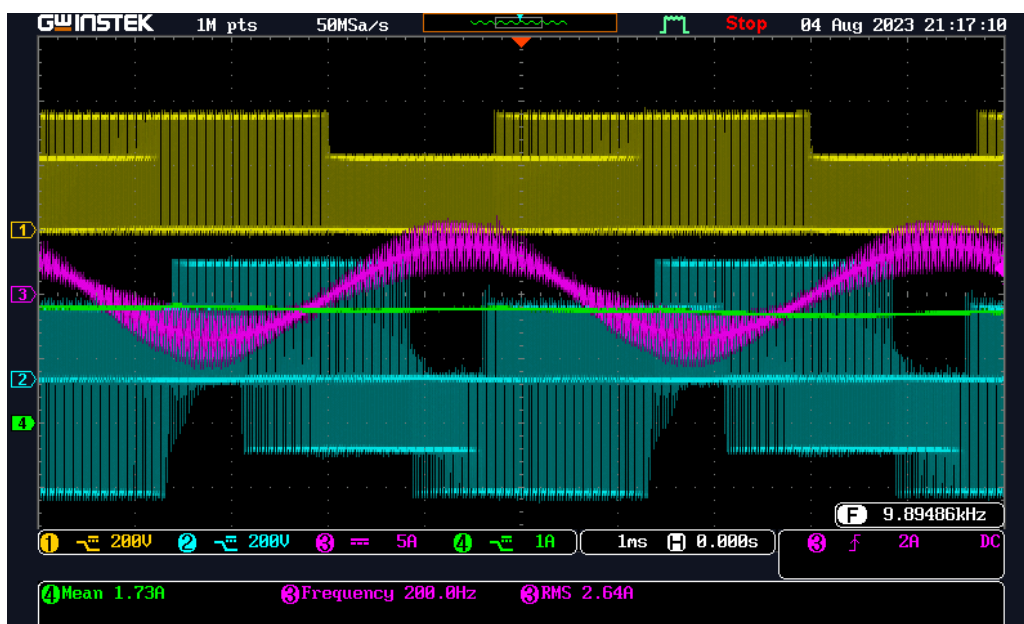

Figure 5.11: Experimental waveforms during the descent scenario

Vector space visualization

The vector space and angle selection during this scenario is explored further in Figure 5.12 with the voltage reference and current measurement from the experiment to highlight what is happening during the experiment. The vector space is shown in Figure 5.12a, the current and output voltage vectors can be seen to be almost 90° out of phase. The battery and fuel cell vector add up to the reference voltage as intended. For the fuel cell to deliver the required power it is placed close to the current vector. The relative available port power is shown in Figure 5.12b. The optimal angle estimate of $\theta_2 - \theta_{ref}$ appears to be right on the maximum of the active power. The angle of port vector 1 can also be seen on the opposite side of U_{ref}. The large ripple in the phase current can be explained by the large angles between the different port vectors and the opposing voltage applied on the motor inductance.
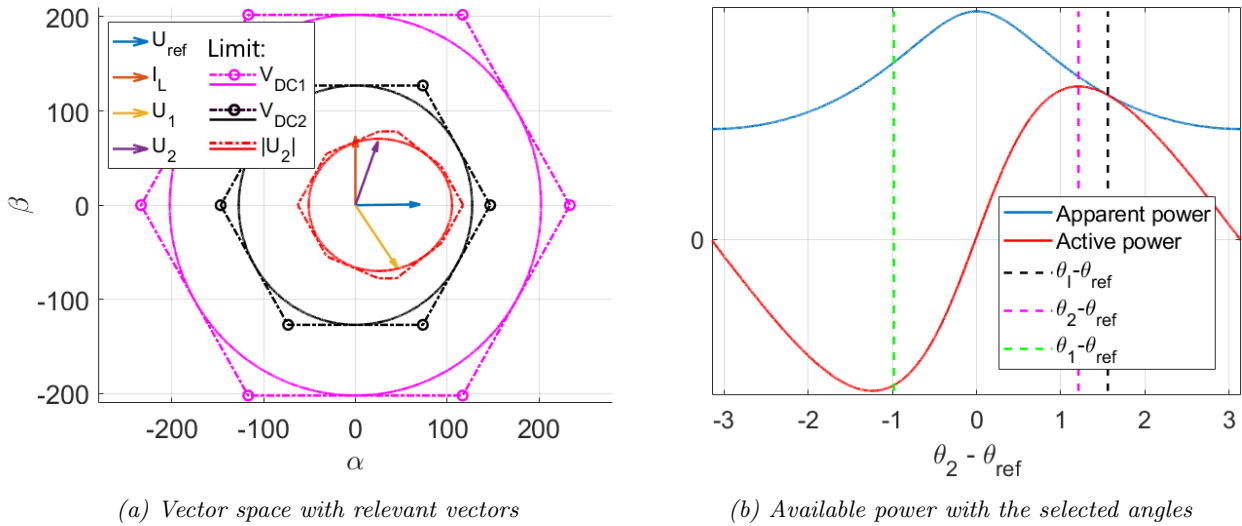

(a) Vector space with relevant vectors

(b) Available power with the selected angles

Figure 5.12: Vector space and optimal power angle as seen during the descent scenario

Filtered voltage waveforms

Finally, two periods of the voltage waveforms are filtered as shown in Figure 5.13. The difference between the takeoff phase to zero voltage in Figure 5.7a and that during the descent stage in Figure 5.13a can clearly be observed, caused by the difference in the port vector angles. The phase-phase voltage during the descent stage in Figure 5.13b is still completely sinusoidal however.
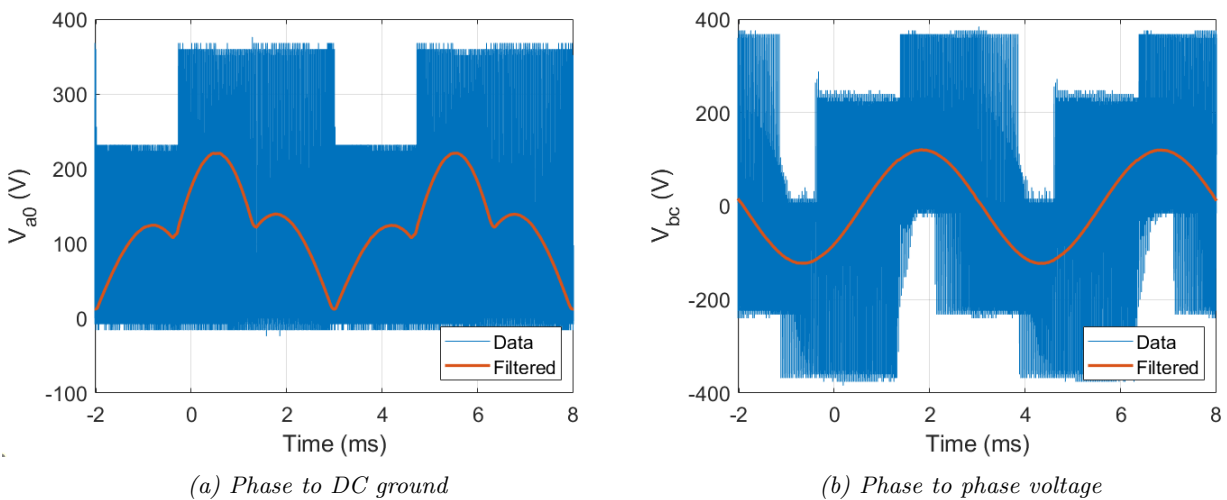

(a) Phase to DC ground

(b) Phase to phase voltage

Figure 5.13: Filtered voltage waveforms during the descent scenario

6. Conclusions and recommendations

6.1 Conclusions

After the investigation into the different aspects of a fuel cell and battery aircraft and different dual-DC-port architectures that can be used to integrate these different energy storage systems it is possible to return to the original research question and subquestions.

- Can the power distribution system in a battery and fuel cell electric aircraft be improved by combining a number of power electronic systems?

  - What are the challenges with distributing electric power between the different energy storage systems?
  - What dual-DC-port converters exist that are suitable for this application?
  - How do these dual-DC-port converters compare to a more conventional solution?

6.1.1 Challenges in a fuel cell and battery electric aircraft

The first subquestion was answered with an analysis of battery and fuel cell electric energy storage systems. The capabilities of commercially available technologies were considered, showing the advantage in the energy density of hydrogen storage systems as well as the power density of battery storage systems. After this, an analysis in the behavior and challenges of these technologies resulted in equivalent circuit models of the energy storage systems and a power distribution strategy. This strategy consisted of operating the fuel cells with a minimum idle power of 4 kW and an active power of 20 kW, with as few transitions between different load conditions as possible to improve the lifetime of the system. The active load of 20 kW, should allow the fuel cell to provide most of the energy in the duration of the flight, where the battery packs are preserved for the high load conditions, as well as a limited amount of regeneration.

6.1.2 Suitability of dual-DC-port inverters

The second subquestion was answered with an exploration of existing dual-DC-port inverter technologies. A comparison of a larger number of dual-DC-port inverters by Neira et al. listed the Z-source inverter as the only dual-DC-port inverter for use with machines [34]. In this research, four promising dual-DC-port inverters were considered for the distribution of power between the fuel cell system, battery packs and PMSM. The designs that appeared most promising in their respective papers were selected for further investigation. The modified split-source inverter turned out not to be suited for this application but the Z-source, split-source and multi-source inverters did perform well in the simulations. It may be the case however, that additional designs may prove to be suited to this application as well, maybe even better than the ones considered in this research. Variations include quasi-Z-source inverters and additional interfaces for the integrated dual-source inverters. This research showed that it is possible for a dual-DC-port inverter to function in this application based on simulations and lab tests.

6.1.3 Architecture comparison

The third subquestion was examined by subjecting multiple designs to a dynamic loading test in simulations. One reference design based on a separate DC/DC interleaved boost converter and DC/AC inverter has been compared to three dual-DC-port inverters on a number of significant characteristics, including the expected mass of passive components, switching losses and dynamic behavior. Some additional properties of designs could have been explored to further improve the quality of the comparison. This includes the conductive losses of passive components and semiconductors, the cost of different components, the volume or area taken up by components and the reliability of the system. Quantifying these elements would have proven difficult, as they lead to conflicting choices. For example, the series resistance of an inductor can be reduced by increasing the wire

diameter but this also increases weight and cost. Similar trade-offs are present in selection of semiconductors and other passive components. With the characteristics that have been used in the comparison, a useful insight to the feasibility of the designs has already been gained. The result for the Z-source and split-source inverter was that they add too much weight to the system without any significant benefits to compensate for this. The multi-source inverter proved more viable due to the lack of large inductors and was explored further in an experimental setup.

6.1.4 Multi-objective vector modulation

The exploration of the multi-source inverter and the possibility to use it in this application led to the development of an expanded multi-objective vector modulation algorithm. Existing algorithms in literature used similar approaches, but they were not sufficient to control the fuel cell output power in all operating conditions. The most important exception was when the power factor of the motor was near zero, like during a descent. The use of the optimal vector angle reduced the required field weakening current and enabled the system to function in all required operating conditions.

6.1.5 Experiments

The experimental setup was used to validate and expand the results of simulations by investigating the quasi-steady state operation of the multi-source inverter and multi-objective vector modulation algorithm. The tests were conducted on four common in flight operating conditions with results that corroborated the expectations from the analysis and simulations on the same system. The experiments did expose some weaknesses of this modulation strategy, seen in the low frequency distortion of the DC current signal and the instability at higher frequencies, both of which can be reduced by improving the current sensing. In total, the experiments and simulations showed that it is possible to distribute the power of the DC sources and an AC load with just one power electronic system that reduces the system complexity and size, while maintaining the same operating capacity.

6.2 Recommendations

A more in-depth design of a multi-source inverter is required to prove whether the design is actually better than the design with an interleaved boost converter and a standard inverter as the overall performance of the two systems is very similar. This also means that the main research question is partially left unanswered. The following recommendations can be used to further investigate this question.

6.2.1 System reliability

This research did not completely consider the reliability of the different system architectures and how a failure in one system may influence the functionality of the aircraft. In aviation the requirements on the system reliability are high and it may be possible that the dual-DC-port inverters improve or deteriorate the system reliability.

6.2.2 Extended experimental testing

The system can be tested more thoroughly with an improved HIL setup. Using an actual PMSM with angle sensor to operate the field oriented control loop would allow verification of the inverter under dynamic loads, including the variable field weakening control. The DC power supplies could be improved by the addition of an output impedance model, including the RC segments and SOC voltage dependency of the battery model and the non-linear voltage drop of the fuel cell. Combined with the repeating load profile of Figure 2.3 it would be possible to test the system under varying DC voltage levels, air-speeds, altitudes and other slow dynamic behaviors. In addition to executing additional tests on the multi-source inverter, the benchmark setup would also need to be realized and tested to allow a further comparison.

Energy management

The speed of simulations on the different architectures limited the duration to a couple of seconds. With a proper dynamic real-time setup the SOC dependency of the battery voltage will start to play an important role and would introduce the requirement of a proper energy management strategy. This includes immediate actions at a full or empty battery as well as preventive actions to avoid either state.

Bibliography

[1] Pipistrel Aircraft, "Pipistrel velis electro." [Online]. Available: https://www.pipistrel-aircraft.com/products/general-aviation/velis-electro/

[2] ——, "Velis electro 128 flyer." [Online]. Available: https://www.pipistrel-aircraft.com/wp-content/uploads/2023/04/Pipistrel_VelisElectro.pdf

[3] F. Cells and H. . J. Undertaking, *Hydrogen-powered aviation : a fact-based study of hydrogen technology, economics, and climate impact by 2050*. Publications Office, 2020.

[4] Boeing, "Boeing fuel cell demonstrator." [Online]. Available: https://secure.boeingimages.com/archive/Boeing-Fuel-Cell-Demonstrator-2F3XC5WZCWO.html

[5] ZeroAvia, "Aviation history: Hyflyer ii programme first flight: Hydrogen powered dornier 228: Hydrogen-electric engine," 2023. [Online]. Available: https://www.zeroavia.com/do228-first-flight

[6] E-mobility engineering, "Zeroavia hydrogen-electric aircraft," 2021. [Online]. Available: https://www.emobility-engineering.com/digest-zeroavia-hydrogen-electric-aircraft/

[7] D. Gates, "Pioneering moses lake flight uses hydrogen to power regional airplane," Mar 2023. [Online]. Available: https://www.seattletimes.com/business/boeing-aerospace/pioneering-moses-lake-flight-uses-hydrogen-to-power-regional-airplane/

[8] Pipistrel Aircraft, "Batteries systems and bms." [Online]. Available: https://www.pipistrel-aircraft.com/products/other-products/batteries-systems-and-bms/

[9] UK Defence Standardization (DStan), "Def stan 91-091," 2019.

[10] United States Department of Energy, "Doe comparison of fuel cell technologies." [Online]. Available: https://www.energy.gov/eere/fuelcells/comparison-fuel-cell-technologies

[11] M. Reuß, T. Grube, M. Robinius, P. Preuster, P. Wasserscheid, and D. Stolten, "Seasonal storage and alternative carriers: A flexible hydrogen supply chain model," *Applied Energy*, vol. 200, p. 290–302, 2017.

[12] United States Department of Energy, "Doe technical targets for onboard hydrogen storage for light-duty vehicles." [Online]. Available: https://www.energy.gov/eere/fuelcells/doe-technical-targets-onboard-hydrogen-storage-light-duty-vehicles

[13] M. C. Massaro, R. Biga, A. Kolisnichenko, P. Marocco, A. H. A. Monteverde, and M. Santarelli, "Potential and technical challenges of on-board hydrogen storage technologies coupled with fuel cell systems for aircraft electrification," *Journal of Power Sources*, vol. 555, p. 232397, 2023. [Online]. Available: https://www.sciencedirect.com/science/article/pii/S037877532201374X

[14] Powercell, "Powercell stacks and systems," 2023. [Online]. Available: https://powercellgroup.com/corporate-governance/product-range/

[15] Pipistrel Aircraft, "E-811 electric engine." [Online]. Available: https://www.pipistrel-aircraft.com/products/other-products/e-811/#tab-id-2

[16] Powercell, "V-stack fuel cells," 2022. [Online]. Available: https://powercellgroup.com/wp-content/uploads/2022/05/v-stack-v-221.pdf

[17] J. Larmini and A. Dicks, *Fuel Cell Systems Explained*. New York: Wiley, 2000.

[18] C. Song, Y. Tang, J. L. Zhang, J. Zhang, H. Wang, J. Shen, S. McDermid, J. Li, and P. Kozak, "Pem fuel cell reaction kinetics in the temperature range of 23–120°c," *Electrochimica Acta*, vol. 52, no. 7, p. 2552–2561, 2007.

[19] T. E. Springer, T. A. Zawodzinski, and S. Gottesfeld, "Polymer electrolyte fuel cell model," *Journal of The Electrochemical Society*, vol. 138, no. 8, p. 2334–2342, 1991.

[20] F. Barbir, *PEM fuel cells: Theory and practice.* Elsevier/Academic Press, 2013.

[21] A. Alaswad, A. Omran, J. R. Sodre, T. Wilberforce, G. Pignatelli, M. Dassisti, A. Baroutaji, and A. G. Olabi, "Technical and commercial challenges of proton-exchange membrane (pem) fuel cells," *Energies*, vol. 14, no. 1, p. 144, 2020.

[22] P. Ren, P. Pei, Y. Li, Z. Wu, D. Chen, and S. Huang, "Degradation mechanisms of proton exchange membrane fuel cell under typical automotive operating conditions," *Progress in Energy and Combustion Science*, vol. 80, p. 100859, 2020.

[23] G. S. Harzer, J. N. Schwämmlein, A. M. Damjanović, S. Ghosh, and H. A. Gasteiger, "Cathode loading impact on voltage cycling induced pemfc degradation: A voltage loss analysis," *Journal of The Electrochemical Society*, vol. 165, no. 6, 2018.

[24] M. Jouin, R. Gouriveau, D. Hissel, M.-C. Péra, and N. Zerhouni, "Degradations analysis and aging modeling for health assessment and prognostics of pemfc," *Reliability Engineering & System Safety*, vol. 148, p. 78–95, 2016.

[25] C. Wang, M. Nehrir, and S. Shaw, "Dynamic models and model validation for pem fuel cells using electrical circuits," *IEEE Transactions on Energy Conversion*, vol. 20, no. 2, pp. 442–451, 2005.

[26] W. Chen, B. Chen, K. Meng, H. Zhou, and Z. Tu, "Experimental study on dynamic response characteristics and performance degradation mechanism of hydrogen-oxygen pemfc during loading," *International Journal of Hydrogen Energy*, vol. 48, no. 12, pp. 4800–4811, 2023. [Online]. Available: https://www.sciencedirect.com/science/article/pii/S0360319922052223

[27] R. Korthauer, *Lithium-Ion Batteries: Basics and Applications.* Springer Berlin Heidelberg, 2018.

[28] R. Zhang, B. Xia, B. Li, L. Cao, Y. Lai, W. Zheng, H. Wang, W. Wang, and M. Wang, "A study on the open circuit voltage and state of charge characterization of high capacity lithium-ion battery under different temperature," *Energies*, vol. 11, no. 9, p. 2408, 2018.

[29] M. Farag, M. Fleckenstein, and S. R. Habibi, "Li-ion battery soc estimation using non-linear estimation strategies based on equivalent circuit models," *SAE Technical Paper Series*, 2014.

[30] U. Westerhoff, K. Kurbach, F. Lienesch, and M. Kurrat, "Analysis of lithium-ion battery models based on electrochemical impedance spectroscopy," *Energy Technology*, vol. 4, no. 12, p. 1620–1630, 2016.

[31] S. Cruz-Manzo and P. Greenwood, "Analytical transfer function to simulate the dynamic response of the finite-length warburg impedance in the time-domain," *Journal of Energy Storage*, vol. 55, p. 105529, 2022.

[32] R. Guo, L. Lu, M. Ouyang, and X. Feng, "Mechanism of the entire overdischarge process and overdischarge-induced internal short circuit in lithium-ion batteries," *Scientific Reports*, vol. 6, no. 1, 2016.

[33] C. Schlasza, P. Ostertag, D. Chrenko, R. Kriesten, and D. Bouquain, "Review on the aging mechanisms in li-ion batteries for electric vehicles based on the fmea method," *2014 IEEE Transportation Electrification Conference and Expo (ITEC)*, 2014.

[34] S. Neira, Z. Blatsi, M. M. Merlin, and J. Pereda, "A technical overview of single-stage three-port dc-dc-ac converters," in *2022 24th European Conference on Power Electronics and Applications (EPE'22 ECCE Europe)*, 2022.

[35] N. Mohan, T. M. Undeland, and W. P. Robbins, *Power Electronics: Converters, applications, and design.* John Wiley &; Sons, 2003.

[36] Microsemi, "Msc015sma070b4 datasheet," 2023. [Online]. Available: https://nl.mouser.com/datasheet/2/268/Microsemi_MSC015SMA070B4_SiC_MOSFET_Datasheet_A-2934518.pdf

[37] KEMET, "C4aq capacitor datasheet," 2023. [Online]. Available: https://content.kemet.com/datasheets/KEM_F3128_C4AQ_P.pdf

[38] M. Electronics, "C4aq capacitor at mouser electronics," 2023. [Online]. Available: https://nl.mouser.com/ProductDetail/KEMET/C4AQLEW6210A3BK?qs=byeeYqUIh0M6WLgslAS9vA%3D%3D

[39] P. GmbH, "Plecs user manual," 2023. [Online]. Available: https://www.plexim.com/files/plecsmanual.pdf

[40] Emrax, "Emrax 268 pmsm," 2022. [Online]. Available: https://emrax.com/wp-content/uploads/2022/11/EMRAX_268_datasheet_A00.pdf

[41] S. Farhani, A. N'Diaye, A. Djerdir, and F. Bacha, "Design and practical study of three phase interleaved boost converter for fuel cell electric vehicle," *Journal of Power Sources*, vol. 479, p. 228815, 2020. [Online]. Available: https://www.sciencedirect.com/science/article/pii/S0378775320311198

[42] S. Hu, Z. Liang, and X. He, "Ultracapacitor-battery hybrid energy storage system based on the asymmetric bidirectional z -source topology for ev," *IEEE Transactions on Power Electronics*, vol. 31, no. 11, pp. 7489–7498, 2016.

[43] A. Abdelhakim, P. Mattavelli, and G. Spiazzi, "Split-source inverter," in *IECON 2015 - 41st Annual Conference of the IEEE Industrial Electronics Society*, 2015, pp. 001 288–001 293.

[44] S. Neira, J. Pereda, and F. Rojas, "Three-port full-bridge bidirectional converter for hybrid dc/dc/ac systems," *IEEE Transactions on Power Electronics*, vol. 35, no. 12, pp. 13 077–13 084, 2020.

[45] E. Fedele, A. Cervone, I. Spina, D. Iannuzzi, and A. D. Pizzo, "Multiobjective vector modulation for improved control of npc-based multi-source inverters in hybrid traction systems," *IEEE Journal of Emerging and Selected Topics in Power Electronics*, vol. 10, no. 6, pp. 7464–7474, 2022.

[46] ONSEMI, "Pcff75h120swf datasheet," 2023. [Online]. Available: https://www.onsemi.com/download/data-sheet/pdf/pcff75h120swf-die-d.pdf

[47] C. Liu, C. Xu, J. Ruan, L. Jin, L. Bao, and Y. Deng, "A vector control strategy for a multi-port bidirectional dc/ac converter with emphasis on power distribution between dc sources," in *IECON 2019 - 45th Annual Conference of the IEEE Industrial Electronics Society*, vol. 1, 2019, pp. 1579–1584.

[48] P. GmbH, "Rt box ce," 2023. [Online]. Available: https://www.plexim.com/products/rt_box/rt_box_ce

[49] A. Hava, S.-K. Sul, R. Kerkman, and T. Lipo, "Dynamic overmodulation characteristics of triangle intersection pwm methods," *IEEE Transactions on Industry Applications*, vol. 35, no. 4, pp. 896–907, 1999.

A. Acronyms

NLR	Netherlands Aerospace Centre
PEMFC	Proton exchange membrane fuel cell
FC	Fuel cell
DC	Direct current
AC	Alternating current
PMSM	Permanent magnet synchronous machine
SOC	State of charge
BMS	Battery management system
PWM	Pulse width modulation
EMF	Electromotive force
FPGA	Field-programmable gate array
MOVM	Multi-objective vector modulation
RC	Resistor, capacitor
CLC	Capacitor, inductor, capacitor
RLC	Resistor, inductor, capacitor
FoM	Figure of merit
ESR	Equivalent series resistance
SVPWM	Space vector pulse width modulation
DPWM	Discontinuous space vector pulse width modulation
HIL	Hardware-in-the-loop

B. Recurring simulation results

The recurring nature of the simulations and the similarities between results made it seem unnecessary to repeat the full simulation results in the main report. The mayor differences that are observed between designs are highlighted in other figures.
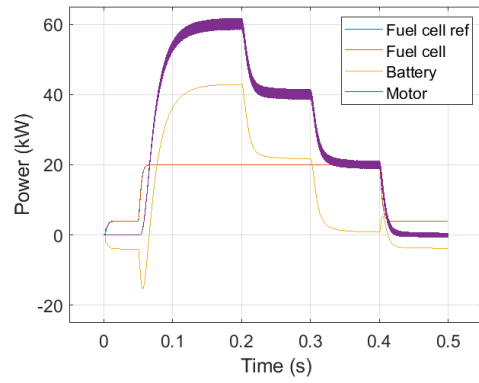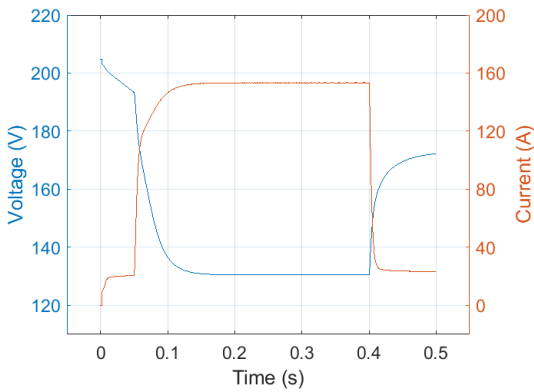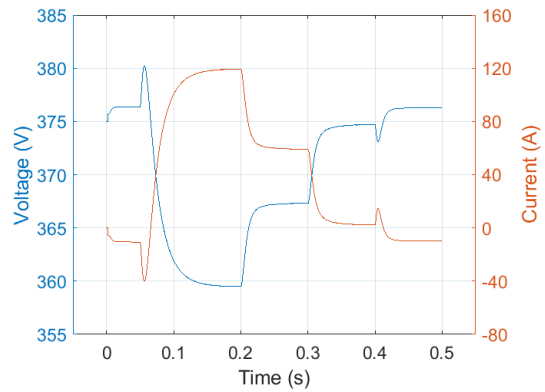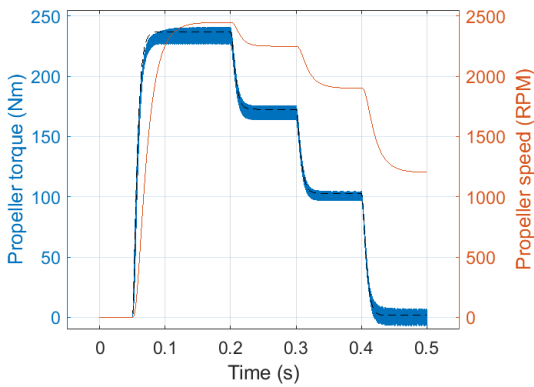

(a) Motor output

(b) Power distribution

(c) Fuel cell system behavior

(d) Battery system behavior
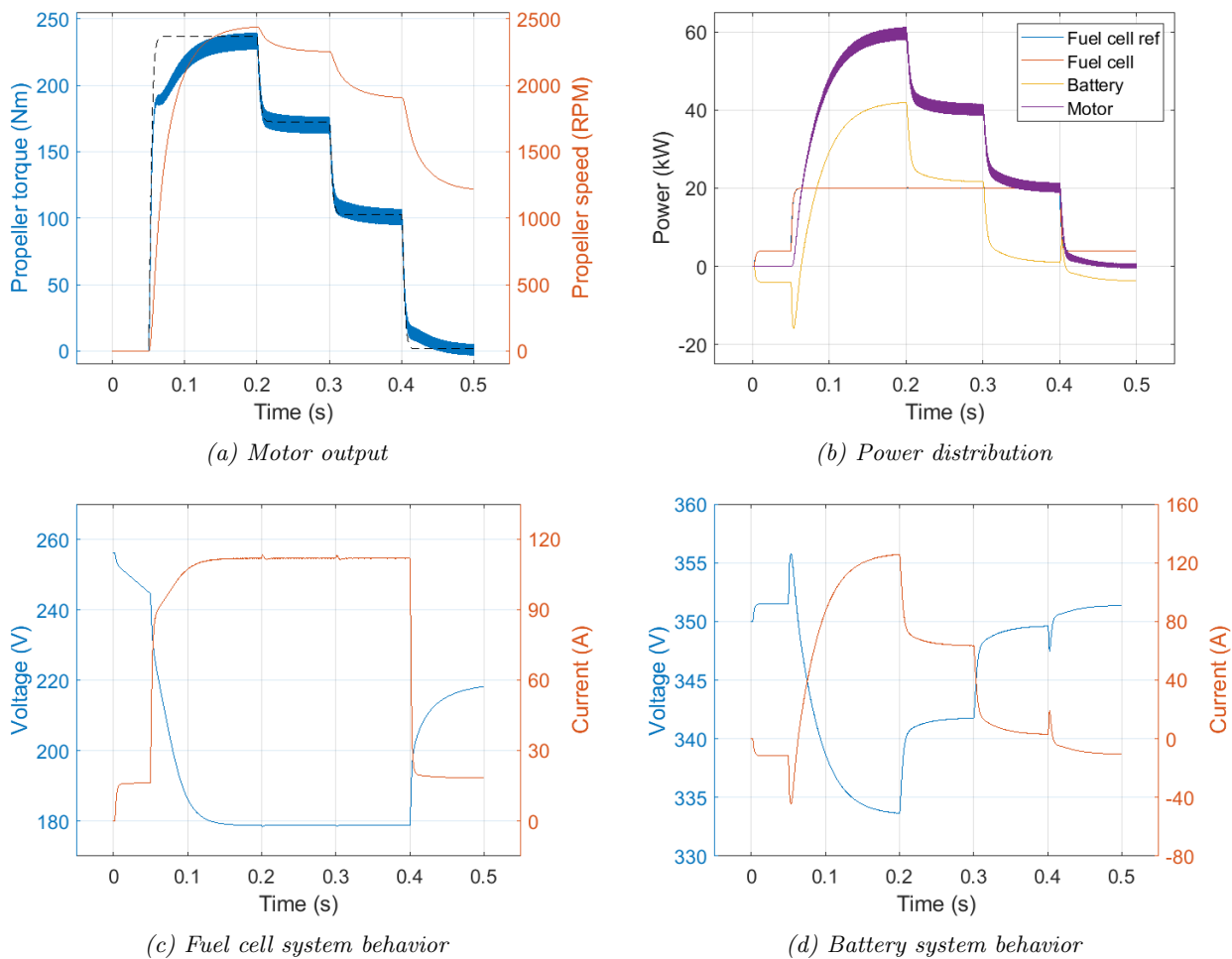
Figure B.1: Dynamic behavior of the Z-source inverter
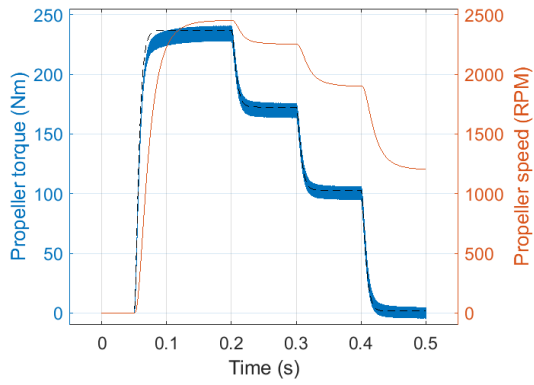
(a) Motor output

(b) Power distribution
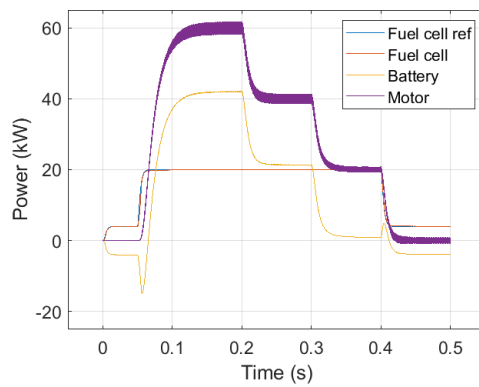
(c) Fuel cell system behavior
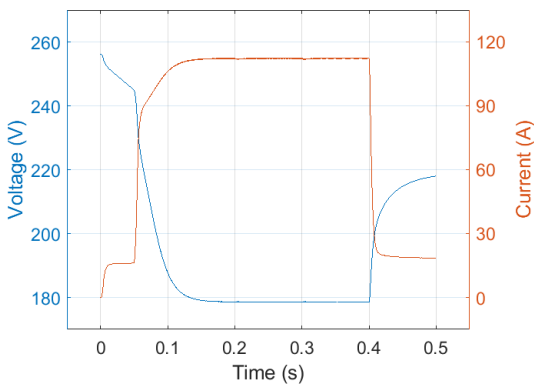
(d) Battery system behavior

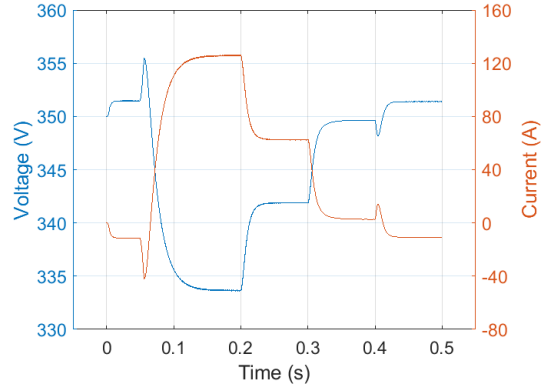Figure B.2: Dynamic behavior of the split-source inverter

(a) Motor output

(b) Power distribution

(c) Fuel cell system behavior

(d) Battery system behavior

Figure B.3: Dynamic behavior of the multi-source inverter